

**MODELING AND OPTIMIZATION OF
PHOTO AND PHOTOCATALYTIC WATER
DETOXIFICATION AND DISINFECTION REACTORS**

XU CHEN

(M. Sc)

A THESIS SUBMITTED

FOR THE DEGREE OF DOCTOR OF PHILOSOPHY

DEPARTMENT OF CHEMICAL AND BIOMOLECULAR ENGINEERING

NATIONAL UNIVERSITY OF SINGAPORE

2014

Declaration

I hereby declare that this thesis is my original work and it has been written by me in its entirety. I have duly acknowledged all the sources of information which have been used in this thesis.

This thesis has also not been submitted for any degree in any university previously.

Xu Chen

4 September 2014

Acknowledgements

I would like to express my greatest gratitude to my supervisor, Professor Gade Pande Rangaiah and co-supervisor, Professor Zhao Xiu Song, George for their continuous encouragement, patience and guidance throughout my whole PhD candidature. This project has been an enriching and invaluable experience for me.

I would also like to express my sincere appreciation to the Department of Chemical and Biomolecular Engineering of National University of Singapore for offering me this opportunity to study as a PhD candidate with a scholarship.

I would like to thank my fellow group and lab mates for their kind help throughout my PhD candidature, Dr. Xiong Zhigang, Dr. Cai Zhongyu, Mr. Han Gang, Mr. Dou Haiqing, Dr. Tian Xiaoning, Dr. Zhang Lili, Dr. Liu Jiajia, Dr. Wu Pingping, Dr. Zhang Jintao, Ms. Ma Jizhen, Mr. Zhou Rui and Mr. Yu Yong.

Acknowledgement also goes to Ms. Sylvia Wan and Ms. Jamie Siew for their kind support on laboratory matters.

I would like to express my deepest thankfulness to my family. They have always been supportive throughout my PhD candidature.

Table of Contents

Declaration.....	i
Acknowledgements.....	i
Table of Contents.....	ii
Summary.....	vii
List of Tables.....	ix
List of Figures.....	x
Nomenclatures.....	xiii
Chapter 1 Introduction.....	1
1.1. Photo and photocatalytic water treatment.....	1
1.2. Objectives of this thesis work.....	2
1.3. Structure of this thesis.....	3
Chapter 2 Literature Review.....	4
2.1. Introduction.....	4
2.2. Water disinfection.....	4
2.2.1. Conventional water disinfection.....	5
2.2.2. UV disinfection.....	6
2.3. Computational fluid dynamics simulation.....	7
2.4. UV fluence rate field.....	8

Table of Contents

2.4.1. Photonic laws	8
2.4.2. Lamp models.....	10
2.4.3. Light distribution in photocatalytic reactors	12
2.5. Fluid dynamics models and CFD simulation.....	13
2.5.1. The standard k- ϵ model.....	14
2.5.2. The realizable k- ϵ model.....	14
2.5.3. Approaches to describe particle motion trajectories	15
2.6. Data-driven modeling	16
2.7. Photocatalytic water treatment.....	17
2.7.1. Photocatalysts	19
2.7.2. Photocatalytic water treatment reactors	22
2.7.3. Catalyst loading	24
2.7.4. Target pollutants	25
2.7.5. Modeling of photocatalytic degradation	26
2.8. Summary.....	31
Chapter 3 Simulation Methodology.....	32
3.1. Introduction.....	32
3.2. TURF method for simulation of UV disinfection reactor.....	32
3.3. Reactor specifications	33
3.3.1. Single lamp reactors.....	33
3.3.2. Multi-lamp reactors.....	34
3.4. Establishment of UV fluence rate field.....	36

3.5. Construction of fluid velocity profile	38
3.6. UV fluence distribution and disinfection performance.....	39
3.7. Comparison of simulation methodologies	40
3.8. Summary.....	41
Chapter 4 CFD Simulation of Photo Water-Disinfection Reactors.....	42
4.1. Introduction.....	42
4.2. UV fluence rate field.....	42
4.3. Flow velocity field	44
4.4. UV fluence received by particles	46
4.5. Particle size and shape	47
4.6. Reactor efficiency and water flow rate	49
4.7. Dimensionless analysis	51
4.8. Reactor shape and size	53
4.9. Radial displacement.....	56
4.10. Conclusions.....	59
Chapter 5 CFD Simulation of Reactors with Multiple Lamps	61
5.1. Introduction.....	61
5.2. UV fluence rate field.....	61
5.3. Water flow profile.....	64

Table of Contents

5.4. Reactor performance	66
5.4.1. Type A and B parallel reactors	66
5.4.2. Parallel reactors.....	67
5.4.3. Perpendicular reactors.....	68
5.4.4. Comparison among all reactors	70
5.5. Normalized standard deviations.....	71
5.6. Conclusions.....	73
Chapter 6 Modeling and Optimization of Photo-Disinfection Reactors	74
6.1 Introduction.....	74
6.2. ANN and GP modeling.....	74
6.2.1. ANN modeling.....	76
6.2.2. GP modeling	76
6.2.3. Multi-objective optimization	76
6.3. Accuracy of ANN and BioGP models	77
6.3.1. ANN model.....	77
6.3.2. BioGP model.....	79
6.4. Multi-objective optimization	80
6.4.1. Process optimization using the ANN model.....	80
6.4.2. Process optimization using BioGP model.....	84
6.4.3. Optimal values of design and operating variables	86
6.5. Conclusions.....	88

Chapter 7 Photocatalytic Degradation: Experiments and Modeling	90
7.1. Introduction.....	90
7.2. Experimental methods	90
7.2.1. Reagents.....	90
7.2.2. Experimental procedure	90
7.3. Adsorption-desorption equilibrium.....	92
7.4. Effects of different lamps.....	93
7.5. TiO ₂ concentration	95
7.6. Initial MB concentration	97
7.7. Modelling of degradation.....	99
7.8. Conclusions.....	104
Chapter 8 Conclusions and Recommendations	106
8.1. Conclusions.....	106
8.2. Recommendations for future work	108
References.....	110
List of Publications	126

Summary

Photo and photocatalytic water treatment are promising technologies to solve water crisis. However, modeling and optimization of photo and photocatalytic detoxification and disinfection processes are still far from satisfactory, due to the complicated nature of these processes involving multi-phase, highly turbulent flow and complex response of pollutants against those processes. Over the past few decades, researchers have devoted effort to establish such models.

Computational Fluid Dynamics (CFD) has been applied to modeling of photo and photocatalytic processes as computer simulation saves both time and money in developing better processes. Recent developments in both hardware and software enable simulation of highly turbulent flows with satisfactory accuracy. In this thesis work, a new methodology (namely, **Three-step UV fluence Rate and Fluid dynamics, TURF**) utilizing CFD simulation to model photo disinfection reactors was proposed. This method saves time and enables independent analysis of UV fluence and water flow profile without compromising accuracy.

TURF methodology was applied to UV water disinfection reactors with different reactor layouts, sizes, water flow rates, microorganism particle sizes and shapes, lamp powers and arrangements. The impacts of these design and operating parameters on reactor performance were analyzed based on UV efficiency and log reduction of microorganisms. It was found that larger reactors (longer length and larger cross sectional area) enhance reactor performance under constant UV dosage received by the water stream. Microorganism particle size and shape had little effect on UV fluence received by these particles. The effect of water flow rate on reactor performance is highly complex. Lower water flow rate would enhance log reduction of microorganisms due to increase in residence time.

Reactors with multiple lamps did not perform better than those with single lamp, despite their more uniform UV fluence rate distribution inside the reactors. Placing lamps directly below water inlet and outlet helps to retain the particles inside the reactors longer, thus increasing UV fluence received by the particles and subsequently log reduction.

Process optimization using CFD simulations is computationally very intensive. Hence, based on extensive simulation data, Artificial Neural Network (ANN) and Genetic

Programming (GP) were applied to model and optimize the photo-disinfection reactors. ANN was able to establish model with smaller error, while GP was able to predict better for new input variable sets and performed better in optimization. The optimal solutions obtained using GP were better than those using ANN in CFD testing. Multi-objective optimization results revealed that reactors with longer length and larger cross-sectional area operating under low water flow rate are favored.

Photocatalytic degradation of methylene blue by titanium dioxide was conducted. The impacts of lamp selection, catalyst concentration and initial concentration of methylene blue were analyzed. Desorption of methylene blue from catalyst surface at the beginning phase of the degradation process was observed. This is modeled and reported in this thesis work, probably for the first time. A model was constructed taking both degradation and desorption effects into consideration.

List of Tables

Table 3.1 Comparison of simulation results with the experimental values [9].....	41
Table 6.1 Input variables and their ranges used for obtaining the data for modeling.....	75
Table 6.2 Selected Pareto-optimal solutions and their CFD test results.....	82
Table 7.1 Constants for photocatalytic degradation and desorption.....	102

List of Figures

Figure 2.1 Coverage of safe drinking water around the world [11].....	5
Figure 2.2 Cutaway view of UV disinfection reactors in NEWater plants, courtesy of Dr. Xiong Zhigang	7
Figure 2.3 Schematic of reflection and refraction.....	9
Figure 2.4 Schematic for the SPACE model [7].....	11
Figure 2.5 Mechanism of photocatalytic reaction.....	18
Figure 2.6 Schematic of various pathways to form 3-D porous photocatalysts [17].....	20
Figure 3.1 Layouts of single-lamp UV photo reactors.....	34
Figure 3.2 Reactor layouts studied in this work; inlet and outlet nozzles are shown as small shaded circles on top of the large cylindrical surface	35
Figure 3.3 Schematic for the MPSS model calculation	36
Figure 4.1 UV fluence rate distribution in a reactor: (a) along axial direction at different radii, and (b) along radial direction at different axial positions	43
Figure 4.2 Turbulence intensity distribution in different reactors	45
Figure 4.3 Turbulence intensity distribution in a U-shaped reactor	45
Figure 4.4 Residence time of water and microorganisms under different water flow rates ...	46
Figure 4.5 Average UV fluence against residence time under constant UV lamp power and different water flow rates	47
Figure 4.6 Distribution of UV fluence received by particles with different diameters, d_p , and shape factors (SF) in a U-shaped disinfection reactor	48
Figure 4.7 Efficiency of the reactor under different water flow rates with constant average UV fluence	50
Figure 4.8 Relationship between single-lamp reactor efficiency, η , and normalized standard deviation of UV fluence, S_U , at average UV fluence = 116 J/m ²	51
Figure 4.9 Comparison of probability density of normalized UV fluence calculated from inverse Gaussian distribution and simulation results.....	52

Figure 4.10 Comparison of reactor efficiency calculated from inverse Gaussian distribution and simulation results	52
Figure 4.11 Log reduction of different single-lamp reactors with dosage at 15 J/kg	53
Figure 4.12 Reactor performance of reactors with different lengths	54
Figure 4.13 Performance of reactors with different outer radii	55
Figure 4.14 Performance of reactors with different outer radii	566
Figure 4.15 Linear-shaped reactor log reduction and r-displacement, dosage = 15 J/kg	57
Figure 4.16 U-shaped reactor log reduction and r-displacement, dosage = 15 J/kg	58
Figure 4.17 Variation of log reduction with S_{rd} in U-shaped reactors of different lengths (a), outer radii (b) and inner radii (c) and S_{rd} , with dosage = 15 J/kg	598
Figure 5.1 UV fluence rate in parallel (plot a) and perpendicular (plot b) reactors.....	622
Figure 5.2 Average and normalized standard deviation of UV fluence rate in different reactors.....	633
Figure 5.3 Water flow velocity profile in m/s and average turbulence intensity in parallel (plot a) and perpendicular (plot b) reactors at water flow rate of 1000 g/s	655
Figure 5.4 Comparison of log reduction (plot a) and average particle residence time over water residence time (plot b) of 4-lamp and single-lamp reactors.....	666
Figure 5.5 Disinfection performance comparison of parallel reactors.....	688
Figure 5.6 Disinfection performance comparison of perpendicular reactors.....	699
Figure 5.7 Water flow vector profile at different water flow rates in the 6-PER-B reactor ...	70
Figure 5.8 Disinfection performance comparison of best parallel and perpendicular reactors with single-lamp reactor	711
Figure 5.9 Relationship between normalized standard deviation of UV fluence (S_U) and that of residence time (S_t).....	722
Figure 5.10 Contour plot of log reduction versus average UV fluence (\bar{U}_p) and S_t	722
Figure 6.1 Reactor layouts: parallel type in the top row and perpendicular type in the bottom row, grey circles are water inlets and outlets	755
Figure 6.2 Parity plots of output predictions by ANN model (plot a) and by BioGP model (plot b), versus actual output (target) values.....	788

Figure 6.3 Pareto-optimal solutions based on the ANN model; highest log reduction at some UV dosages in the training data are also shown for comparison.....	80
Figure 6.4 Pareto-optimal solutions found using ANN models with different number of hidden neurons.....	811
Figure 6.5 Comparison of model predictions with CFD test for input variables of POS1-ANN (plot a) and POS2-ANN (plot b), with varying UV dosage.....	833
Figure 6.6 Pareto-optimal solutions based on the BioGP model; highest log reduction at some UV dosages in the training data are also shown for comparison	844
Figure 6.7 Comparison of model predictions with CFD test for input variables of POS3-BioGP (plot a) and POS4-BioGP (plot b), with varying UV dosage.....	855
Figure 6.8 Selected design and operating variables of the Pareto-optimal solutions obtained using the developed BioGP model.....	877
Figure 6.9 Distribution of lamp arrangements in the Pareto-optimal solutions.....	888
Figure 7.1 Schematic of the photo-reactor.....	911
Figure 7.2 Change in light absorbance over time when the radiation was shielded or not for the 0.2g/L–20ppm run; error bars are also shown	922
Figure 7.3 Degradation of MB with different lamps: TiO ₂ concentration = 0.5 g/L, and initial MB concentration = 20 ppm	944
Figure 7.4 Degradation of MB with different TiO ₂ concentration, a 500 W mercury lamp, and initial MB concentration of (a) 20 ppm, (b) 25 ppm, (c) 30 ppm, and (d) 35 ppm.....	966
Figure 7.5 Degradation of MB with different initial MB concentration, 500 W mercury lamp and TiO ₂ concentration of: (a) 0.2 g/L, (b) 0.3 g/L, (c) 0.4 g/L, and (d) 0.5 g/L.....	988
Figure 7.6 Variation of light absorbance of 0.5 g/L TiO ₂ with MB concentration.....	1011
Figure 7.7 Light absorbance for selected runs and the model predictions.....	1011
Figure 7.8 Degradation rate constants at different TiO ₂ and initial MB concentrations	1033
Figure 7.9 Desorption rate constants at different TiO ₂ and initial MB concentrations	1044

Nomenclatures

Normal cases:

C_a	concentration of methylene blue adsorbed on the surface of the catalyst (g/g catalyst)
C_{a0}	concentration of adsorbed methylene blue at the start of light radiation (g/g catalyst)
C_f	concentration of free methylene blue in the solution (g/L)
C_{f0}	concentration of free methylene blue in the solution at the start of light radiation (g/L)
C_s	catalyst concentration (g/L)
D	displacement (m)
d	diameter (cm or μm)
k_1	degradation reaction rate constant (hr^{-1})
k_2	desorption rate constant (hr^{-1})
P	UV fluence rate (W/m^2)
\bar{P}_R	Average UV fluence rate inside a reactor (W/m^2)
Q	water flow rate (g/s)
r	radial distance from the axis of the reactor (m)
S	normalized standard deviation (dimensionless)
SF	shape factor (dimensionless)
t	residence time (s)
U	UV fluence (J/m^2)
\bar{U}_p	average UV fluence received by particles (J/m^2)
V	volume (m^3)

Nomenclatures

X	light absorbance of the reaction suspension (A.U.)
x	axial distance from the inlet end of the reactor (m)
η	reactor efficiency based on log reduction (dimensionless)
σ	standard deviation

Subscripts:

P	of UV fluence rate
p	of particles
PR	of UV fluence rate inside the reactor
R	of reactors
r	in radial direction
rd	displacement of particles in radial direction
U	of UV fluence
w	of water

Chapter 1

Introduction

1.1. Photo and photocatalytic water treatment

Photo and photocatalytic water treatment provide possible solutions to the water crisis [1, 2]. They are water treatment methods without addition or generation of hazardous and harmful materials. Complete degradation of pollutants to carbon dioxide, water and mineral acid is achievable by photocatalysis. However, their application is limited by difficult control and high operation cost, mainly due to absence of robust models relating reactor performance and design and operating parameters, a result of complex nature and time-consuming experimental verification of these processes [3].

Computational Fluid Dynamics (CFD) is able to simulate turbulent flow with acceptable accuracy; hence, it is useful in simulating photo-disinfection reactors, which usually operate in turbulent regime due to high water flow rate in industrial applications [4]. Researchers have applied CFD simulation to various reactors, and also tried to model this complicated process. Various light intensity distribution models based on photonic laws and light emission models have been proposed and validated [5-7]. Turbulence models have been modified to better describe the water flow pattern in the reactors [8]. Approaches describing microorganism particle motion have been studied [9]. However, in-depth analysis of design and operating parameters on overall reactor efficiency is still lacking. Comparison of different reactor designs and operating conditions, and subsequently optimization of photo-disinfection process is still far from complete.

Since photo-disinfection process is very complex in nature, it is not possible to describe this process using a simple model such as algebraic equations. With large amount of simulation results, it is possible to utilize data-driven modeling techniques such as Artificial Neural Network (ANN) and Genetic Programming (GP) to establish models relating input parameters and reactor performance. There have been research papers utilizing CFD simulation data as the training data set for model building [10]. The modeling accuracy can be assessed by comparing the errors of different models. After construction of models, photo-disinfection reactors can be optimized to find the optimal values of design and operating

variables for different requirements, through optimization tools. The validity of these models can be further tested by comparing the optimal solution sets and the simulation results of these optimal solutions.

Photocatalytic degradation of pollutants in water is even more complex than photo-disinfection due to addition of a new phase – the solid catalyst. Therefore, its modeling is expected to be more difficult. Currently, modeling of photocatalytic water treatment usually utilizes a target pollutant whose concentration is easy to measure, such as different kinds of dyes for ease of light absorbance measurement in UV-visible spectrometers. Dyes have different affinity to the photocatalyst particles due their surface charges in different environment. The degradation is therefore much dependent on both dye and catalyst properties. It is also possible that the change in the catalyst properties during the photocatalytic process would affect the reaction. Modeling of photocatalytic water treatment still has much room for research and provides basis for future industrial applications.

1.2. Objectives of this thesis work

This thesis work focuses on modeling and optimization of photo and photocatalytic water detoxification and disinfection processes. Specific objectives of this work are as follows.

- Propose a new simulation methodology for the photo-disinfection process. It should be more flexible and computationally faster than the conventional one, named as **S**imultaneous **U**V fluence **R**ate and **F**luid dynamics (SURF) method in this work [9].
- Use the new simulation methodology to simulate water photo-disinfection reactors of different lamp arrangements, reactor layouts and sizes under different operating conditions, and then analyze the relationship between these design and operating parameters and the reactor performance.
- Apply ANN and GP to build models relating reactor performance and design and operating parameters. Compare these two modeling tools based on their modeling accuracy and generalization ability, i.e. ability to predict output from new input sets.
- Use the ANN and GP models for multi-objective optimization to find optimal reactor design and operating conditions, and simulate the optimal solutions found using CFD to validate the models further.

- Investigate photocatalytic degradation of methylene blue under different conditions, experimentally and then develop a suitable model based on the measured data.

1.3. Structure of this thesis

There are 8 chapters in this thesis work. A brief introduction and a summary of the thesis objectives are provided in Chapter 1. This is followed by a detailed literature review on modeling and optimization of photo and photocatalytic water treatment processes in Chapter 2. Chapter 3 presents the proposed simulation methodology; some simulation parameters and results are also included. In Chapter 4, simulation data of single-lamp photo water disinfection reactors are presented. The effects of design and operating variables are discussed. Performance of water photo-disinfection reactors with different lamp arrangements is compared in Chapter 5. Based on the simulation data in Chapters 4 and 5, ANN and GP are utilized to model the water photo-disinfection reactors in Chapter 6. Multi-objective optimization is applied to find design and operating conditions for the most energy-efficient reactor. The optimal solution sets are then verified via CFD simulation to compare the generalization ability of ANN and GP models for this application. Chapter 7 provides the details for the photocatalytic degradation of methylene blue by TiO_2 . The effects of lamp selection, catalyst concentration and initial methylene blue concentration are discussed. The conclusions drawn from this research and suggestions for future work are presented in Chapter 8.

Chapter 2

Literature Review

2.1. Introduction

Photo and photocatalytic water treatment technologies have attracted much research attention to counter water crisis. This chapter reviews these processes based on the research papers published in last few decades. Various ways of water disinfection are introduced in Section 2.2. This is followed by review of CFD applications in water photo-disinfection reactors in Section 2.3. The models used to describe the light radiation distribution and fluid dynamics are presented in Sections 2.4 and 2.5 respectively. Different aspects of photocatalytic water treatment are reviewed in Section 2.6; they include reactor design, catalyst type and loading, and modeling of this process. The data-driven modeling techniques used in this work to construct models for water photo-disinfection reactors are discussed in Section 2.7. Summary of this chapter is given in the last section.

2.2. Water disinfection

Water crisis has been a serious threat to human development. In 2008, there were more than 884 million people around the world lacking access to safe drinking, according to a joint report by the World Health Organization (WHO) and the United Nations Children's Fund (UNICEF) [11]. One major threat posed by unsafe drinking water is waterborne diseases. A United Nations' report stated that half of the world's hospital beds are occupied by patients suffering from diseases due to contaminated water at any time [12]. These diseases are the result of different water pollutants, such as microorganisms (bacteria, viruses and protozoa), solid particles and both organic and inorganic chemicals. To make water safe for human consumption, these pollutants need to be removed. Although with the help of developed countries and various international organizations, the percentage of people lacking safe drinking water access has been reduced greatly in recent decades, this problem is still a serious challenge. Most of these people lacking access to safe drinking water are in undeveloped countries, as shown in Figure 2.1, where the population is increasing rapidly, increasing the demand for clean water and worsening the situation further. In addition, industrialization and pollution brought by it, deforestation and global warming reduce the

fresh water source. Therefore, researchers are striving to find new water treatment processes which are effective, reliable and also economically feasible. Water purification, the process which removes pathogens and other harmful materials from water, is a crucial process in water treatment and is attracting much attention [13].

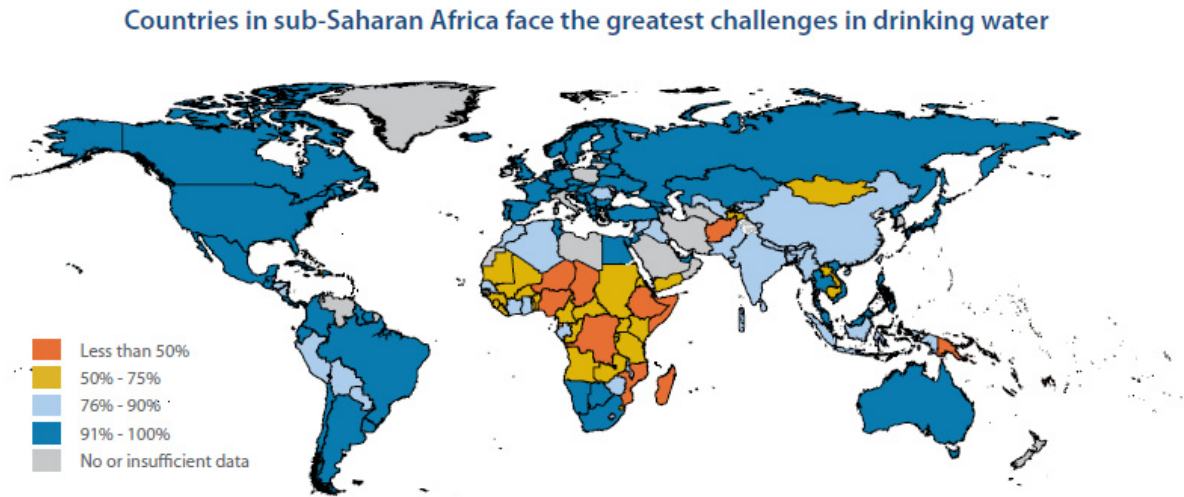


Figure 22 Drinking water coverage, 2006

Figure 2.1 Coverage of safe drinking water around the world [11]

Water disinfection is the process which removes pathogens from water. Harmful microbes include viruses and bacteria, such as *Escherichia coli*, *Campylobacter* and *Shigella*, as well as parasitic protozoa, such as *Giardia lamblia*. Boiling or evaporation can remove all of these pathogens, but the cost is too high for mass production. Filtration and addition of chemicals are the conventional disinfection methods. Advancement in technology enables scientists to utilize new methods to remove the waterborne pathogens, such as ultra-violet (UV) and photocatalytic disinfection.

2.2.1. Conventional water disinfection

Conventionally, water disinfection is achieved through filtration and chlorination. Some large microbes can be filtered out by conventional filters such as rapid sand and activated carbon. Recent advancements in membrane technology make removal of much smaller microorganism particles possible. However, most microorganisms can go through conventional filters and need to be removed in later steps. Modern membranes can block microorganisms, but growth of microorganisms on membrane and subsequently blocking of

the membrane pores is a serious problem for membrane filtration. One common disinfection method is chlorination, which has been used since 19th century [14]. Chlorine is a strong oxidant. It is effective against most of the microbes and able to kill them rapidly. In addition to its high effectiveness, chlorination offers prolonged residue disinfection effect compared to other technologies. Sodium hypochlorite is normally used instead of dangerous and toxic chlorine gas. However, chlorination produces possible carcinogenic disinfection by-products (DBPs). Therefore, alternative disinfection methods have been explored. For example, ozone (O₃) and hydrogen peroxide (H₂O₂) have been proposed to replace chlorine compounds. Both methods produce much less DBPs, in terms of both quantity and harmfulness. However, it is difficult to dissolve O₃ in water while H₂O₂ disinfection is slow and increases water acidity. In addition, both methods do not have prolonged disinfection effect. For these reasons, UV disinfection is gaining attention as it does not use or generate hazardous chemicals [15].

2.2.2. UV disinfection

UV radiation is effective in killing both viruses and bacteria. UV radiation with the wavelength below 260 nm is able to damage the chemical bonds of deoxyribonucleic acid (DNA) of microbes, thereby inhibiting their reproduction [1]. A few industrial water plants have utilized this technology, such as the NEWater plants in Singapore. The cutaway view of the UV water disinfection reactors in the NEWater plants is shown in Figure 2.2. However, UV disinfection suffers from drawbacks such as high operation cost, low reliability, difficult maintenance and regrowth of microbes. Solutions to these problems include addition of a photocatalyst to utilize light of longer wavelengths [2, 16, 17], addition of hydrogen peroxide to produce hyper-reactive hydroxyl radicals, design of more efficient reactors and optimization of operating conditions. An accurate and robust model of UV disinfection reactors is therefore important as it provides the foundation for the latter two solutions. The main obstacles to the establishment of such a model are the complicated trajectories of small microorganism particles due to high turbulence and non-uniformity of the UV fluence rate field in the reactor, as well as poorly-defined responses of microorganisms to UV radiation. Researchers have devoted much effort in establishing an efficient method to determine reactor performance quickly. However, experimentation is highly time-consuming. Simulation of UV disinfection reactors using computational software takes 5-10 days. Deep

insight into the relationship between reactor performance and decision variables is also lacking.



Figure 2.2 Cutaway view of UV disinfection reactors in NEWater plants, courtesy of Dr. Xiong Zhigang

2.3. Computational fluid dynamics simulation

Careful experimentation is the most accurate and convincing method to study photo disinfection reactors. However, it is usually time-consuming, especially for disinfection experiments, where culturing microorganisms usually takes days. It is common to take weeks to get just one data point when the experiment has to be repeated to minimize random error [3]. The error in experimentation is also usually high. Experimental verification is expensive as modeling and optimization in design of reactors involves many reactors and experiment sets. Scaling-up of reactors from lab-scale to industrial-scale costs a lot. To save time and money, computational simulation of photo and photocatalytic reactors have been explored by researchers. Small-scale reactors are constructed, and their experimental data are compared with simulation results. If both results agree, it is reasonable to deduce that simulation results of other reactors under other operating conditions will be close to corresponding actual experimental data. Computational Fluid Dynamics (CFD) software packages have been employed to assist analysis of photo disinfection reactors [4, 9, 18-23]. Advancement in computing technology has enabled utilization of more sophisticated fluid dynamics models and faster calculations.

In the previous studies on photo and photocatalytic reactor simulation, UV fluence rate field was established using a radiation model [7, 24-26]. This field was incorporated into the fluid computational domain. Microorganisms were considered either as a discrete phase

(Lagrangian approach) or a soluble reacting species (Eulerian approach) [27]. However, these studies did not fully analyze the effects of design and operating variables, such as reactor shape and size, water flow rate, UV intensity and photocatalyst specifications, on the reactor performance. Such effects are critical in the design and optimization of both UV disinfection and photocatalytic processes. Since both UV intensity and fluid dynamics calculation are computationally very intensive, this thesis work develops a more efficient simulation method which also enables independent analysis of various factors affecting the reactor performance.

2.4. UV fluence rate field

Establishment of an accurate UV fluence rate field is one of the pre-requisites of an accurate model for photo and photocatalytic reactors. However, it is usually difficult to measure the UV intensity distribution *in situ* directly. Introducing UV detectors inside the reactors would change the flow pattern. Although this is unlikely to change the UV fluence rate field much, UV detectors are usually too large to get an accurate value for local UV fluence rate, especially at places close to the lamps where the highest UV intensity occurs. Biodosimetry is usually used as an indirect way to measure UV fluence. Biodosimetry utilizes well-calibrated bacteria whose UV response has been established. The disinfection effect of the reactor is then compared with the UV response curve to get the average UV fluence rate value. It is obvious that this method cannot provide detailed data for the UV fluence rate distribution inside the reactor. Therefore, the UV fluence rate fields inside photo reactors are usually established based on photonic laws and power distribution models of lamps [9]. The accuracy of such models is tested by comparing the calculation results with the measured light radiation intensity around the lamp as well as overall average values obtained by biodosimetry.

2.4.1. Photonic laws

In photo and photocatalytic water treatment reactors, reflection and refraction occur at the interfaces of different media, as shown in Figure 2.3. Each medium has its own light absorption coefficient (n). Photonic laws governing these three phenomena have already been well established [25].

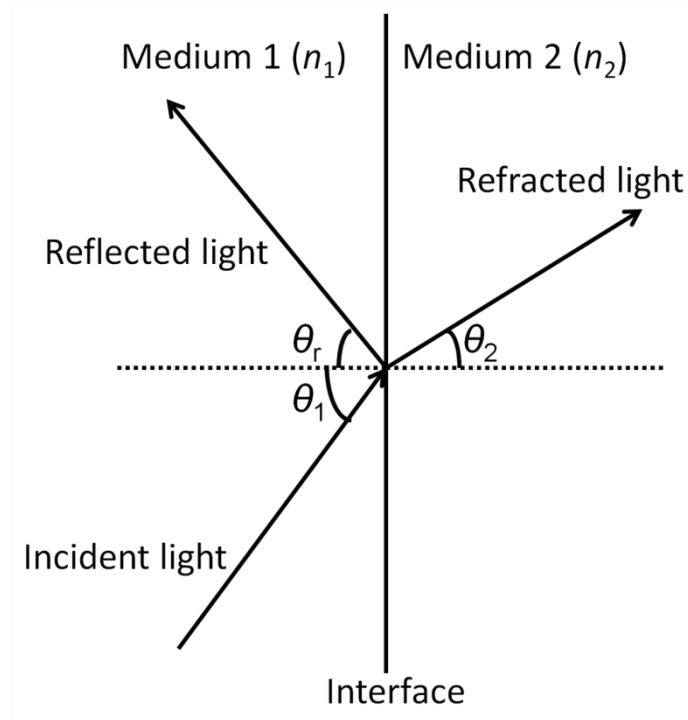


Figure 2.3 Schematic of reflection and refraction

Snell's law describes the refraction phenomenon quantitatively. The relationship between incidence angle (θ_1) and refraction angle (θ_2) is given by:

$$n_1 \sin \theta_1 = n_2 \sin \theta_2 \quad \text{Equation 2-1}$$

where n_1 and n_2 are refractive indices of respective medium.

Fresnel's law calculates the reflection phenomenon. The fraction of light reflected back to the incidence medium R is calculated by:

$$R = \frac{1}{2}(r_{\perp}^2 + r_{\parallel}^2) \quad \text{Equation 2-2}$$

where $r_{\perp} = \frac{n_1 \cos \theta_1 - n_2 \cos \theta_2}{n_1 \cos \theta_1 + n_2 \cos \theta_2}$ and $r_{\parallel} = \frac{n_2 \cos \theta_1 - n_1 \cos \theta_2}{n_2 \cos \theta_1 + n_1 \cos \theta_2}$

Light absorption by each medium can be calculated using the Beer-Lambert's law. The relationship between incidence fluence rate P_0 and measured fluence rate P transmitted through a material with absorption coefficient of α and thickness of x is given by:

$$P = P_0 \exp(-\alpha x) \quad \text{Equation 2-3}$$

These three laws provide the basis for UV fluence rate field calculation inside photo and photocatalytic reactors.

2.4.2. Lamp models

It is important to find an accurate model to describe the distribution of light intensity emitted by the lamps in the photo and photocatalytic reactors. The simplest model is the **Infinite Line Source (ILS)** model [5]. This model assumes that the lamp is a linear source, emitting light only in the plane normal to the lamp axis uniformly in 360°. The light absorption by air in the quartz sleeve is neglected due to the much lower light absorption by air compared to other media (such as water and quartz). Fluence rate, P at a point with radial distance r from the axis of the lamp is given by:

$$P(r) = \frac{P}{2\pi r L_2} \exp[\alpha(r - r_L)] \quad \text{Equation 2-4}$$

where P is the total output power, L_2 is the lamp length, r_L is the lamp sleeve radius, α is the absorption coefficient of the medium. ILS model is simple but inaccurate, especially at the two ends of the reactor. However, if the reactor length is much larger than its diameter, the accuracy of this model is still acceptable as the proportion of volume of low accuracy is limited.

An improved version of lamp model is the **Multi-Point Source Summation (MPSS)** model [6], which assumes that emission of a linear lamp is equivalent to that of n point sources spaced equally along the axis of the lamp. The output power P is evenly distributed among these point sources. All these point sources emit radiation in all directions uniformly. The overall fluence rate received by any point inside the reactor is the sum of fluence rates received from all point sources. As n increases, accuracy of the model increases. This model is computationally more intensive than the ILS model especially when n is large, but offers higher accuracy [9].

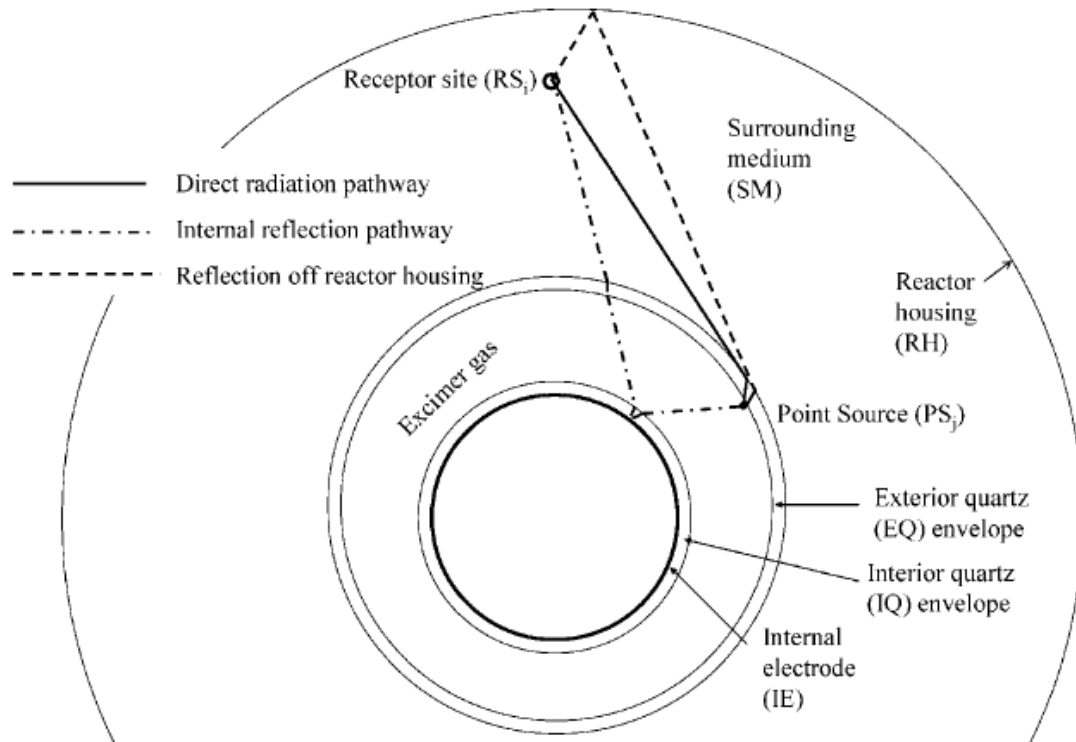


Figure 2.4 Schematic for the SPACE model [7]

There have also been other more sophisticated models such as the SPACE (Surface Power Apportionment for Cylindrical Excimer lamps) proposed by Naunovic et al. [7]. This model is similar to the MPSS model in that the radiation received by any reception point is the sum of a large number of point sources. However, the point sources in the SPACE model are located at the cylindrical surface of the lamp, rather than along the axis of the lamp in the MPSS model. Refraction and reflection by the internal surface of the quartz jacket and the external housing are taken into consideration, as shown in Figure 2.4. The SPACE model is computationally even more intensive than the MPSS model, and yet does not offer significant improvement in accuracy, especially when the number of point sources is large.

Duran et al. established and experimentally evaluated a volume-finite model for fluence rate distribution in annular photo-reactors [26]. This model incorporated Hg vapour inside the lamps in the computational domain. This modification showed better approximation in calculating UV fluence rate inside the reactor than the MPSS model. CFD software FLUENT was used to assist the calculation.

Elyasi and Taghipour integrated photonic laws for modeling the UV fluence rate distribution in a medium [28]. The model considers refraction and reflection along the light pathway through the body of the UV lamp and sleeve, as well as the reflections from other sources, such as the reactor body. The measured boundary conditions are applied to realistically simulate the fluence rate around the radiant source, in particular, in the zone closest to the radiant source. Different low-pressure UV lamps were tested under different operating conditions using photodiodes and a radiometer to measure the local UV fluence rate. The experimentally measured fluence rate was in good agreement with the simulation results of the model.

Chen et al. used FLUENT to simulate UV disinfection processes in a closed-conduit reactor [29]. An improved low Reynolds' number $k-\epsilon$ fluid dynamics model and P-1 radiation model were used. The results agreed with the experimental data well. Effects of wall reflection were analyzed under different conditions. Wall reflection was more influential when the disinfection is high.

2.4.3. Light distribution in photocatalytic reactors

Fluence rate distribution is important in photocatalytic water treatment reactors. The size of solid catalyst particles is usually close to UV radiation wavelength; hence, absorption and scattering of light by the solid particles are quite complicated.

Cabrera et al. studied absorption and scattering coefficients of TiO_2 particles suspended in water [30]. Several physical and optical parameters of 6 commercial powders were analyzed. Agglomeration of these powders in water suspension made simplification of geometric optics applicable. Dependence of mass specific extinction coefficients (sum of absorption and scattering) on wavelength was analyzed.

Li Puma et al. established a model for photocatalytic pesticide oxidation in a slurry annular reactor. TiO_2 was the catalyst and isoproturon was the target pollutant [23]. MPSS model was used to simulate light emission of the lamp. A novel six-flux absorption-scattering model was proposed to estimate the radiation field in the annular reactor. Both absorption and scattering were taken into consideration. The model parameters were obtained by fitting the solution from Monte-Carlo approach to the model equations. The fluid was assumed to be a

fully developed laminar flow. Reaction rate constants were fitted to a Langmuir-Hinshelwood kinetic model. Despite a few assumptions and simplifications, Li Puma et al.'s model was satisfactory when applied to the photocatalytic oxidation of isoproturon.

Boyjoo et al. used CFD to simulate UV distribution in a slurry water reactor with multiple lamps [31]. Light scattering and absorption coefficients of Degussa P25 TiO₂ were measured and calculated. The radiation model in FLUENT was used to simulate the lamps. An optimal distance between lamps was found to exist for different design parameters. However, due to dimension of the probe, it is not possible to measure the region closest to the lamp. This region is the most important since its UV fluence rate here is much higher. Therefore, the applicability of this work is limited.

2.5. Fluid dynamics models and CFD simulation

There have been several studies on simulation of photo and photocatalytic reactors in the laminar regime [23, 32]. It is possible to get analytical solution for laminar flow velocity profile. Such a study is useful in kinetic studies of photo-disinfection and photocatalytic processes. However, since most industrial reactors operate in turbulent regime to utilize better mixing brought by turbulence, most of the reactors analyzed in research have turbulent flow [4, 9, 20, 21, 24, 33-35]. Turbulence is complex and usually cannot be described by equations which offer analytical solution. In most cases, it is described by approximate models which have applicable range (such as viscosity or Reynolds' number) [27, 36].

In CFD simulation, method of discretization is usually utilized to solve for the velocity profile in turbulent fluid. The computational domain is meshed into a large number of small control volumes. Governing equations for mass, momentum and energy transfer of all these small volumes are established based on appropriate fluid dynamic models [37-39]. These equations along with user-supplied pre-defined boundary conditions are solved numerically on digital computers. Smaller control volume gives calculation result of higher accuracy but requires longer calculation time. Several commercial software packages have been developed, including PHOENICS by CHAM Ltd, FLUENT by ANSYS Inc and STREAM by Software Cradle Co. Among them, FLUENT is the one most widely used in the literature [9, 20, 21, 26, 28]. Previous studies have shown that this program provides good agreement between simulation and experimental results [20, 21].

2.5.1. The standard k - ε model

CFD software usually has a few built-in fluid dynamic models. Commonly used turbulence models in photo and photocatalytic water disinfection simulation are normally based on the standard k - ε model [40]. In this model, it is assumed that the flow is fully turbulent and the molecular viscosity is negligible. The standard k - ε model is built around two key variables: the turbulence kinetic energy k and turbulence dissipation rate ε , thus giving the model its name. These two variables are defined by the following transport equations:

$$\frac{\partial}{\partial t}(\rho k) + \frac{\partial}{\partial x_i}(\rho k u_i) = \frac{\partial}{\partial x_j}[(\mu + \mu_t) \frac{\partial k}{\partial x_j}] + G_k + G_b - \rho \varepsilon - Y_M + S_k$$

Equation 2-5

$$\frac{\partial}{\partial t}(\rho \varepsilon) + \frac{\partial}{\partial x_i}(\rho \varepsilon u_i) = \frac{\partial}{\partial x_j}[(\mu + \frac{\mu_t}{1.3}) \frac{\partial \varepsilon}{\partial x_j}] + \frac{1.44 \varepsilon}{k} (G_k + C_{3\varepsilon} G_b) - 1.92 \rho \frac{\varepsilon^2}{k} + S_\varepsilon$$

Equation 2-6

Here, turbulence viscosity, $\mu_t = 0.09 \rho \frac{k^2}{\varepsilon}$, S_k and S_ε are user-defined source terms,

generation of turbulence kinetic energy due to the mean velocity gradient, $G_k = -\rho u_i' u_j' \frac{\partial u_j}{\partial x_i}$,

generation of turbulence kinetic energy due to buoyancy, $G_b = -\frac{1}{\rho} \left(\frac{\partial \rho}{\partial T} \right)_p \frac{\mu_t g_i}{0.85} \frac{\partial T}{\partial x_i}$, g_i is the

component of gravitational vector in the i th direction, $C_{3\varepsilon} = \tanh \left| \frac{v}{u} \right|$, v is the component of

the flow velocity parallel to the gravitational vector, u is the component of the flow velocity perpendicular to the gravitational vector, and Y_M is the compressibility effect in high-Mach-number flows, which normally is not applicable in the area of this research.

2.5.2. The realizable k - ε model

An improved version of the standard k - ε model is the realizable k - ε model, which modifies the standard k - ε in two ways: the turbulent viscosity μ_t and the turbulence dissipation rate ε [8]. This model satisfies certain mathematical constraints on the Reynolds

stresses, and is consistent with the physics of turbulent flows; therefore, it is called “realizable”. In this model, Equation 2-6 is changed to:

$$\frac{\partial}{\partial t}(\rho\varepsilon) + \frac{\partial}{\partial x_i}(\rho\varepsilon u_i) = \frac{\partial}{\partial x_j} \left[\left(\mu + \frac{\mu_t}{1.2} \right) \frac{\partial \varepsilon}{\partial x_j} \right] + 1.44 \rho S \varepsilon - 1.9 \rho \frac{\varepsilon}{k + \sqrt{\nu \varepsilon}} + 1.44 \frac{\varepsilon}{k} C_{3\varepsilon} G_b + S_\varepsilon$$

Equation 2-7

Here, $C_{3\varepsilon} = \max\left[0.43, \frac{\eta}{\eta + 5}\right]$, $S_\varepsilon = \frac{k}{\varepsilon \eta}$, turbulence viscosity $\mu_t = C_\mu \rho \frac{k^2}{\varepsilon}$,

$C_\mu = \frac{1}{4.04 + \sqrt{6} \cos \phi} \frac{k U^*}{\varepsilon}$, $U^* = \sqrt{S_{ij} S_{ij} + (\Omega_{ij} - 4 \varepsilon_{ijk} \omega_k)^2}$, and Ω_{ij} is the mean rate of rotation

tensor viewed in a moving reference frame with the angular velocity ω_k .

Sozzi and Taghipour compared the accuracy of the above two models and another widely used turbulence model, the Reynolds stress model (RSM) [20]. The simulation results were compared to the experimental particle image velocimetry (PIV) data. The realizable k - ε model was found to be the most accurate as it offers the lowest error in particle velocity. Therefore, the realizable k - ε model was chosen as the fluid dynamics model for all the later part in this thesis.

2.5.3. Approaches to describe particle motion trajectories

Two different approaches to describe the microorganism particle motion in the reactor have been used to study the UV disinfection process: the Lagrangian approach which considers microorganisms as a discrete phase and the Eulerian approach which considers them as a soluble reacting species [27]. There have been studies showing that both approaches yield similar results if the effluent plane in the Eulerian approach has been defined appropriately [21]. Microorganism particles, especially bacteria, contain high amount of water. Their densities and photonic properties are close to that of water in photo disinfection reactors. It is unlikely that the microorganisms would change the macroscopic properties of water. Thus, the Eulerian approach is a good approximation. However, photocatalysts are insoluble solid particles which are very different from water in terms of density, light absorption and scattering, and other physical properties. Therefore, using the Lagrangian approach is more reasonable for photocatalytic reactors. In this thesis work, the

Lagrangian approach is used to define the motion trajectories of both microorganism and photocatalyst particles in the water treatment reactors.

2.6. Data-driven modeling

Data-driven modeling techniques have been employed to mimic complex relationships in complicated systems. The training data for these models are usually obtained from real-life data or computer simulations. Both Artificial Neural Network (ANN) and Genetic Programming (GP) have been found to be able to construct models for various engineering and other application with good accuracy [41]. Some applications include blast furnace [42], hydrogen production [43], cyclones [10, 44, 45], moving bed reactors [46], nucleation process [47], waste water treatment [48, 49] and natural gas hydrates formation [50]. The modeling accuracy depends on both modeling algorithm and the nature of the processes. GP performs better than ANN in some occasions such as moving bed reactors [46, 51, 52], while the opposite is observed in some other cases such as drug release [53, 54]. Besides their ability to model and predict the complex processes, the developed ANN and GP models can be subsequently combined with suitable optimization tools to find the optimal design and operating parameters.

Some researchers have worked on modeling of photocatalytic degradation by ANN. Caliman et al. analyzed photocatalytic degradation of Alcian Blue 8GX by Degussa P25 TiO₂ [55]. Effects of initial dye concentration, catalyst concentration, initial pH value and H₂O₂ concentration were analyzed. An ANN was constructed to model the degradation process and optimal reaction conditions were found. Dutta et al. analyzed the application of ANN in photocatalytic degradation modeling of active dye using Hombikat TiO₂ catalyst [56]. It was shown that selection of transfer functions, algorithms and number of neurons was vital for model accuracy.

Various simulation software packages have been used to supply training data for ANN and GP modeling. Safikhani et al. used ANN to fit a model for cyclone performance with training data obtained from FLUENT simulation [44]. Relationship between design parameters and cyclone performance was analyzed. These researchers further used multi-objective optimization through genetic algorithm to find the Pareto-optimal front for collection efficiency and pressure drop [10]. Fahmi and Cremaschi used ANN to model and optimize superstructure of biodiesel production plant with training data obtained from

HYSYS simulation [57]. Elsayed and Lacor used modeling tools including ANN, desirability functions and genetic algorithms to model and optimize cyclone performance based on CFD simulation data [45]. ANN offered good modeling accuracy. Song et al. used ANN to model airflow and temperature distribution in data centres based on training data from CFD simulations [58]. The model worked well. Genetic algorithm was then applied to minimize the total energy cost.

2.7. Photocatalytic water treatment

Heterogeneous photocatalysis by semiconductors such as titanium dioxide (TiO_2) is a promising technology for water purification [59]. It can degrade pollutants which are difficult to degrade by other methods, such as benzene, dyes and pesticides, as well as complex mixture of water contaminants in industrial and domestic wastewater [60-62]. In addition, it is able to degrade chemical contaminants and microorganisms completely into carbon dioxide, water and mineral acid [63]. Figure 2.5 shows the mechanism of photocatalytic degradation. When the electrons in the valence band of the semiconductor absorb photons with energy greater than the band gap (ΔE) of this material, these electrons become excited and reach conduction band, leaving positively-charged holes in the valence band. Besides recombination of this electron-hole pairs, some of the holes and excited electrons react with water and oxygen molecules adsorbed on the surface of the catalyst independently. The positively-charged hole is a strong oxidizing agent, which is able to oxidize water molecule adsorbed on the surface of the catalyst into hyper-reactive hydroxyl free radicals ($\cdot\text{OH}$). These hydroxyl radicals are the main agent that attack the chemical bonds in the chemical pollutant molecules or microorganism cell walls to degrade them [64, 65]. Oxygen molecules dissolved in water can be reduced by the excited electrons to form peroxide radicals ($\text{O}_2\cdot$), which are also able to degrade water pollutants.

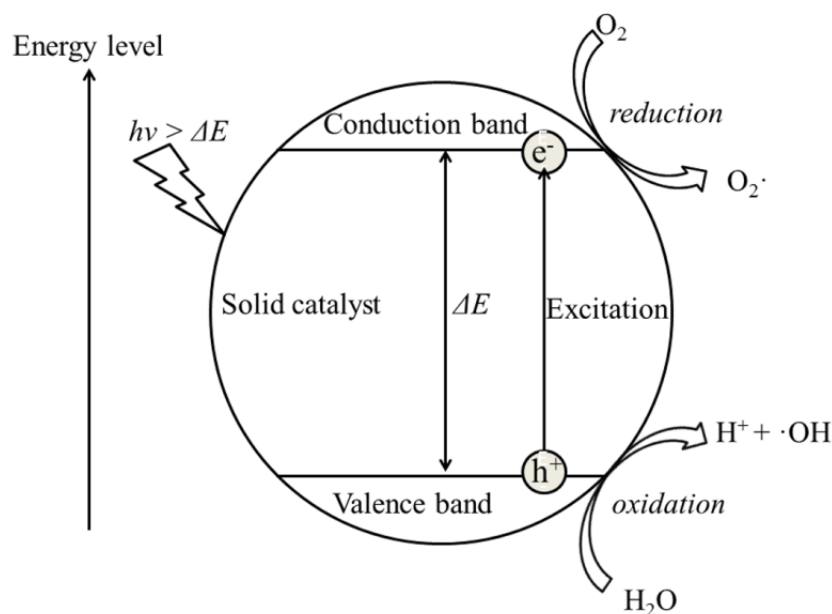


Figure 2.5 Mechanism of photocatalytic reaction

Since both hydroxyl and peroxide radicals are too reactive to travel for long distance in water, the photocatalytic detoxification and disinfection processes occur close to the surface of the photocatalyst. That means, in photocatalytic detoxification process, only pollutant molecules close to the surface of the solid catalyst are degraded. Similarly, adsorption of solid catalyst particles on the surface of microorganisms is an important step in photocatalytic disinfection process, where chemical bonds in the molecules of cell walls of bacteria are attacked by the radicals, disrupting the cell wall structure, exposing the interior of cells and killing them [3]. The organic materials released by the inactivated microorganisms are then further degraded by the photocatalyst.

In addition to complete mineralization, photocatalytic processes have another merit of higher quantum efficiency. The bandgap energy of photocatalysts is usually lower than the UV radiation required in photo disinfection. For example, un-doped titanium oxide (TiO_2) has a band-gap corresponding to the UV radiation of wavelength at 365 nm. UV disinfection requires radiation with wavelength shorter than 260 nm. Photocatalytic disinfection is thus able to utilize light radiation of lower energy. Photocatalysts can be doped to lower its bandgap energy, utilizing more energy from the emission spectrum of lamps and even solar radiation can be utilized directly.

The main disadvantage of photocatalytic disinfection is that it is essential to separate the photocatalyst particles from water after disinfection and detoxification process in slurry reactors. The size of photocatalyst particles is usually small (micron-scale or smaller) in order to achieve high surface area available for adsorption and reaction, but it increases the cost of separation. To overcome this problem, photocatalysts with larger particle size and similar activity have been suggested either via more sophisticated morphology or improved quantum efficiency. Composites of photocatalyst and magnetic materials have also been explored to assist separation via magnetic force [66]. To completely avoid separation of photocatalysts, disinfection reactors with photocatalyst immobilized on various media have been analyzed [67-69]. The immobilized photocatalysts are usually coated on the surface of the quartz tubes which house the lamps. However, such reactors reduce the reaction surface area and face the problem of reduced performance compared to slurry reactors. More reactors are thus required to treat the same amount of polluted water.

2.7.1. Photocatalysts

Degussa P25 TiO₂ has been the research benchmark catalyst for photocatalytic water treatment [70]. It is polycrystalline, consists of 80% anatase and 20% rutile phase by mass. Its average particle size is 25 nm and specific surface area is 50 m²/g. There has been effort to find more effective photocatalyst [17]. One possible development for photocatalytic water purification is to utilize sunlight as the light source [2]. However, the band gap of TiO₂ corresponds to ultra-violet wavelength, which is only a small fraction of natural sun radiation. Therefore, new semiconductors with smaller band gap such as ZnS [71], CdS [72] and graphene and its derivatives [73, 74] have been developed. Another aspect of improving photocatalyst efficiency is to delay the recombination of electron-hole pairs [75]. Composite materials have also been studied to utilize merits of different materials, such as TiO₂-silica [76] and reduced graphene oxide-CdS-ZnO [77].

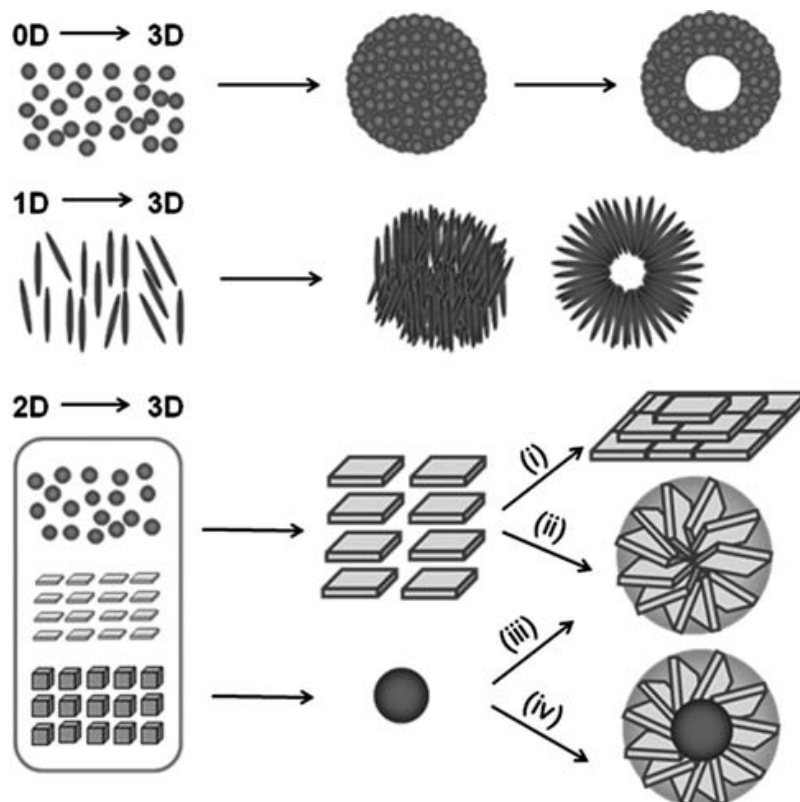


Figure 2.6 Schematic of various pathways to form 3-D porous photocatalysts [17]

Since majority of photocatalytic processes occurs close to the surface of the catalyst, morphology of the catalyst is crucial for high photocatalytic performance. Various methods have been proposed to synthesize catalyst of higher specific surface area [78-81]. Figure 2.6 shows some examples of 3-D porous materials which offer high specific surface area and hence better photo-activity. Most photocatalysts are very small in size to obtain high specific surface area. Hence, it is energy intensive to remove them from reaction suspension after degradation. Different reactor designs have been proposed to immobilize photocatalyst without compromising overall performance [68, 82, 83].

Various materials have also been doped into or coated on the surface of TiO_2 to utilize light of longer wavelength or enhance photocatalytic performance by other means, such as delay of electron-hole pair recombination and increase in specific surface area. Nikazar et al. researched on photocatalytic degradation of azo dye acid red 114 with TiO_2 supported on clinoptilolite (a natural zeolite) prepared by solid state dispersion [84]. They suggested that ease of transfer of hydroxyl radicals from TiO_2 to the zeolite was the reason for the enhancement in photo-activity.

Chuang and Chen coated TiO₂ on Ag and Ag-Ni [66]. Metal cores and oxide shells were observed. It was shown that both doping agents enhanced the photocatalytic activity of TiO₂ under visible light radiation. It was observed that doped catalysts have higher adsorption of Rhodamine B than pure TiO₂, regardless of their smaller specific areas. It was suggested that the electrons in the metal cores were excited by visible light and then diffused to the oxide shells to facilitate photocatalysis. When subject to UV radiation, pure TiO₂ was more efficient, possibly due to the smaller TiO₂ content and amorphous structures of the doped catalyst. It is easier to separate the TiO₂-Ag-Ni composite from water by utilizing magnetic force.

Dunnill et al. fabricated sulphur-doped TiO₂ thin films on glass substrate via chemical vapour deposition of titanium tetrachloride, ethyl acetate and carbon disulphide [85]. Anatase TiO₂ was formed. Such thin film was found to be good material for self-clean products due to higher photo-activity (especially under white light source with *E. coli* as the target microorganism) and super-hydrophilicity.

Sa et al. doped various amounts of different metals on TiO₂ via controlled photo-deposition of metal salts on TiO₂ nanoparticles and studied the effects on the performance of photocatalytic reduction of nitrate [86]. It was found that doping of Ag would have better improvement on both selectivity and activity over other metals (Cu and Fe). Particle size, metal choice, hole scavenger and its concentration affected the performance.

Van Grieken et al. immobilized Ag-doped TiO₂ on quartz glass substrate [87]. TiO₂ was coated on substrate using dip-coating, while doping of Ag was accomplished by photocatalytic reduction of Ag⁺ ions in solution using TiO₂ coated substrate. The authors found that such a composite material had lower photo-bactericidal activity in slurry system than P25 TiO₂, possibly due to the change in microscopic structure by thermal treatment required for Ag particles stabilization. However, in immobilized systems, an optimal amount of Ag doping was observed and such systems exhibited better disinfection activity than ordinary TiO₂ system.

Akhavan and Ghaderi synthesized Ag-TiO₂ nano-composite layer on rough mesoporous anatase TiO₂ layer via sol-gel method [75]. A good enhancement in disinfection of *E. coli* compared to pure TiO₂ and pure Ag, both with and without UV radiation was

observed. The authors suggested that this is mainly due to delay of recombination of photo-excited electrons and holes in TiO₂.

An et al. synthesized iron-coated TiO₂ nanotubes by treating hydrogen titanate nanotubes with Fe(OH)₃ sol [88]. Methyl orange was used to test its photocatalytic degradation performance. Such catalyst exhibited better thermal stability because the Fe₂O₃ particles formed reinforced the nanotube structure. Photocatalytic performance also improved as Fe₂O₃ acted as electron acceptors.

Quinonez et al. synthesized Au/Pd modified TiO₂ thin films deposited on ITO (SnO₂:In) using Doctor Blade method [89]. This composite material was found to be more effective in removing methylene blue from water, possibly due to reduction in electron-hole pair recombination rate.

Wang et al. synthesized Nd-doped TiO₂ hollow spheres using carbon spheres as the template and Nd-doped TiO₂ nanoparticles as the building blocks [90]. A red-shift was observed in the absorption spectrum of such hollow spheres compared to pure TiO₂. Photocatalytic activity was enhanced under visible light due to reduction in band-gap energy.

Chen et al. synthesized Ag₂O-modified TiO₂ nano-sheets and tested their adsorption and degradation ability using methylene blue as the target pollutant [91]. A small amount of Ag₂O added was found to be enhancing both adsorption and degradation ability. Photocatalytic performance of this catalyst is enhanced by both increase in specific surface area and presence of Ag₂O as the electron sink to suppress electron-hole pair recombination.

2.7.2. Photocatalytic water treatment reactors

The choice of light sources and their arrangements are important in photocatalytic reactor design. Artificial light sources especially UV lamps have been employed in research for their consistency compared to natural radiation. Ordinary light bulbs have also been utilized. Direct utilization of solar radiation to activate photocatalysts has been suggested but the photocatalytic efficiency is low, limiting its application in large-scale operation [92-96]. Solar collectors were essential to improve the quantum efficiency in those reactors.

UV water disinfection reactors and photocatalytic water disinfection reactors using lamps as the light source, can be classified into three types according to the lamp arrangement: *external*, *distributive* and *immersive* reactors [97].

In the *external* type, the light source is placed outside the reactor. Light has to pass through the reactor wall (which is normally quartz glass for good UV transmission) to reach the water body. The UV intensity in this kind of reactors is normally lower than that in the other two types for the same power consumption. In addition, the UV fluence rate distribution is not even, unless multiple UV lamps are placed around the reactor, which would increase both capital and operation cost. Currently, most of external type water treatment reactors utilize solar radiation so that there would be no capital or operating cost for the light source. As the UV portion in solar radiation spectrum is low, a photocatalyst with low band gap is usually applied to enhance photon efficiency.

In the *distributive* type, the light source is also outside the reactor, like the *external* type. Light transmission media such as glass rods or optical fibers are added inside the reactors to distribute light inside the reactors [98]. The *distributive* type reactor usually has higher and more homogeneous UV radiation inside the reactor than the *external* type reactor. However, the light incident angle has to be chosen carefully in order to avoid total reflection inside the light transmission medium and achieve uniform UV radiation. The maintenance and operation of such reactors are thus complicated.

The *immersive* type reactor has UV lamps placed inside the reactors. This kind of reactors utilizes more UV radiation output than the other two types. Most industrial UV disinfection water reactors are of this type [99]. Various ways of placing lamps inside the reactors have been explored by researchers, such as a row or a matrix of lamps placed perpendicular to the water flow direction [35, 100], or single or multiple lamps placed parallel to the reactor axis [9, 20, 21], via both experiments and simulations. However, each of these studies focuses on only one or two types of lamp arrangement. In this thesis work, different lamp arrangements are compared on a common basis.

Besides the above conventional reactors, there have also been efforts in discovering new reactors which offer higher photocatalytic efficiency. Packed bed reactors have been studied due to their higher surface area for reaction and more efficient mass transfer [82]. The

reactors are filled with UV-transparent packing materials. The photocatalyst is coated on the surface of the packing materials. It has been reported that this type of reactor had higher efficiency than annular reactors with photocatalyst coated on inner wall [69].

Advancement in micro-fluidic devices has been helpful to photocatalytic reactions [101]. The main advantages of micro-fluidic reactors are superior light penetrations, controlled reaction times, precise temperature control and removal of photo-products from the irradiated area, resulting in higher conversions or yields, improved selectivity, enhanced energy efficiencies and reductions of solvent volumes and consequently waste [102].

Application of membrane reactors with photocatalysts has been proposed [103]. The photocatalysts are either immobilized on/in the membrane or suspended in the solution. Immobilized reactors avoid membrane fouling by the photocatalyst and expensive catalyst separation but their efficiency is lower. Destruction of the membrane structure by hydroxyl radicals is another risk for immobilized reactor.

Spinning disk reactors have also been reported to be superior than annular reactors, offering higher quantum efficiency and volumetric reaction rate [83].

Photocatalytic water treatment has been incorporated with other processes to enhance the water recovery or other benefits, such as pervaporation [104] and photo-electricity production [105-107].

2.7.3. Catalyst loading

There have been a large number of papers focusing on different ways of loading catalysts in photocatalytic reactors. These designs could be broadly classified into two categories: slurry and immobilized reactors. Each has its own advantages and disadvantages.

Slurry reactors offer greater surface area for reaction and closer distance from photocatalyst particles to the chemicals and microorganisms. Since $\bullet\text{OH}$ radicals generated are too active to travel long distance in water, photocatalytic degradation and disinfection can be assumed to occur only near the surface of photocatalyst particles. Slurry reactors, therefore, usually exhibit higher efficiency against various target organic pollutants and microorganisms [19, 23, 92, 108-110]. However, the photocatalyst particles have to be filtered and recycled after water treatment. This process is energy intensive due to small size of the catalysts and

thus economically unattractive. This hinders commercial application of slurry reactors. In addition, it is difficult to achieve uniform light intensity distribution for all photocatalyst particles due to light absorption and scattering by the solid particles suspended in the fluid phase, which usually have the size at around the same order as the wavelength of incident UV radiation.

To avoid the filtration process, reactors with photocatalysts immobilized on different supporting materials have been designed. However, the surface area available for photocatalytic reaction is compromised. This together with inadequate mixing lowers the reactor performance. The support materials for photocatalysts varied among different studies. In packed bed and fluidized reactors, photocatalysts could be coated on both porous and non-porous packing materials that are UV-transparent [18, 111-113]. These reactors still faced the problem of non-uniform UV radiation received by photocatalysts, the same as the slurry reactors. Other researchers have studied reactors with photocatalysts coated on the light sources, e.g. jackets for UV lamps or light transmission media immersed inside the reactors [67, 114-117]. There have also been studies on reactors with photocatalysts coated on the inner side of the outer wall. In these reactors, most of the photocatalyst particles experience nearly the same UV radiation intensity.

2.7.4. Target pollutants

Quite a few contaminants have been analyzed for photocatalytic water treatment. Besides real-life wastewater [60, 61], common target pollutants include aromatic compounds such as phenol [118, 119], toluene [76] and chlorobenzene [120] as well as dyes such as Rhodamine B [74], Acid Red 114 [84], Direct Red 16 [121], Ethyl Violet [122], Reactive Brilliant Blue [123] and methylene blue [89, 124-127]. The dyes are of great interest as they are usually hard to be degraded by conventional methods. Their remaining concentration can be easily determined by measuring light absorbance of the reaction suspension or filtered solution. Environmental acidity would affect the electric charge on both the functional groups of dyes and surface of the photocatalysts. Therefore, dyes with different functional groups would have different affinity to the photocatalyst in different pH environment, and hence their degradation kinetics would be affected [128, 129]. During photocatalytic degradation

process, the pH of the mixture is likely to change due to formation of mineral acid, affecting the degradation kinetics.

Some other target pollutants include isovaleraldehyde [130], atrazine [131, 132], Galaxolide [133], 2,4-dichlorophenoxyacetic acid [134], boscalid (a fungicide) [135], Acetamiprid (an insecticide intermediate) [136], styrene-acrylic acid co-polymer [137] and metalaxyl fungicide [110].

2.7.5. Modeling of photocatalytic degradation

Photocatalytic degradation is a complex process, involving more than three phases (water liquid, solid catalyst, light, and sometimes gas bubbled in to facilitate the reaction). The parameters deciding the overall reaction rate includes temperature, solid catalyst particle size, morphology and concentration, target pollutant concentration and its ease of degradation, water flow velocity and pattern, light distribution field inside the reactor, emission power and spectrum of the light source, pH and the catalyst surface properties under that environment, as well as water turbidity. In the literature, only a few of these parameters are studied in each paper while holding all other variables constant. In most cases, the degradation reaction in a well-stirred slurry reactor fits into a Langmuir-Hinshelwood (L-H) model, which is developed from Langmuir isotherm model describing the adsorption equilibrium:

$$-r = \frac{dC}{dt} = \frac{kKC}{1+KC} \quad \text{Equation 2-8}$$

where C is the target pollutant concentration, k is the reaction rate constant and K is the adsorption equilibrium constant [76]. When the concentration of the target pollutant is low, which is normally the case for degradation of dyes (a few dozens of ppm), $KC \ll 1$ and the reaction is pseudo-first-order with respect to the target pollutant concentration.

McMurray et al. used a stirred tank reactor (STR) with TiO_2 immobilized at the bottom of the reactor to study the kinetics of photocatalysis [138]. Formic and oxalic acids were used as target pollutants. It was found out that increasing the stirrer speed did not enhance the reaction rate after a certain extent. Photocatalysis of pollutants was not mass transfer-controlled with sufficiently high Reynolds' number. Catalyst loading enhanced

photocatalysis first and then suppressed disinfection performance after reaching an optimal value. The reaction kinetics was found to follow the L-H kinetics.

Li et al. studied the effects of different parameters on the overall performance of photocatalytic water treatment reactor [18]. TiO₂ deposited on activated carbon was used as the catalyst. The reaction rate results with different initial pollutant concentrations (Rhodamine B in this work) showed that photo-decomposition was first order with respect to target pollutant. Li et al. showed that the apparent rate constant increased with increasing light intensity and decreasing initial organic concentration. The effect of amount of TiO₂ deposited on the apparent rate constant was much more complicated. Li et al. further proposed a kinetic model that incorporated the light intensity into the L-H rate equation.

Saien et al. used a conic body packed bed reactor with TiO₂ coated on transparent Raschig Rings to perform photocatalytic decomposition of Direct Red 16 in water [121]. Both photolysis and photocatalysis occurred. Effects of addition of ethanol to the reaction liquid proved the importance of hydroxyl radicals in photocatalysis, showing that hydroxyl radicals were the major degradation agent in photocatalysis. The experiment showed that, for this reaction, there existed an optimal solution pH. Higher temperature favours photocatalysis, but only to a small extent. Power law could be applied for the photocatalysis kinetics, and the reaction was first order with respect to direct red 16.

Akly et al. synthesized a silica-TiO₂ composite for toluene degradation in air using a sol-gel method [76]. Effects of relative humidity and residence time on toluene removal were analyzed. Further kinetic study revealed that mass transfer, both external and inside pores, had no significant impacts on the reactor. The kinetic data fitted well into the L-H model.

Ballari et al. studied the effects of mass transfer on the photocatalytic degradation of dichloroacetic acid in a slurry flat plate reactor [32]. A specially designed photo-reactor was constructed. UV radiation was introduced through two windows of two opposite sides of the flat plate. The flow in the reactor was kept at laminar regime. The authors showed that, under certain operation conditions, mass transfer limit exists for photocatalysis. Therefore, the validity of perfect mixing model was limited.

Calza et al. studied photo-degradation of HHCB (a synthetic musk fragrance) using Degussa P25 TiO₂ [133]. Different water samples and initial HHCB concentrations were the variants. Both factors were found to be important for degradation efficiency. The dependence of degradation on water quality increases with increasing initial HHCB concentration. Degradation intermediates were examined and possible degradation pathways were proposed.

Chen et al. studied the effects of various operating variables on photocatalytic mineralization of dimethoate by Degussa TiO₂ [34]. Intermediates of mineralization and effects of presence of various organic and inorganic ions were analyzed. The authors suggested competitive adsorption as the reason for decline in photocatalysis activity for inorganic ions at high concentration.

Fernandez et al. modeled photo-degradation of three dyes using factor screening and response surface strategies [139]. It was found by screening method that presence of H₂O₂ was the most significant factor. Even in the absence of photocatalyst, H₂O₂ was able to degrade the dyes. A quadratic empirical equation was established to describe the degradation process by using response surface strategy.

Juang et al. analyzed photo-degradation of two dyes in both single and binary systems [140]. The effects of initial dye concentration, TiO₂ concentration, initial pH and presence of the other dye were analyzed. The reaction rate constants for both dyes were lower in the binary system than in their respective single-dye systems.

Khataee et al. optimized operating conditions such as initial dye concentration, UV fluence rate, and water flow rate and residence time for photo-degradation of Basic Blue 3 over immobilized TiO₂ [141]. RSM and central composite design were utilized.

Sakkas et al. reviewed the application of RSM on the design of experiments for both modeling and optimization in photocatalytic field [142]. Four designs of experiments were described for selection of experimental points, namely, full three level factorial design, central composite design, Doehlert design and Box-Behnken design. Each design is appropriate for a different study. The authors discussed their advantages and disadvantages. In RSM, model equations include polynomial terms of each parameter, as well as products of parameters. The latter one is included if parameters are dependent on one another. An exact

optimization point can be determined when the model equation was obtained. Sakkas et al. then demonstrated usefulness of RSM by a case study of photocatalytic degradation of Congo Red.

Vargas and Nunez studied the kinetics of photocatalytic degradation of three hydrocarbons (p-nitrophenol, naphthalene and dibenzothiophene) in three different reactors (both batch and continuous) by TiO₂ under UV radiation and different acidity environment (pH=3, 6, 10) [143]. The authors reported that experimental results fit the L-H model well. L-H adsorption equilibrium constants, apparent reaction rate constants and pseudo-first-order constants of these three hydrocarbons were calculated. It was shown that the apparent reaction rate constants were highly dependent on the reactor types while adsorption equilibrium constants were independent of reactors. Kinetic study in this work showed that the rate determining step for mineralization was the same as the degradation process. Acidity of the solution affected both the adsorption equilibrium constants and apparent rate constants, and hence it should be optimized for degradation and mineralization.

Zhong et al. studied the mass transfer and reaction mechanism involved in the photocatalytic process in air purification for buildings [144]. The kinetic models of the different conditions of elementary reactions were critically reviewed. The factors that may affect the efficiency were interpreted based on the established fundamental mechanism. Some recommendations were made for future work to improve the efficiency for building applications. The authors then developed and validated a model for UV photocatalytic degradation reactors used in indoor environment [145]. Relationship between degradation performance and various parameters were investigated.

Assadi et al. analyzed effects of operating conditions such as relative humidity, UV radiation, air gap and geometry of reactors on photocatalytic degradation of isovaleraldehyde in air [130]. The authors suggested possible degradation route and fitted the reaction into an L-H model.

Zekri and Colbeau-Justin introduced a new parameter for describing photocatalytic degradation mechanism of phenol and its degradation intermediates by photocatalyst [146]. This parameter is catalyst type-specific and indicates the probability that a photon absorbed by the suspension gives an oxidizing agent. Monte-Carlo simulation was used to calculate the

Local Volumetric Rate of Photon Absorption (LVRPA). The authors claimed their model required minimal input variables and was accurate enough.

Besides modeling based on actual experiment data, CFD simulation has been utilized to assist modeling the photocatalytic degradation process. Li Puma presented dimensionless analysis of steady-state, continuous flow, slurry photocatalytic reactors [19]. Three ideal flow conditions were considered: falling film laminar flow, plug flow and slit flow. The models derived were applicable to flat-plate and annular reactors. Four dimensionless parameters were established and they can be used for reactor scaling-up. Li Puma further showed that falling film laminar flow reactor performs best for slurry reactors.

Alpert et al. studied UV/hydrogen peroxide oxidation of methylene blue utilizing the CFD software PHOENICS [33]. Impacts of different operation and model parameters (such as water flow rate, reaction kinetic rate constants and choice of lamp and turbulence models) on model accuracy were discussed. Grid densities had little effect after reaching a sufficiently fine meshing. Three turbulent models were selected: standard $k-\varepsilon$, renormalized group (RNG) $k-\varepsilon$ and $k-\omega$. Baffle plates were present in the reactor to enhance mixing. All the CFD models under-predicted organic degradation percentage. The error increased with increasing flow rate. Selection of turbulent models did not affect the simulation results much. RAL-LSI (a modified line source integration model) and MSSS (multi-segment source summation) models were used to simulate the UV fluence rate field. MSSS predicted a higher fluence rate. Concentration of dissolved organic carbon (DOC) significantly affects the degradation process as DOC acted as a radical scavenger for $\cdot\text{OH}$. Degradation of methylene blue was found to be overall second order process, with rate constant strongly affecting the simulation.

Queffeuilou et al. used FLUENT to simulate a photocatalytic air purifier to remove acetaldehyde from a room, using kinetic parameters determined from experiment [147]. The selection of parameters and concentration profile were found to be influential on simulation results.

Qi et al. modeled the hydrodynamics and degradation kinetics in an annular photocatalytic bubble column reactor using an Eulerian multi-fluid approach [148]. All the results (gas holdup, fluid flow patterns and organic concentrations) were evaluated against experimental data. The simulation results revealed that the degradation rate of organic

pollutants was controlled by the local hydrodynamics and light intensity. By combining CFD and degradation kinetics models, mechanisms governing the photocatalytic reaction were determined.

Motegh et al. modeled well-mixed photocatalytic reactors [149]. Various criteria were obtained for reactor design regarding inclusion of scattering effects and upper limit of optical thickness. Minimum or maximum optical thickness, for which certain assumptions (such as neglecting scattering effect or ignoring decay of photon absorption) cannot be made, was calculated with different photo fluxes. This can be calculated easily without lengthy simulation of reactors.

2.8. Summary

Photo and photocatalytic water treatment are attractive technologies for conventional disinfection and detoxification technologies. Their computational simulation, modeling and optimization are essential for their industrial application. Some researchers have modeled these processes either by experimental work or computer simulation. Various models have been proposed to describe them. However, there is still much room for research in this area. All the models are limited for certain reactor design or range of operating conditions only. Modeling for the photocatalytic degradation is still in the early stage as the models so far mainly focuses on the process itself and not extended to reactor design. This thesis aims to establish relationship between design and operating parameters and reactor performance for a large variety of reactors via both computer simulation and lab-scale experiments.

Chapter 3

Simulation Methodology

3.1. Introduction

A new simulation methodology was proposed in this research work. Compared to the conventional simulation methodology, this new method offers several advantages. Section 3.2 provides an overview of the proposed simulation method and discusses its advantages over the conventional method. The reactors simulated in this work are described in detail in Section 3.3. Sections 3.4 to 3.6 present the three steps to simulate a photo-disinfection reactor. The results of different simulation methods are compared with the experimental values in Section 3.7. These are followed by a Summary section at the end of this chapter.

3.2. TURF method for simulation of UV disinfection reactor

The proposed procedure for simulating a UV water disinfection reactor comprises of three parts:

1. The UV fluence rate field inside the reactor is established using a Multiple-Point Source Summation (MPSS) model [6] with the aid of MATLAB, a computational software package developed by The MathWorks Inc.
2. Monte-Carlo method is employed to simulate the motion trajectories of a batch of target microorganism particles in the reactor using FLUENT, a CFD software package developed by ANSYS Inc., adopting the Lagrangian approach.
3. By combining the results of the previous two parts, the UV fluence received by each individual microorganism particle is calculated. The distribution of the UV fluence received by the particles and hence the disinfection performance of the reactor is obtained by substituting the UV fluence values received by a large number of microorganism particles, into the UV fluence response equation.

In the previous studies [20, 21], the UV fluence rate field was incorporated as a user-defined function in the CFD software. The output of the CFD simulation was already the reactor disinfection performance. This methodology is named the SURF (Simultaneous UV

fluence **R**ate and **F**luid dynamics) method in this thesis. In the proposed method, the UV fluence rate field and fluid dynamics simulation were conducted separately. Therefore, it took three steps to complete the simulation, called the TURF (**T**hree-step **U**V fluence **R**ate and **F**luid dynamics) method. The TURF method has several advantages over the SURF method:

- It enables separate analysis of the effects of UV fluence rate field and fluid dynamics, i.e. the UV fluence rate field can be changed without changing the fluid velocity profile to see the effects of UV fluence rate field on the reactor performance. This feature is helpful and computationally efficient, especially in multi-lamp systems. One possible application would be analysis of impacts on the reactor performance if one or more of the lamps in the reactor is not working. Also, the fluid velocity profile can be altered while keeping the UV fluence rate field unchanged, e.g. when the water flow rate is changed in the same reactor. This feature can help to analyze the effects of water flow rate on reactor performance.
- The TURF method is computationally faster since less time is consumed for UV fluence rate calculations. For example, Elyasi and Taghipour (2006) calculated UV fluence rate at the centre of each meshed volume. However, in annular reactors, UV fluence rate is constant in the angular direction. Hence, the TURF method calculates UV fluence rate only in the upper half of the x-y plane of the annular reactor, thus reducing the number of UV fluence rate calculations.
- The motion trajectories of particles are stored in separate data files, and they can be later analyzed independently, which is important and convenient for model establishment, as discussed in Section 5.6.

3.3. Reactor specifications

The reactors simulated can be classified into two categories: reactors with single lamp and multiple lamps.

3.3.1. Single lamp reactors

Annular type reactors were first analyzed in this work. These reactors were classified into different shapes (L, linear, reverse-L and U) according to the arrangement of water inlet and outlet, as shown in Figure 3.1. A UV lamp with length equal to that of each reactor was

placed along the axis of the reactor inside a quartz jacket. The radii of the water inlet and outlet were both 1.1 cm. Reactor length, inner radius and outer radius were all varied for analysis of their effects on reactor performance. If the water inlet or outlet is perpendicular to the reactor axis, its centre is located 3 cm away from the nearer end of the reactor. If the water inlet or outlet is parallel to the reactor axis, its centre is located at the centre plane of the reactor, right in the middle between the inner surface of the reactor wall and the outer surface of the quartz jacket. These annular reactor layouts were chosen for their simplicity in meshing and modeling when using the CFD software. Previous studies have shown that arrangement of water inlet and outlet would affect reactor performance [9]. U-shaped reactor is the most widely used one in industrial water treatment.

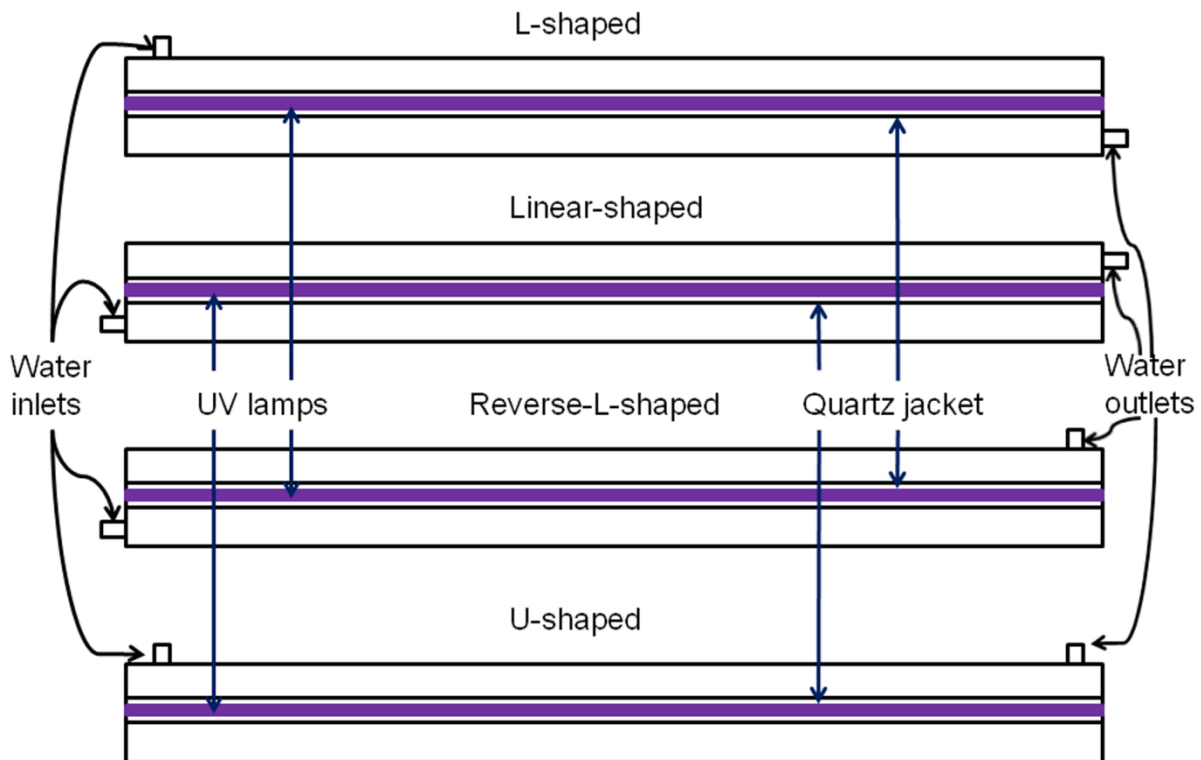


Figure 3.1 Layouts of single-lamp UV photo reactors

3.3.2. Multi-lamp reactors

In order to compare on a common basis, all the reactors with multiple lamps had the same inner dimensions: a cylinder with 50 cm in length and 44.5 mm in radius. Both the water inlet and outlet are perpendicular to the reactor axis, just as the U-shaped reactor in

Figure 3.1. A single-lamp U-shaped annular reactor with the same dimension and the outer radius of the quartz jacket housing the lamp of 1.125 cm was chosen as the reference reactor. In different reactors, the lamps were placed either perpendicular or parallel to the reactor axis. In this thesis work, each reactor was named according to the number and direction (PER for perpendicular and PAR for parallel), as well as orientation with respect to inlet/outlet nozzles (A and B for different reactors with the same number and direction of lamps) of the lamps, as shown in Figure 3.2. For example, 4-PAR-A means type A reactor with 4 lamps placed parallel to the reactor axis.

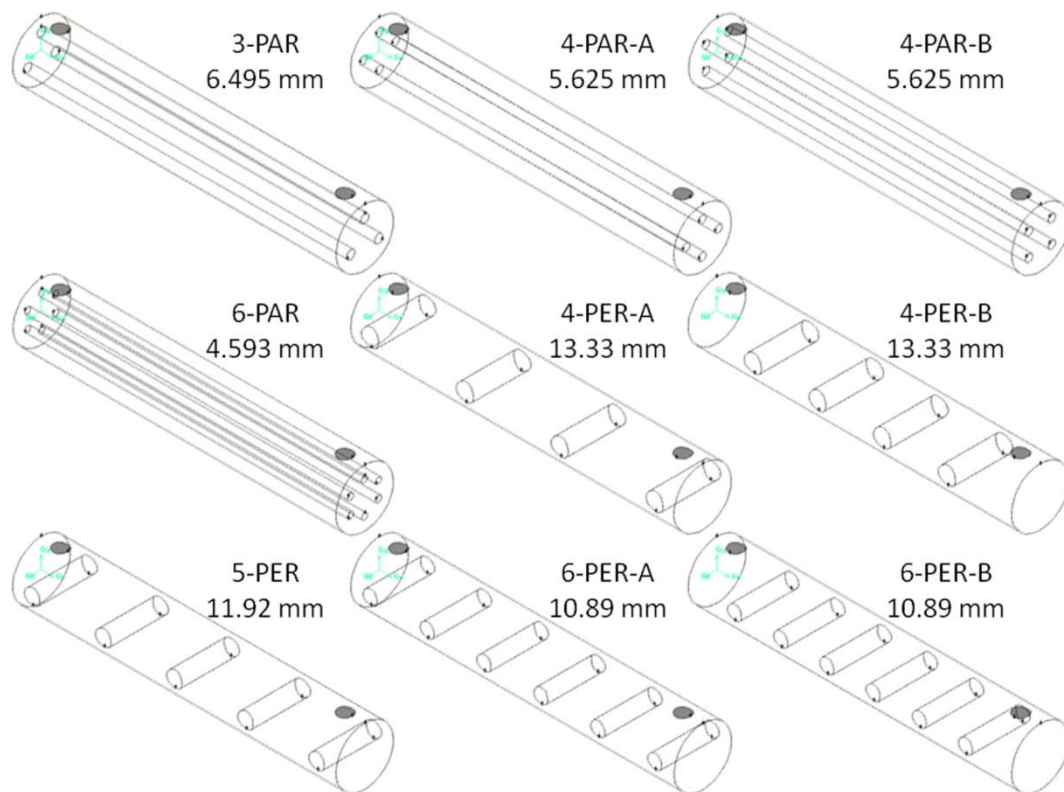


Figure 3.2 Reactor layouts studied in this work; inlet and outlet nozzles are shown as small shaded circles on top of the large cylindrical surface

The major difference between Type A and Type B is that there is at least a lamp directly located below the water inlet and outlet in Type A reactors. In parallel reactors, the centers of the lamps are located right in the middle between center of the reactor and the reactor wall (Figure 3.2). The distance between neighboring lamps is constant for all lamps. In Type A perpendicular reactors, there is one lamp located directly below the water inlet and another directly below the water outlet. The rest of the lamps are distributed evenly between

these two lamps. In Type B perpendicular reactors, the lamps are distributed evenly between two ends of the reactors along its central axis. The internal volumes of all reactors were kept the same as the reference reactor by varying the radius of quartz jackets housing the UV lamps, as indicated by the numbers in Figure 3.2. Both 6-PAR and 5-PER reactors are Type A reactors, with at least one UV lamp located directly below the water inlet. Their respective Type B counter-parts are not analyzed as it was discovered that Type B reactors perform inferior to their Type A counter-parts for those reactors with fewer lamps.

3.4. Establishment of UV fluence rate field

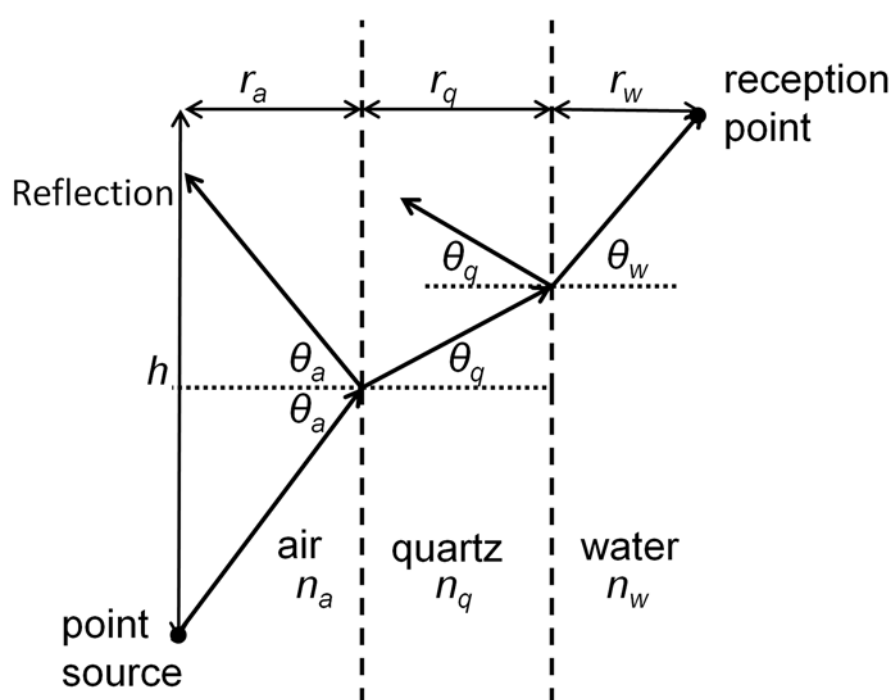


Figure 3.3 Schematic for the MPSS model calculation

The MPSS model was used to simulate the UV fluence rate field inside the reactors. There were three media: air, quartz and water, along the path of each light beam connecting each pair of point source and reception point in a UV disinfection reactor (Figure 3.3). Photonic laws were applied to calculate refraction (Snell's Law) and reflection (Fresnel's Law) at the interfaces as well as absorption (Beer-Lambert's Law) in each medium [25]. MATLAB (version 7.8.0.347, R2009a) was used to calculate the light path length and angle of incidence

in each medium. Thus, the overall fluence rate at any reception point inside the annular reactors was obtained by summing up fluence rate received from all the point sources.

The relationship between the angles of incidence and refraction, and the refractive indices of all the media are described by Equations 2-1 and 2-2. As shown in Figure 3.3, the angles of incidence in air θ_a , quartz θ_q and water θ_w and the refractive indices of air n_a , quartz n_q and water n_w are governed by Equations 3-1 and 3-2:

$$\theta_q = \arcsin[(n_a / n_q) \sin \theta_a] \quad \text{Equation 3-1}$$

$$\begin{aligned} \theta_w &= \arcsin[(n_q / n_w) \sin \theta_q] \\ &= \arcsin\{(n_q / n_w) \sin(\arcsin[(n_a / n_q) \sin \theta_a])\} \\ &= \arcsin[(n_a / n_w) \sin \theta_a] \end{aligned}$$

$$\theta_w = \arcsin[(n_a / n_w) \sin \theta_a] \quad \text{Equation 3-2}$$

For any pair of point source and reception point, their distances in axial direction h and in radial direction in each medium (r_a , r_q and r_w) are all known. Thus:

$$r_a \tan \theta_a + r_q \tan \theta_q + r_w \tan \theta_w = h \quad \text{Equation 3-3}$$

Substituting Equations 3-1 and 3-2 into Equation 3-3:

$$r_a \tan \theta_a + r_q \tan\{\arcsin[(n_a / n_q) \sin \theta_a]\} + r_w \tan\{\arcsin[(n_a / n_w) \sin \theta_a]\} = h \quad \text{Equation 3-4}$$

Equation 3-4 has only one unknown, θ_a . It can be solved by iteration in Matlab. Then, all the angles and length of light path in each medium can be calculated easily. Equations 2-2 and 2-3 were then used to calculate the fraction of light intensity lost along the light path through reflection and absorption. When the length and power of the UV lamp are known, the UV fluence rate received at each reception point inside the reactor can then be calculated by summing all the UV fluence rates received from all point sources. In this project, number of point sources was set at 1000. Doubling this number yielded similar results. The average relative absolute difference between these two UV fluence rate calculations was below 0.2%. For immobilized photocatalytic reactors, an additional layer, photocatalyst, would be applied

between quartz and water. The calculations would be similar, but there would be four terms on the left hand side of Equations 3-3 and 3-4.

3.5. Construction of fluid velocity profile

A CFD software package FLUENT (version 6.3.26) based on finite volume method was used to simulate the fluid dynamics inside the annular reactors. A realizable $k-\varepsilon$ model [8] was selected as the turbulence model. Previous studies [9, 20] have shown that the FLUENT program provides good agreement between simulation and experimental results using the above mentioned model. For each simulation run, the computational domain of the reactor was discretized into 0.5 to 2 million small cells depending on reactor size using the same characteristic length, with the help of a meshing tool: GAMBIT (version 2.4.6), which was also developed by ANSYS Inc. The meshing steps are listed below.

1. Construct the reactor volume according to the specifications.
2. Define each surface including its name and properties.
3. Define zones for all surfaces (inlet, outlet or wall) and volumes (solid or liquid).
4. Create and define boundary layers. Set appropriate values for thickness of first layer, number of layers, and tick the continuity and wedge corner options.
5. Mesh each surface using the “Tri, Pave” algorithm separately. Set appropriate characteristic length (2% of shortest line).
6. Mesh the reactor volume using the “Tet/Hybrid, TGrid” algorithm.

The meshed volume was then loaded into the FLUENT software. The velocity field in the reactor was established by defining the operation parameters and running the simulation according to the following steps.

1. Load the data file describing the meshed volume into FLUENT.
2. Define the viscosity model: the realizable $k-\varepsilon$ model.
3. Tick the discrete phase model option to enable definition of particle specifications.
4. Define the materials. Properties of water and the particles need to be updated.
5. Define the units and operating conditions, especially the direction and magnitude of gravity.

6. Define the injections, i.e. the plane where the particles are released and various properties of particles (water inlet). The discrete random walk model option needs to be ticked.
7. Define the boundary conditions such as water flow rate at water inlet and wall conditions. Define the surfaces such as the one passing through the centers of water inlet and outlet, as well as the central plane. This is mainly to enable analysis after simulation is complete such as Figure 4.2 and 4.3, and is optional.
8. Initialize the computational domain using conditions at the water inlet.
9. Define the particle velocity at the water inlet plane. Set it to the water velocity at the inlet.
10. Run the iteration to start the simulation.

By adopting the Lagrangian approach, i.e. considering the microorganism particles as a discrete phase in water, the data describing the motion trajectory of each microorganism particle passing through the reactor were obtained and exported. The characteristic length used for meshing (2% of the shortest line) was found to be small enough as further reducing the characteristic length yielded small differences (< 2%) in both average UV fluence received by the particles and log reduction of microorganisms. The reactor was assumed to be kept at room temperature throughout simulation. Although UV lamps would heat up the quartz jacket and hence the water flow, such effect was minimal due to low lamp power and high water flow rate. The average maximum temperature rise was calculated to be below 0.04 °C when water flow rate was at minimum in this work, i.e. 250 g/s. This small difference would have practically no impact on fluid dynamics and disinfection. In industrial reactors where lamps of higher power are used, ventilation in the jacket would be required.

3.6. UV fluence distribution and disinfection performance

The data containing the information on the motion trajectories of microorganism particles (i.e., FLUENT output) were imported into the MATLAB program. In conjunction with the UV fluence rate field obtained in Section 3.4, the UV fluence received by each microorganism particle was calculated by numerically integrating the UV fluence rate along its motion trajectory in the reactor using the trapezium rule:

$$U = \sum_{i=1}^{n-1} (t_{i+1} - t_i) \left(\frac{P_{i+1} + P_i}{2} \right) \quad \text{Equation 3-5}$$

where U is the total UV fluence received by the particle, t_i is the time at i th time step, P_i is the UV fluence rate at the particle position at i th time step, and n is the total number of time steps, which was normally between 20000 to 50000. Since the volume of each discretized cell was small, it is reasonable to assume that the UV fluence rate was uniform inside each cell. This assumption is valid as further shrinking the volume of each discretized cell by choosing a smaller meshing characteristic length did not affect the calculated UV fluence received.

The probability of the microorganism surviving the UV radiation inside the reactor was then calculated using the fluence response curve of the target microorganism, which in this work was MS2 virus with a fluence response curve given by Elyasi and Taghipour [9]. MS2 virus is commonly used as the target microorganism in UV disinfection study [150, 151]. Its UV response is an order-3 polynomial relating log-reduction and UV fluence received. According to Elyasi and Taghipour [9], the log-reduction fits the UV response curve when the UV fluence varies from 100 to 1000 J/m². The overall UV fluence distribution and reactor disinfection performance were then established by sampling data for around 5000 microorganism particles. This sample size was large enough as simulation results showed that the average UV fluence received and log reduction of another two sets of sampled data for 5000 microorganism particles was within 0.1% of the first set. Also, further increasing the sample size did not affect simulation results.

3.7. Comparison of simulation methodologies

TURF method was applied to simulate reactors in the literature [9]. The results were compared with the SURF simulation results and experimental log reduction reported by the authors, as shown in Table 3.1. The TURF method has comparable simulation accuracy with SURF method. In SURF simulation, the UV fluence is calculated for each time step of each particle along its motion trajectory. A typical data file containing motion information for 500 particles contains a few millions of time steps. The UV fluence rate calculation is thus repeated a few millions times. However, in TURF simulation, a UV fluence field is constructed beforehand. For reactor with single lamp, the UV fluence rate calculation is repeated for about 5000 times, which is much smaller than in the SURF method. This UV

fluence rate field typically takes about 5 to 10 hours to construct (UV fluence rate calculation for 5000 times) and the fluid dynamic calculation takes about the same time. Therefore, TURF method is able to save most of the calculation time.

Table 3.1 Comparison of simulation results with the experimental values [9]

Reactor	S8Q	S12Q
Experimental log reduction	2.20	2.12
SURF results	2.12	2.26
TURF results	2.31	2.14

3.8. Summary

Photo-disinfection reactors can be simulated using the TURF methodology in three consecutive steps: establishment of UV fluence rate distribution, construction of water flow profile and calculation of microorganism log reduction passing through the reactors. The TURF methodology was accurate enough to describe photo water-disinfection reactors. This method was applied in the next three chapters for simulation of single lamp reactors (Chapter 4), multi-lamp reactors (Chapter 5) and validation of models (Chapter 6).

Chapter 4

CFD Simulation of Photo Water-Disinfection Reactors

4.1. Introduction

CFD simulation of photo water-disinfection reactors was conducted. The effects of different parameters, including reactor shape and size, water flow rate, average UV fluence (i.e. lamp power), the size and shape of the microorganism particles on the overall performance of the reactor were analyzed. Since these parameters affect the average UV fluence rate inside the reactors, the performance of different reactors was assessed by comparing their disinfection log reduction ($-\ln(N/N_0)$), where N_0 is the number of microorganism particles passing through the reactor and N is the number of the microorganism particles surviving the UV radiation inside the reactor at the outlet, under the same UV dosage. UV dosage was calculated by dividing the total UV lamp power by water flow rate. Keeping UV dosage across different reactors constant under different operating conditions was achieved by varying the UV lamp power accordingly. This comparison was reasonable since majority of the operating cost of UV disinfection reactors comes from electricity power consumption of the lamps. Therefore, a better UV disinfection reactor can be defined as a reactor which can kill more microorganisms with the same power input.

The UV fluence rate field calculated by MATLAB is discussed in Section 4.2. The water flow velocity profile constructed by CFD simulation in FLUENT is presented in Section 4.3. The UV fluence received by the particles is shown in Section 4.4. The effects of particle size and shape are discussed in Section 4.5. The overall reactor performance and the effects of various design and operating variables are presented and discussed in Sections 4.6 to Section 4.8. The relationship between reactor performance and particle motion trajectories inside the annular reactors is examined in Section 4.8. Findings of this work are summarized in the last section of this chapter.

4.2. UV fluence rate field

MATLAB was used to construct the UV fluence rate (P_R) field. Refraction, reflection and absorption of UV radiation were calculated using the method described in Section 3.4.

Figure 4.1 shows the UV fluence rate at different positions inside an annular reactor with the following specifications: 4.45 cm outer radius, 1.125 cm inner radius, 94 cm length and 39 W lamp power. It can be observed in Figure 4.1a that P_R is almost constant along the axial direction (x) for majority of the axial length; but it decreases drastically along the radial direction (r), as shown in Figure 4.1b. Disinfection is therefore much faster at regions close to the UV lamp. Hence, the radial mixing is more important to narrow the distribution of UV fluence received by microorganism particles (U_p) for better disinfection performance.

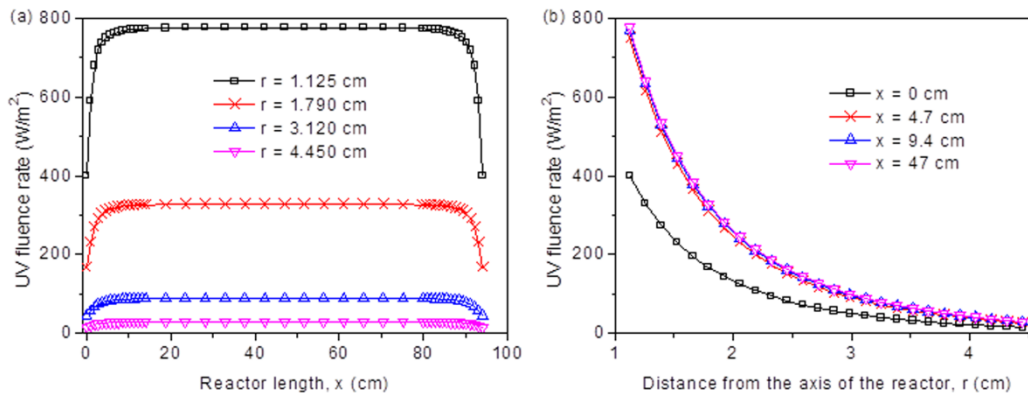


Figure 4.1 UV fluence rate distribution in a reactor: (a) along axial direction at different radii, and (b) along radial direction at different axial positions

The volumetric average (\bar{P}_R) and normalized standard deviation (S_{PR}) of UV fluence rate in a reactor are important for reactor performance. As UV fluence rate distribution inside the reactors was assumed to be independent of water flow field, different arrangements of water inlet and outlet as well as different water flow rates would not affect both \bar{P}_R and S_{PR} , which were only dependent on reactor dimensions and lamp power. Calculated values of \bar{P}_R and S_{PR} for reactors of different lengths, inner and outer radii are presented in Table 4.1. As shown in this table, \bar{P}_R was almost inversely proportional to reactor length. Also, S_{PR} was found to be insensitive to reactor length. Decreasing outer radii of reactors shrank the regions of lower P_R , and hence increasing \bar{P}_R and decreasing S_{PR} at the same time. Increasing the reactor inner radius had more complicated effects. On one hand, it reduced regions of higher P_R . On the other hand, it reduced length of light path in water and increased that length in air. Since UV absorption coefficient of water is much higher, overall effect of increased inner radius is slightly increased \bar{P}_R . According to UV fluence rate calculation, increasing inner

radii from 9 to 15 mm increased \bar{P}_R when the outer radius was 44.5 mm (Table 4.1). As thinner reactors offered narrower P_R range, increasing reactor inner radii reduced S_{PR} .

Table 4.1 Average UV fluence rate (\bar{P}_R) and its normalized standard deviation (S_{PR}) of different single-lamp reactors

Reactor length (cm)	Inner Radius (mm)	Outer Radius (mm)	\bar{P}_R (W/m ²)	S_{PR}
50	11.25	44.5	224.79	1.0595
70	11.25	44.5	163.18	1.0526
94	11.25	44.5	122.77	1.0481
120	11.25	44.5	96.8	1.0453
94	11.25	35	180.3	0.778
94	11.25	40	146.22	0.9204
94	11.25	50	100.68	1.2042
94	9	44.5	120.95	1.1974
94	13	44.5	124.03	0.9516
94	15	44.5	125.45	0.8556

Although larger reactors had lower \bar{P}_R and higher S_{PR} , which are both detrimental to reactor performance, the overall effect of reactor size on disinfection is more complicated. Larger reactors offer higher residence time, and hence increase the UV fluence received by the particles, which enhances microorganism log reduction.

4.3. Flow velocity field

The flow velocity field is highly dependent on reactor layout. Figure 4.2 shows the distribution of turbulence intensity in reactors of different shape with the same dimensions (94 cm length, 11.25 mm inner radius, 44.5 mm outer radius). The flow rates are all 757 g/s.

High turbulence is observed at the water inlet for all reactors. The L-shaped reactor has the highest average turbulence intensity and the reverse-L shaped reactor has the lowest (Figure 4.2). The U-shaped reactor has the most uniform turbulence intensity (Figure 4.3). Normally, higher turbulence means better mixing and hence better reactor performance. Therefore, one may deduce that L-shaped reactor has the highest log reduction among the four under these operating conditions.

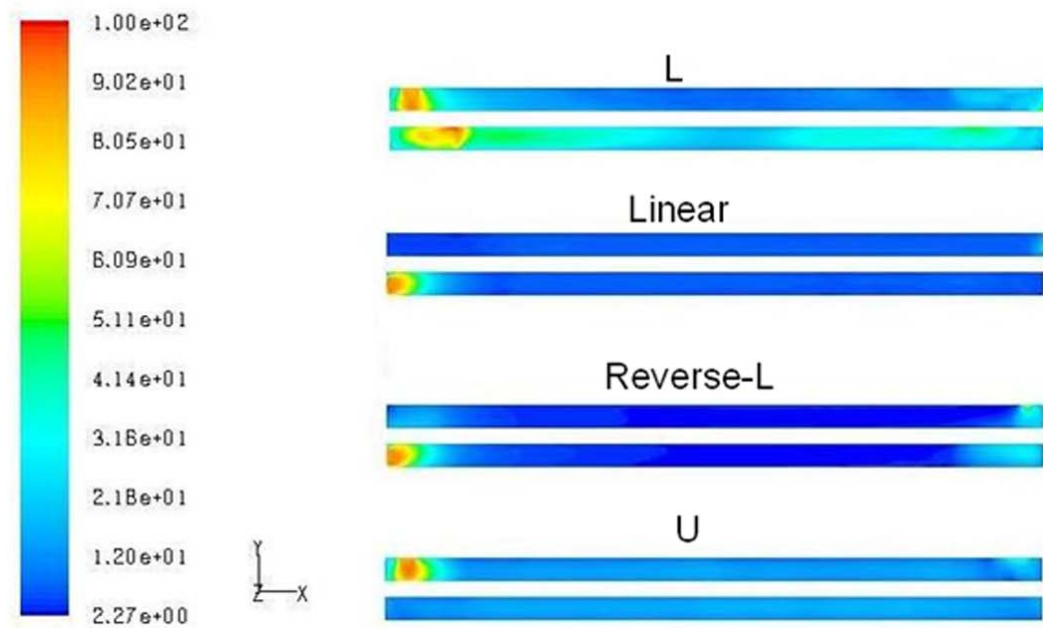


Figure 4.2 Turbulence intensity distribution in different reactors

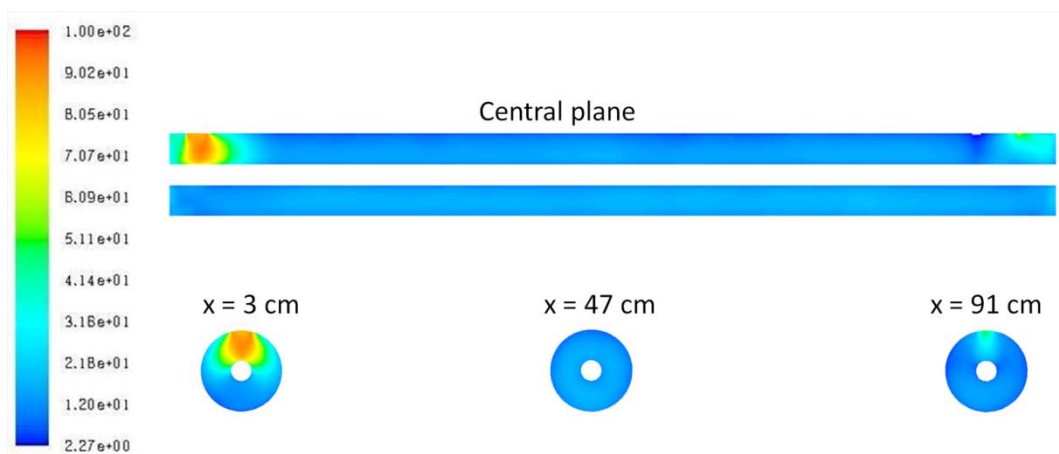


Figure 4.3 Turbulence intensity distribution in a U-shaped reactor

Figure 4.3 shows the turbulence intensity distribution in the above U-shaped reactor when the water flow rate is 757 g/s. The annular graphs under the central plane show the turbulence intensity at different reactor lengths, namely, at the centre of the water inlet ($x = 3$ cm), at the half length of the reactor ($x = 47$ cm) and at the centre of the water outlet ($x = 91$ cm). It can be observed that the water flow is highly turbulent at the water inlet, especially at the upper half of the reactor. The turbulence intensity at the water outlet is much lower than that at the water inlet. At the centre of the reactor, the turbulence intensity is almost uniform.

4.4. UV fluence received by particles

Average UV fluence received by microorganism particles (\bar{U}_p) inside a reactor is an important factor as higher UV fluence received means better disinfection performance. Figure 4.4 shows the relationship between the water flow rate, the mean residence time of microorganism particles and that of water for the linear-shaped reactor of 94 cm length, 11.25 mm inner radius and 44.5 mm outer radius. The nearly identical lines indicate that microorganism particles had similar mean residence time to that of water molecules.

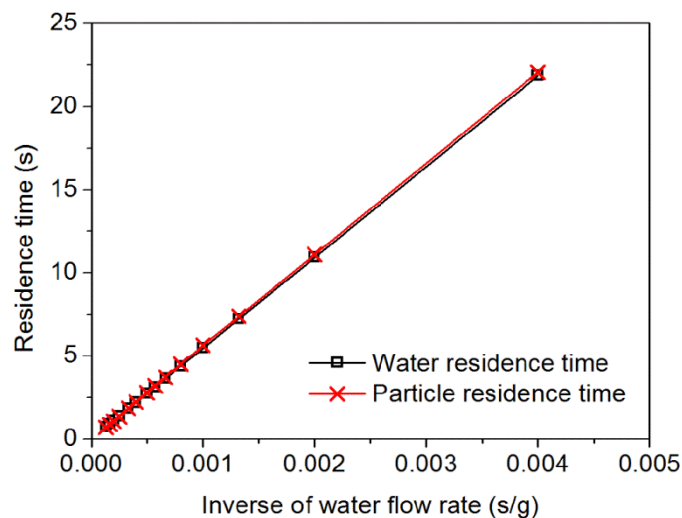


Figure 4.4 Residence time of water and microorganisms under different water flow rates

In Figure 4.5, the data points are average UV fluence received by microorganism particles (\bar{U}_p) under different water flow rates and constant UV lamp power. Figure 4.5 shows that with reactor dimensions specified above and water flow rates varying from 250 g/s to 7500 g/s, the mean UV fluence received by microorganism particles was close to the product of the mean residence time of the microorganism particles (which was close to that of

water as shown in Figure 4.4) and the volume-weighted average UV fluence rate (\bar{P}_R , 135 W/m² in this case) inside the reactor, i.e.:

$$\bar{U}_p \approx \bar{P}_R \times \bar{t}_w = \bar{P}_R \times V_R / Q \quad \text{Equation 4-1}$$

where V_R is the reactor volume and Q is the volumetric water flow rate. The latter two values could be calculated without knowledge of fluid dynamics inside the reactor. Similar relationship was also observed for all other reactors.

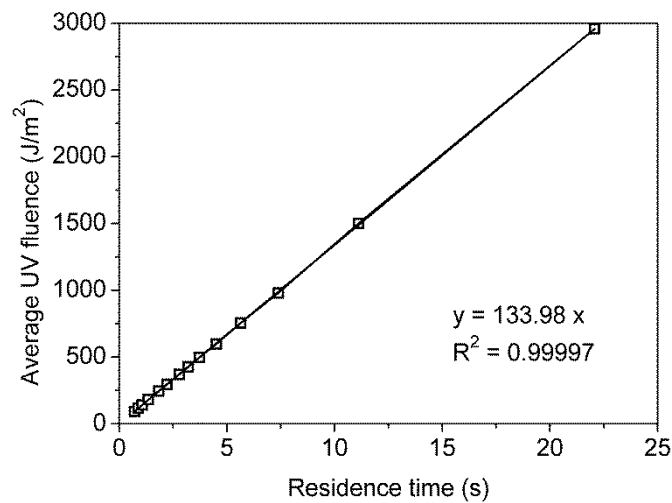


Figure 4.5 Average UV fluence against residence time under constant UV lamp power and different water flow rates

4.5. Particle size and shape

Microorganisms vary in size and shape greatly. The motion trajectories of particles of different diameters and shape factors passing through a U-shaped reactor with the water flow rate at 757 g/s and UV lamp power at 39 W were simulated. Combined with the UV fluence rate field established in Section 4.4, distribution of UV fluence received by these particles was obtained. From the results shown in Figure 4.6, it could be concluded that increasing diameter of spherical particles, d_p , from 0.5 to 10 μm (typical length of bacteria ranges from 0.5 to 10 μm , and viruses are even smaller) would not significantly change the distribution of UV fluence received by particles. The shape of the microorganism particles also had minimal effect. The distribution of the UV fluence received by the particles with shape factor (SF) ranging from 0.1 to 1 and 1 μm in equivalent diameter (equals to the diameter of a sphere with the same volume as the particle) is similar to one another. Shape factor in this work was

defined as the ratio of the surface area of a sphere with the same volume as the particle to the actual surface area of the particle, which always has a value between 0 and 1 and is important in calculating the drag force experienced by the particles in the reactors.

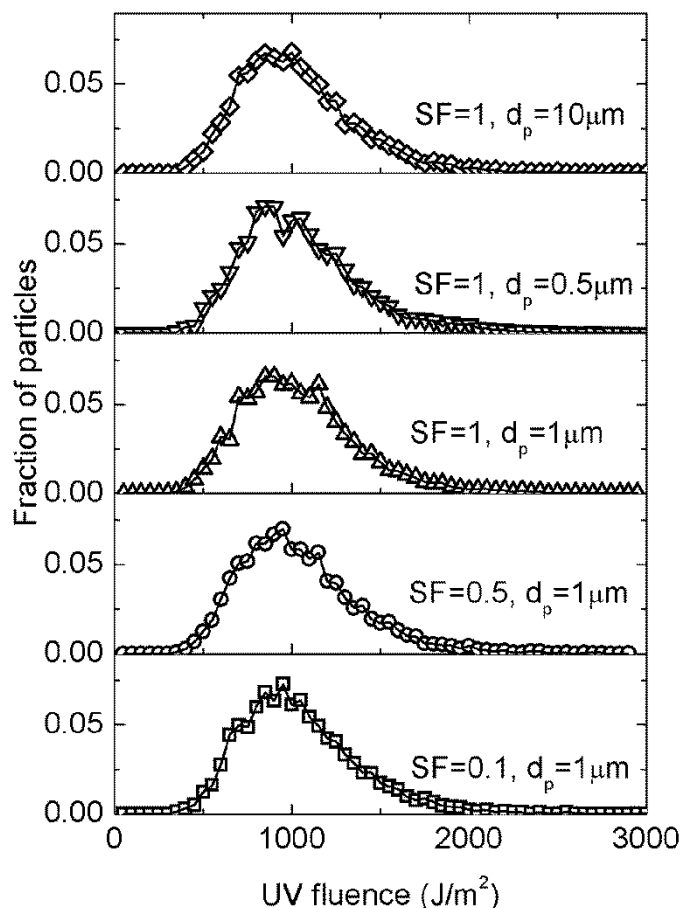


Figure 4.6 Distribution of UV fluence received by particles with different diameters, d_p , and shape factors (SF) in a U-shaped disinfection reactor

The fluctuations in the distribution curves in Figure 4.6 were due to random sampling errors. Due to the similar UV fluence distribution shown above, the overall log reduction of microorganism particles would also be close if their UV response was the same. This is due to the fact that, for small objects like bacteria and viruses, their sizes and shapes do not interfere with the fluid dynamics inside these reactors. Hence, microorganisms with similar UV fluence response but different sizes and shapes would have similar deactivation in the same UV disinfection reactor operated under the same conditions.

4.6. Reactor efficiency and water flow rate

By adopting the simulation methodology described in Chapter 3 and substituting the UV response of MS2 virus provided by Elyasi and Taghipour (2006), the average reduction was close to the reported experimental values (less than 5% in absolute relative difference, Table 3.1).

Different reactors under different operating conditions may have similar \bar{U}_p . For example, if the lamp power and water flow rate of a reactor are both doubled, the new average UV fluence received by particles should be similar to the original value (as $\bar{U}_p \approx \bar{P}_R \times \bar{t}_w$). The difference in reactor disinfection performance should mainly arise from different distributions of U_p . Therefore, normalized standard deviation of UV fluence (S_U), defined as standard deviation of UV fluence received by particles (σ_U) divided by the average particle UV fluence (\bar{U}_p) was calculated and its relationship with reactor performance was analyzed.

Higher S_U can be due to a lower peak in the UV fluence distribution plot or a peak at lower UV fluence value, i.e. a longer tail. Since the reactor performance is also sensitive to average UV fluence due to non-linearity of the UV response curve, the reactor efficiency is compared while holding average UV fluence received by particles constant. For this, reactor efficiency, η , is defined as:

$$\eta = [\ln (N / N_0)] / [\ln (N / N_0)]_{ideal} \quad \text{Equation 4-2}$$

where the numerator is the log reduction of the UV disinfection reactor under consideration and the denominator is the log reduction which would occur in an ideal reactor, i.e. all microorganism particles received the average UV fluence (so $S_U = 0$).

In the above simulations, the power of the UV lamp was kept constant. The mean UV fluence received by the microorganism particles decreased with increasing water flow rate. The change in the reactor efficiency was due to changes in both UV fluence rates and water flow rates. To further analyze the effects of the water flow rate only, more simulations were performed. The average UV fluence received by the microorganism particles was held constant while varying the water flow rate for each of these simulations. This was achieved

by varying the power of the UV lamp, i.e. the power of the UV lamp was set to higher values for simulations of higher water flow rates. Figure 4.7 shows the dependence of the efficiency of the linearly shaped reactor with above specification on the water flow rate under different average UV fluence values. It could be deduced that the UV disinfection efficiency was at maximum when the water flow rate was about 1750 g/s, regardless of the change in the average UV fluence. All the efficiency curves under different average UV fluence values were similar in shape and reach maximum at around the same water flow rate, suggesting that this optimal water flow rate where such maximum efficiency occurred was dependent on reactor specification but independent of average UV fluence, or in other words, lamp power. In order to study the dependency of optimal water flow rate on the UV fluence response of the microorganism, the coefficients in the fluence response equation were varied. The optimal water flow rate is still at 1750 g/s.

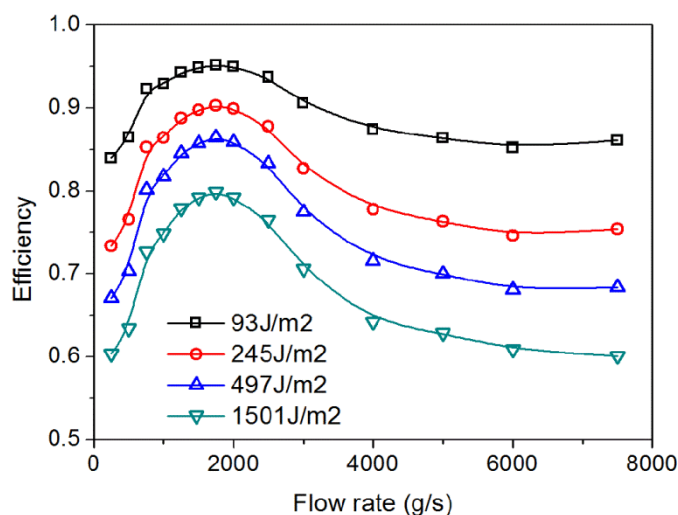


Figure 4.7 Efficiency of the reactor under different water flow rates with constant average UV fluence

The increase in the efficiency in the linear-shaped reactor when water flow rate is lower than 1750 g/s is due to the increase in turbulence and mixing induced by the increase in water flow rate. Since the UV fluence rate decreases rapidly in the radial direction, disinfection is much faster at regions close to the UV lamp. The radial mixing is therefore more important to achieve high reactor efficiency. However, further increasing the water flow rate beyond 1750 g/s may suppress the radial mixing. Under high water flow rate, some particles would stay in regions of low UV fluence rate near the reactor wall while some others stayed in regions of high UV fluence rate near the lamp throughout the disinfection

process. This widened the distribution of UV fluence received by microorganism particles and hence decreased the reactor efficiency.

The fluence response curve used in this work was a polynomial expression relating UV fluence and log reduction of microorganisms. Therefore, from mathematical point of view, the relationship between log reduction and average UV fluence was closer to a linear curve and thus at lower average UV fluence, a higher efficiency was expected. Figure 4.7 also shows that the efficiency of reactors decreased with increasing average UV fluence received by microorganism particles while holding the water flow rate constant.

4.7. Dimensionless analysis

Figure 4.8 shows that the relationship between reactor efficiency, η , and normalized standard deviation of UV fluence, S_U , is very close to a second order polynomial. Note that the y-intercept in this figure is 1. The data points in Figure 4.8 are for 10 annular reactors of different dimensions and layouts under different water flow rates, and average UV fluence is 116 J/m^2 .

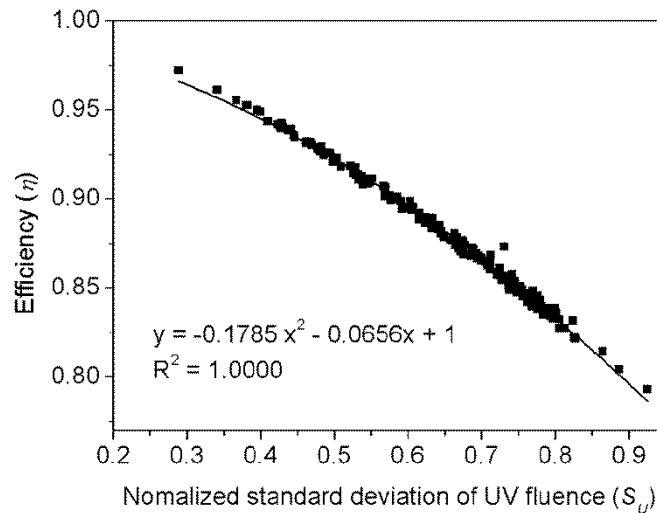


Figure 4.8 Relationship between single-lamp reactor efficiency, η , and normalized standard deviation of UV fluence, S_U , at average UV fluence = 116 J/m^2

Throughout the positive range of S_U , η decreases with increasing S_U . This trend is expected. When all the particles experience the same amount of UV radiation (i.e., S_U is 0), efficiency of the reactor is maximum (i.e., $\eta = 1$). Larger S_U means broader distribution of U_p and hence lower efficiency. Since the points representing S_U and η were approximately on the

same curve, it is reasonable to propose that distribution of UV fluence received by microorganism particles in different annular reactors under different operating conditions were similar in shape.

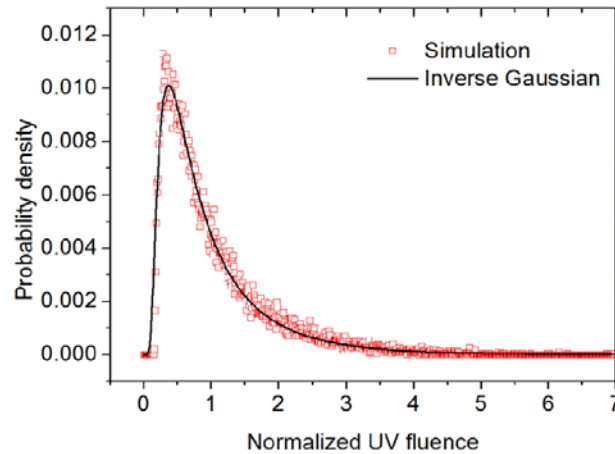


Figure 4.9 Comparison of probability density of normalized UV fluence calculated from inverse Gaussian distribution and simulation results

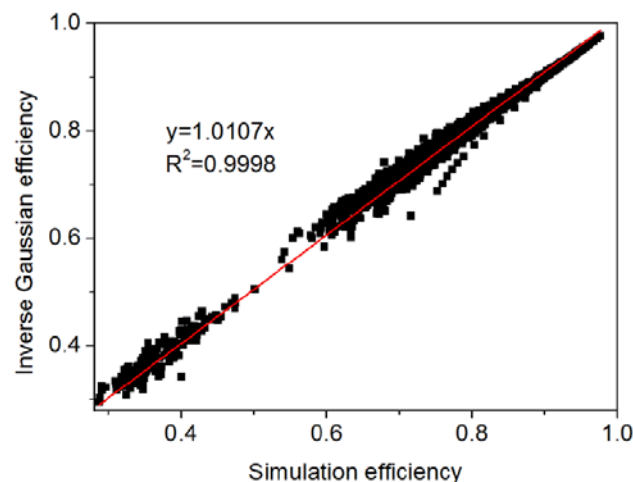


Figure 4.10 Comparison of reactor efficiency calculated from inverse Gaussian distribution and simulation results

After analyzing the results shown in Figures 4.6 and 4.8, all UV fluence normalized by \bar{U}_p were found to be close to the inverse Gaussian distribution with the same mean (1.0) but different variances. Figure 4.9 shows the comparison of inverse Gaussian distribution and simulation results. The efficiency calculated from the inverse Gaussian distribution was also found to be close to the simulated results, with average absolute relative error of around 1.5% over more than 2500 data points, as shown in Figure 4.10. However, the inverse Gaussian

distribution approximation was applicable to single-lamp reactors only. The UV fluence rate distribution and water flow profile was expected to be significantly different in multi-lamp reactors. Consequently, the UV fluence received by microorganisms distributed differently and hence the reactor performance was also different.

4.8. Reactor shape and size

Reactor shape and water flow rate (Q) can affect the disinfection performance due to their different flow patterns. Even though \bar{U}_p of different reactors under different operating conditions would be close to one another, different distribution patterns of U_p result in different reactor efficiencies. Figure 4.11 shows the distinct behaviour of log reduction when Q is varied for single-lamp reactors of the same dimension (94 cm length, 11.25 mm inner radius, 44.5 mm outer radius) but different water inlet and outlet arrangements under the same UV dosage (15 J/kg). Velocity of water in the annulus region varies from 4.29 cm/s to 129 cm/s for the Q range in this figure. Linear-shaped reactor exhibited a nearly parabolic relationship between Q and log reduction. Maximum log reduction occurred at around 1750 g/s. Reverse-L-shaped reactor had a nearly constant log reduction with small fluctuations when Q was varied from 250 to 7500 g/s. Both U-shaped and L-shaped reactors showed a dip in log reduction when Q was around 1250 g/s, and L-shaped reactor performed better than U-shaped reactor under most conditions. The large fluctuations are due to random errors in Monte Carlo simulations and complex nature of turbulence.

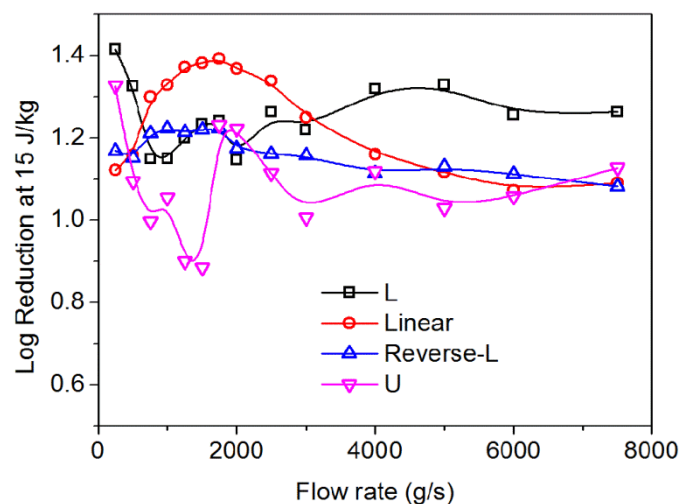


Figure 4.11 Log reduction of different single-lamp reactors with dosage at 15 J/kg

U-shaped and L-shaped reactors exhibited more fluctuations because of arrangement of water inlet. Unlike linear- and reverse-L-shaped reactors with water inlets parallel to reactor axis, U- and L-shaped reactors have water inlet perpendicular to the reactor axis (Figure 3.1). Water flow is deflected by the quartz jacket in these two reactors. This made the relationship between water flow rate and profile more complicated, resulting in more fluctuation in log reduction. Combined with Figure 4.2, it can be observed that, although the L-shaped reactor has higher average turbulence intensity than the U-shaped reactor when the water flow rate is 757 g/s, the U-shaped reactor performs better. Therefore, the average turbulence intensity is not directly related to the overall reactor performance. The deflection effect mentioned above shows that the movement of microorganism in radial direction is a candidate for indicator of reactor performance.

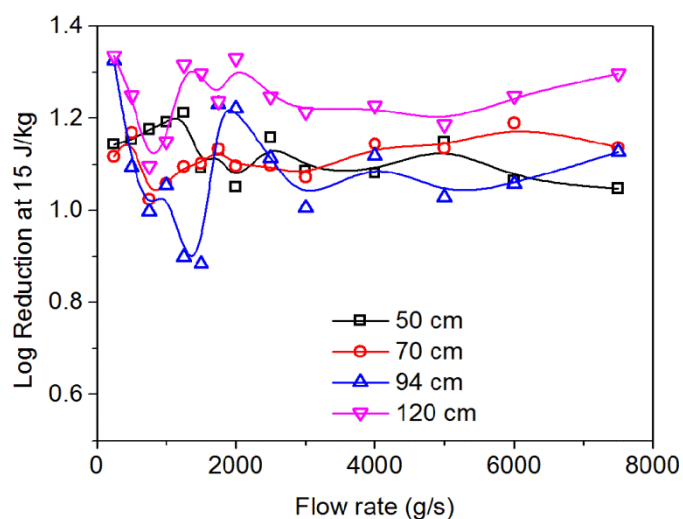


Figure 4.12 Reactor performance of reactors with different lengths

Longer reactors are expected to perform better due to better mixing in radial direction enabled by longer residence time. To verify this, U-shaped reactors of different lengths (50 cm, 70 cm, 94 cm and 120 cm) were analyzed under different water flow rates. All the reactors studied for this have the same inner and outer radii (11.25 mm and 44.5 mm respectively). The 120 cm reactor had the highest overall log reduction under most water flow rates. However, reactor performance does not improve for all reactor lengths and water flow rates, as shown in Figure 4.12. The 50 cm, 70 cm and 94 cm reactors have similar performance and large fluctuation for most of the lower water flow rate. At higher water flow

rate, the log reduction exhibits less fluctuation, as the difference in radial mixing is suppressed by the high water velocity in axial direction.

Reactors with smaller cross-sectional areas have smaller variance in UV fluence rate field inside the reactors, as discussed in Section 4.2. Therefore, distribution of U_p should also be narrower and hence the reactor performance should be better. However, changing cross-sectional areas of reactors also affects fluid dynamics. In addition, smaller cross-sectional area reduces reactor volume if the reactor length is kept constant, thus reducing the particle residence time and UV fluence received by the particles if the UV dosage is kept constant. This is complicated further by change in $\overline{P_R}$. Thus, the overall effect is hard to predict. Four reactors with 94 cm length and 11.25 mm inner radius but different outer radii (35 mm, 40 mm, 44.5 mm and 50 mm) were simulated under different water flow rates. 50 mm reactor had the highest log reduction while 35 mm one had the lowest under most water flow rates (Figure 4.13). This is due to their difference in reactor volume and thus residence time and average UV fluence received by particles. Larger reactors offer higher residence time, which allows more time and thus UV fluence received for disinfection.

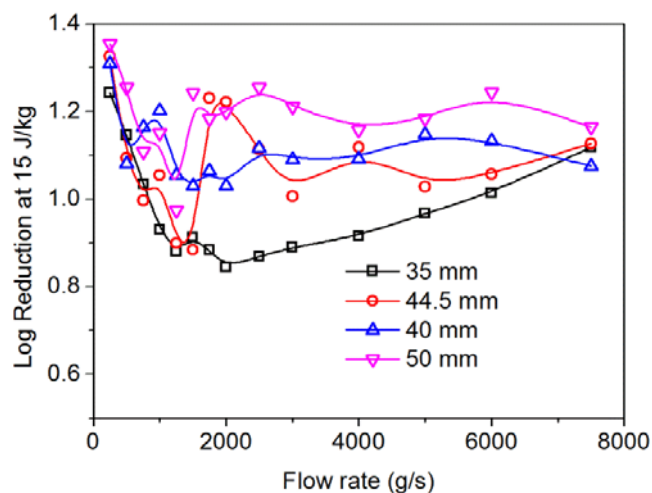


Figure 4.13 Performance of reactors with different outer radii

This situation is similar to the case where the inner radius is varied. To confirm this, another four reactors with the same length (94 cm) and 44.5 mm outer radius were simulated under different water flow rates (Figure 4.14); their inner radii were 9 mm, 11.25 mm, 13 mm and 15 mm. Under most water flow rates, the 9 mm reactor had the highest overall log

reduction and the 15 mm had the lowest. Therefore, larger cross-sectional area favours better reactor performance.

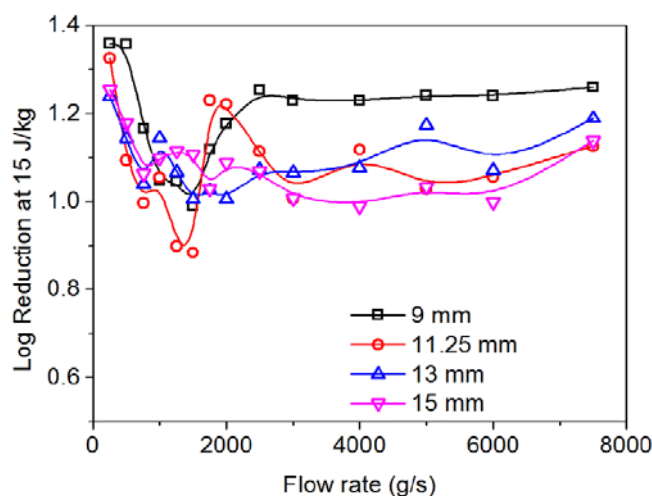


Figure 4.14 Performance of reactors with different inner radii

4.9. Radial displacement

Turbulence inside the reactor is a good indicator of mixing. However, it is not sufficient for reactor performance since the distribution of UV fluence rate (P_R) inside the reactor is also important. Even when the dimensions of reactors and lamp power are the same (i.e., distribution of P_R is the same), higher turbulence does not lead to higher disinfection. As discussed in Section 3.1, P_R decreased rapidly along radial direction and remained almost constant along axial direction in single-lamp reactors. Therefore, it is reasonable to propose that a batch of particles, which had a higher displacement in radial direction (defined as r-displacement, D_r) when passing through a reactor, should have a narrower distribution of U_p (i.e. smaller S_U) than a batch of particles with a smaller D_r passing through another reactor with the same dimensions. This is because, in the latter batch, some particles would stay in regions of low P_R near the reactor wall while some others stayed in regions of high P_R near the lamp throughout the disinfection process. This widens the distribution of U_p . If both batches of particles have the same \bar{U}_p , the latter one should have a lower log reduction. This expected effect of r-displacement is investigated through simulation, and discussed below.

The r-displacement was calculated by accumulating the differences between consecutive time steps in the radial distance of the particle from the central axis of the reactor.

This value would be affected by the characteristic length of meshing. However, comparison across different water flow rates (Q) in the same reactor is still valid since the meshing structure was identical for the same reactor. Figure 4.15 shows the relationship among Q , log reduction and r-displacement for a linear-shaped reactor under the same dosage. It can be observed that both log reduction and r-displacement vary similarly with Q and also have peak values at approximately the same Q . The increase in the log reduction at lower Q could be primarily due to the increase in turbulence and mixing induced by the increase in water flow rate. However, further increasing the water flow rate beyond 1750 g/s may suppress the radial mixing as the reduction in residence time did not allow large D_r . This widened the distribution of UV fluence received by microorganism particles and hence decreased log reduction. Therefore, it is reasonable to conclude that reactor performance and r-displacement are correlated to each other for linear-shaped reactors.

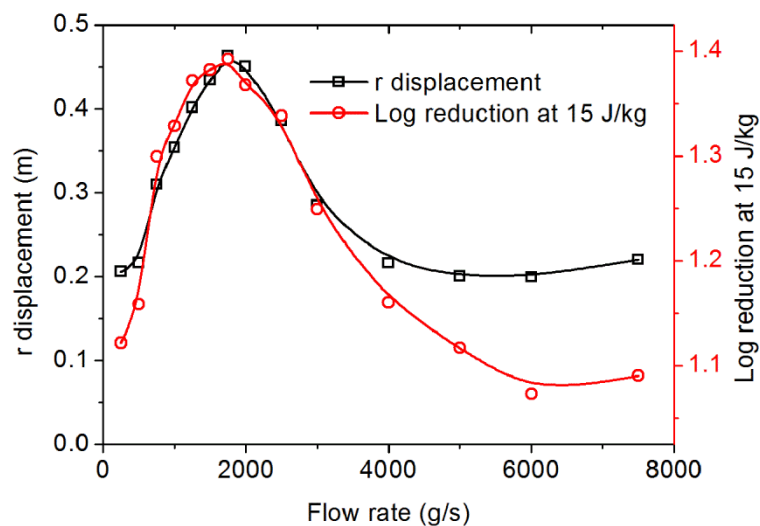


Figure 4.15 Linear-shaped reactor log reduction and r-displacement, dosage = 15 J/kg

However, the correlation in Figure 4.15 between reactor performance and r-displacement was not observed for reactors of other shapes studied. This is because the range of r-displacement of reactors of other shapes under different Q was not large enough to observe such trend. All the reactors except for the linear-shaped reactor in this work had water inlet or outlet (or both for the U-shaped reactors) that was perpendicular to the reactor axis. Therefore, r-displacement in such reactors was bigger than that in the linear-shaped reactor, reducing the relative range of r-displacement. Figure 4.16 shows the log reduction and r-displacement of a U-shaped reactor of the same size as that in Figure 4.15. The

variation in r-displacement is smaller in Figure 4.16 while its absolute value is larger. In addition, r-displacement is dependent on reactor dimensions. Longer reactors with larger cross-sectional area are expected to have larger r-displacement. In this case, distribution of r-displacement is more important. Smaller normalized standard deviation of r-displacement (S_{rd}) means more even distribution of r-displacement among particles, and hence narrower distribution of U_p and consequently higher log reduction. Since S_{rd} is normalized by average r-displacement, it also provides a reasonable way to compare reactors of different dimensions. In addition, reactors with different sizes and UV lamps usually offer different S_{PR} , which should also be considered. Figure 4.17 shows the variation of log reduction in U-shaped reactors with different lengths (a), outer radii (b) and inner radii (c) and S_{rd} , all with the same dosage. The general trend of higher S_{rd} resulting in lower log reduction still holds.

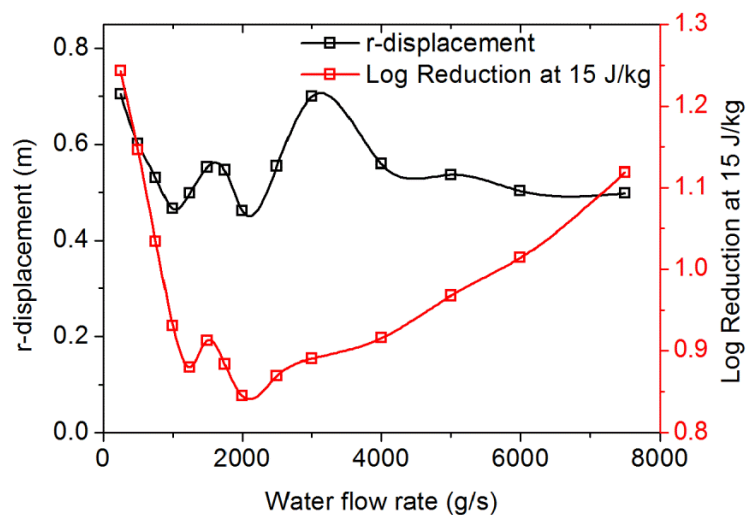
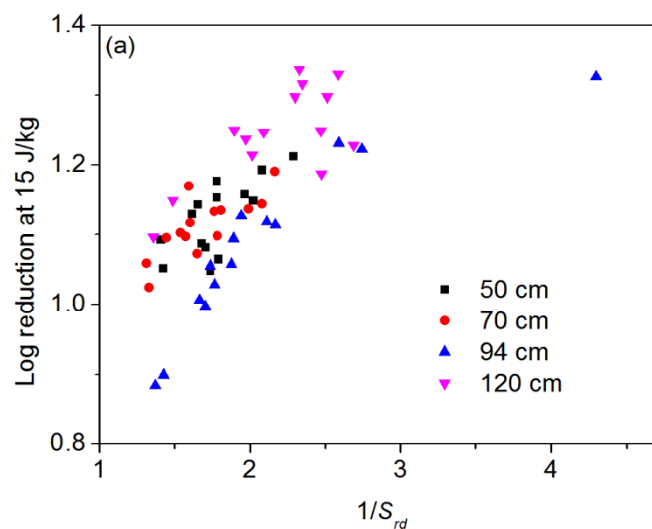


Figure 4.16 U-shaped reactor log reduction and r-displacement, dosage = 15 J/kg



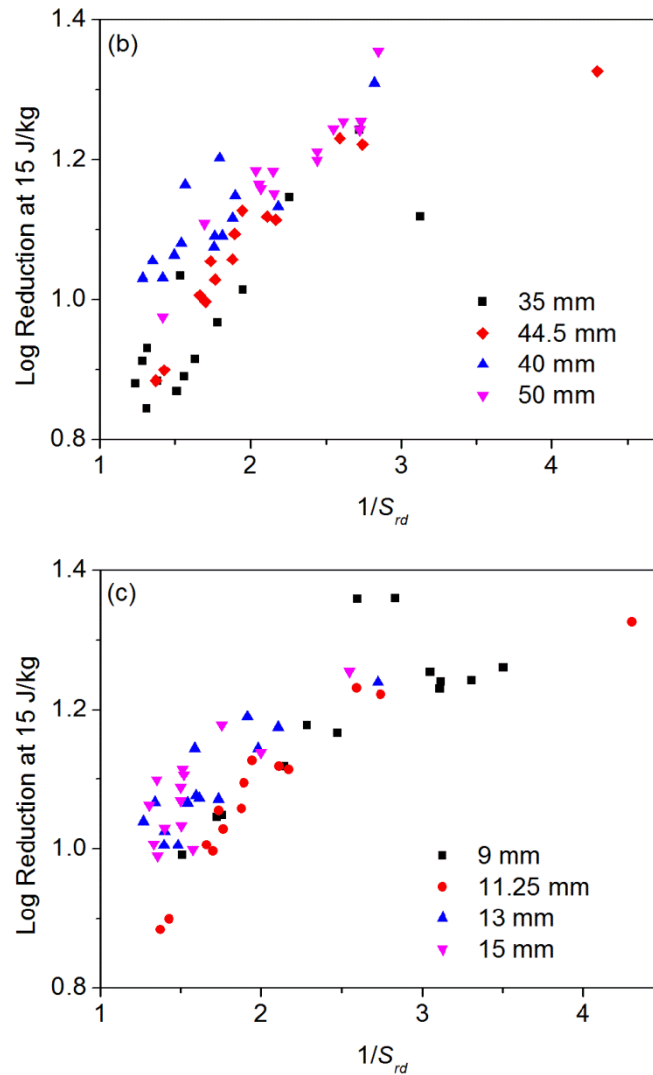


Figure 4.17 Variation of log reduction with S_{rd} in U-shaped reactors of different lengths (a), outer radii (b) and inner radii (c) and S_{rd} , with dosage = 15 J/kg

4.10. Conclusions

The effects of various operating and design variables on the performance of various UV water disinfection reactors were analyzed using a new TURF method. The size and shape of microorganism particles did not have a large impact on the UV fluence received by microorganisms. Water flow rate, reactor size and shape have complex effect on reactor performance. It was found that reactor performance was correlated to the particle movement in radial direction inside the reactors. Overall, this work provides the simpler TURF method for simulation of UV disinfection reactors, many results and better understanding of the effect of design and operation variables on the performance of UV disinfection reactors. An efficient UV disinfection reactor should enhance radial movement of particles inside the

reactor, either by increasing the radial displacement or narrowing distribution of radial displacement of the particles. This helps to narrow the distribution of UV fluence received by the particles and ultimately enhances the reactor performance.

Chapter 5

CFD Simulation of Reactors with Multiple Lamps

5.1. Introduction

The effects of lamp arrangements on the overall performance of the water photo-disinfection reactor were analyzed. Similar to the CFD simulation for the single-lamp reactors, since lamp arrangement affects the average UV fluence rate inside the reactors, the performance of different reactors was assessed by comparing their disinfection log reduction ($-\ln(N/N_0)$). UV dosage was calculated by dividing the total UV lamp power by water flow rate. Keeping UV dosage constant across different reactors was achieved by varying the UV lamp power accordingly. All the lamps in a particular reactor were identical to each other in both size and power for the convenience of operation and maintenance. All the reactors are U-shaped and of the same size: straight length of 50 cm and radius of 44.5 mm; refer to Figure 3.2 for different reactor layouts.

Effects of lamp arrangement on UV fluence rate field inside the reactors are presented in Section 5.2, followed by lamp arrangement effects on water flow profile in Section 5.3. The reactor performance is compared in Section 5.4. Relationship between variables of interest is discussed in Section 5.5. Findings of this study are summarized in the Conclusions section.

5.2. UV fluence rate field

MATLAB was used to construct the UV fluence rate (P_R) field. Refraction, reflection and absorption of UV radiation were calculated. Figure 5.1 shows the UV fluence rate in different reactors with the same total power consumption of 39 W. That means for the 3-lamp reactor, the power of each lamp is 13 W while that for the 4-lamp reactor is 9.5 W. Figure 5.1a shows the UV fluence rate distribution at the plane perpendicular to the lamp axis in parallel reactors at half of the reactor length. The regions with warmest color in each reactor are the location of quartz jackets housing the UV lamps. It can be observed that, as the number of lamps increases, the maximum UV fluence rate inside the reactors decreases. This is because the outer radius of quartz jacket decreases with increasing number of lamps (in

order to keep internal volume of the reactors uniform) but its wall thickness is kept constant. Therefore, the light path in the quartz medium increases when light comes from emission points other than the one which is the projection of the reception point on the lamp axis. As the UV absorption coefficient of quartz is much larger than air and water, the increase in light path in the quartz medium decreases UV fluence rate. On the other hand, increase in number of lamps also makes UV fluence rate distribution more uniform, a result of decrease in the maximum distance between reception points and lamps.

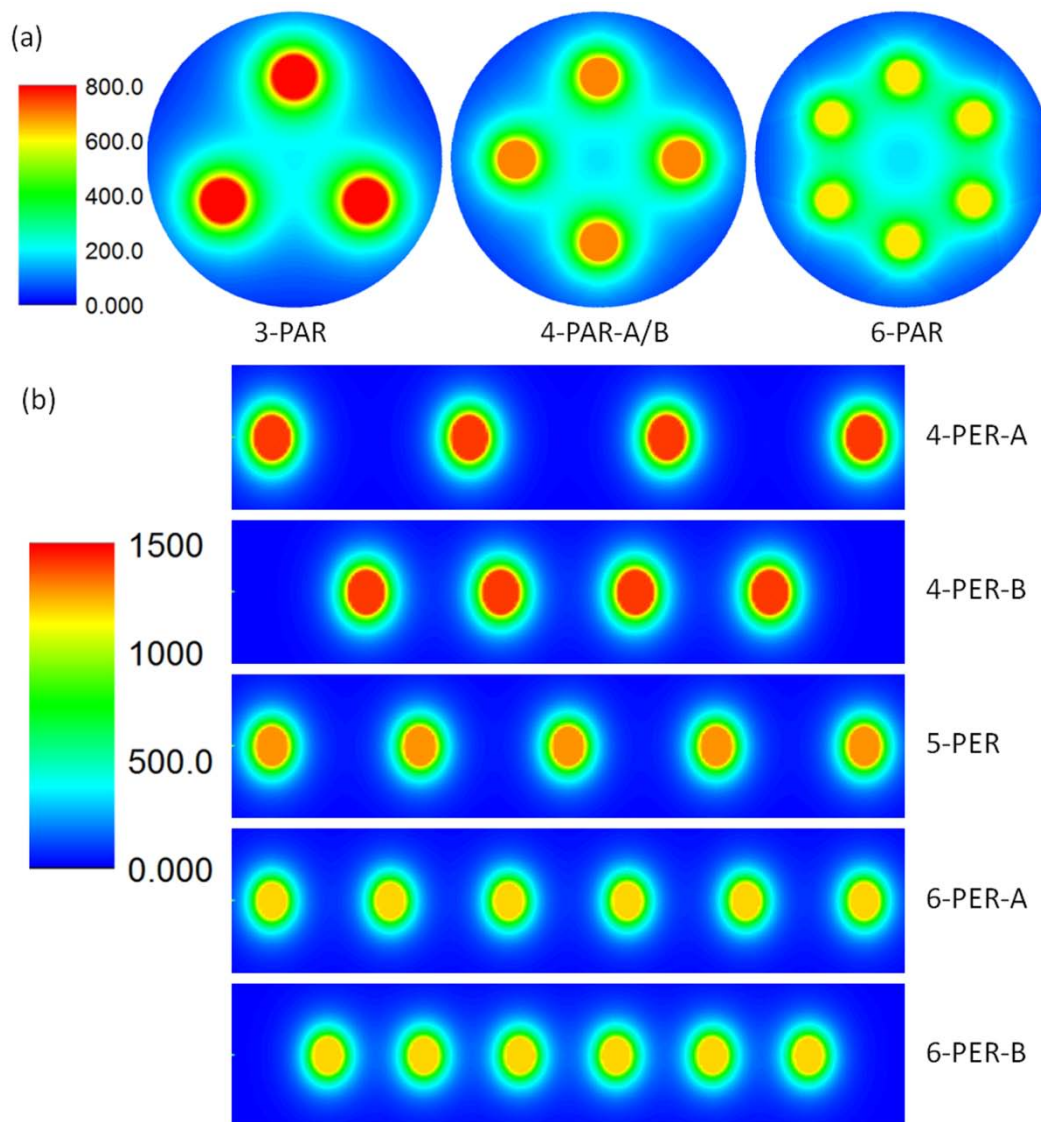


Figure 5.1 UV fluence rate in parallel (plot a) and perpendicular (plot b) reactors

Similar trends can also be observed in perpendicular reactors. Figure 5.1b shows the UV fluence rate distribution at the central plane normal to the lamps in perpendicular reactors. While perpendicular reactors offered higher maximum UV fluence rate than parallel ones (due to larger lamp radius and shorter total lamp length), the UV fluence rate distribution is less uniform.

Figure 5.2 shows the average UV fluence rate (\bar{P}_R) and standard deviation of UV fluence rate normalized by respective \bar{P}_R (S_{PR}), in various reactors. The single-lamp reactor is also included for comparison. All parallel reactors have higher \bar{P}_R but lower S_{PR} than all perpendicular reactors. Single-lamp reactor has the highest \bar{P}_R and its S_{PR} is between parallel and perpendicular reactors. For perpendicular reactors, Type A reactors have slightly lower \bar{P}_R and higher S_{PR} than their respective Type B counterpart, as a result of even distribution of light sources in the Type B perpendicular reactors. In parallel reactors, both \bar{P}_R and S_{PR} decrease slightly with increasing number of lamps, due to decrease in maximum UV fluence rate inside the reactors and more homogeneous distribution of UV fluence rate. While for perpendicular reactors, \bar{P}_R increases slightly and S_{PR} decreases with increasing number of lamps. In theory, higher \bar{P}_R and lower S_{PR} would enhance reactor performance.

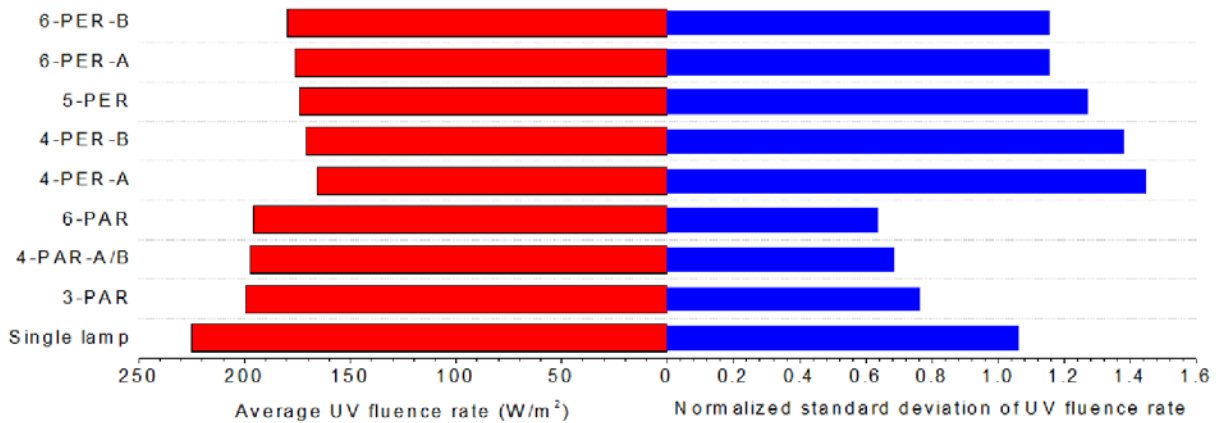


Figure 5.2 Average and normalized standard deviation of UV fluence rate in different reactors

5.3. Water flow profile

Different lamp arrangements result in different internal geometry of reactors. This would significantly affect the internal water flow profile and thus particle motion trajectories inside the reactors and also the reactor disinfection performance. For UV fluence rate field, higher \bar{P}_R and lower S_{PR} are, in theory, indicators of better disinfection performance. However, the effect of internal geometry on reactor performance is not so straightforward, and is further complicated by the effects of water flow rate, as previous studies have revealed the complex relationship between reactor disinfection performance and water flow rate [152].

Generally, higher water flow rate means higher turbulence and better mixing. The effects of different lamp arrangement on water flow profile under the same operating conditions were analyzed. Figure 5.3 shows the water flow velocity profile in the plane parallel to the reactor axis when the water flow rate was 1000 g/s. The number below each reactor type indicates the mass-average turbulence intensity of each reactor at that condition calculated by FLUENT. These high average turbulence intensities indicate highly turbulent flow in these reactors when water flow rate was 1000 g/s. Parallel reactors had higher average water flow velocity and lower average turbulence intensity than perpendicular reactors. This is because the lamps in the latter reactors are perpendicular to the overall water flow direction, acting as barriers and causing more turbulence when the water flow hit them. In parallel reactors, such barrier effect is only observable in the regions close to the water inlet and outlet. This is also the reason why the turbulence intensity in the 4-PAR-A reactor is higher than that in the 4-PAR-B reactor. In perpendicular reactors, regions of low water flow velocity near the reactor wall between the lamps are observed while such regions are absent in parallel reactors. Also, the distribution of water flow velocity in these reactors is less than that in parallel reactors. There is no obvious relationship between number of lamps and average turbulence intensity in each type of reactors.

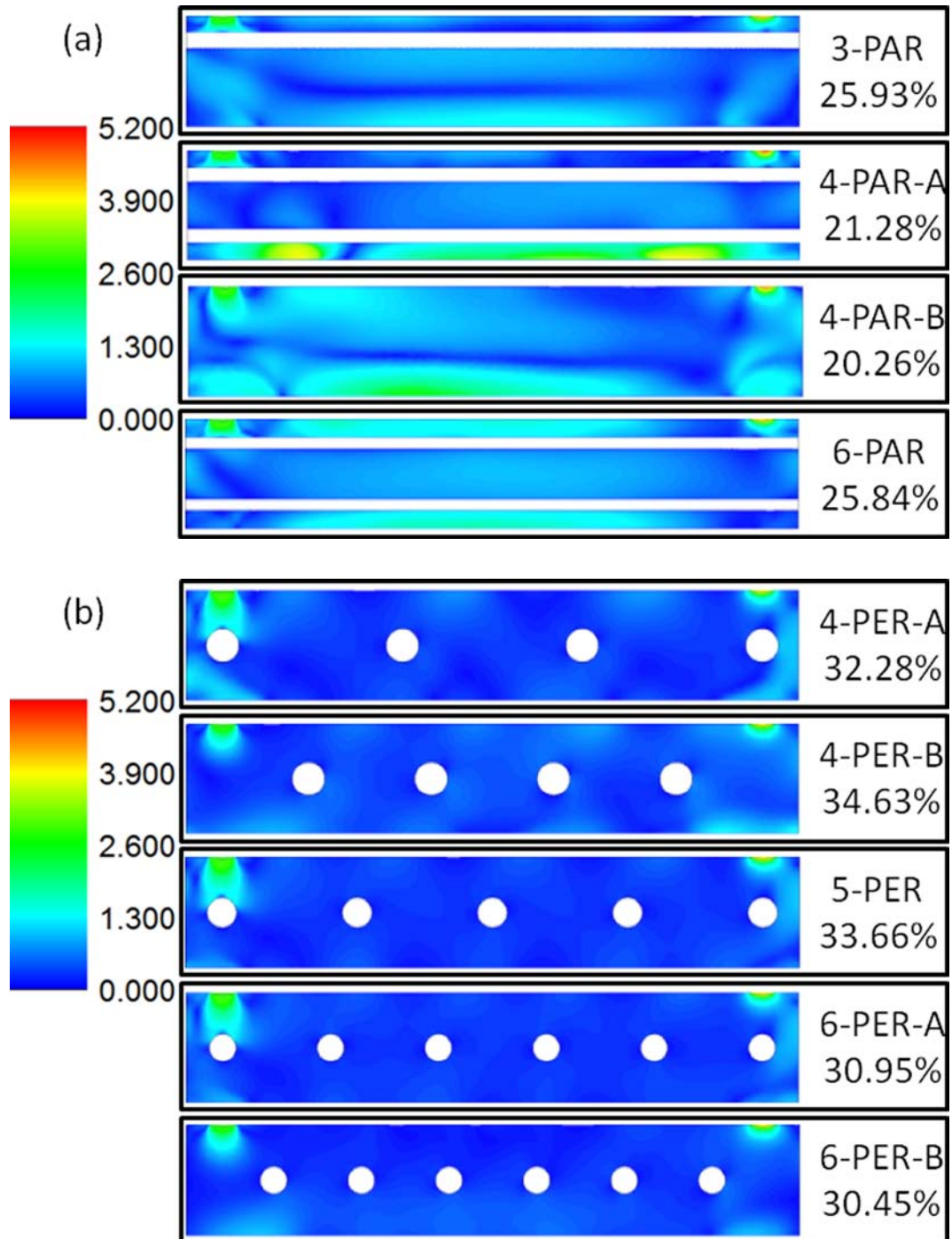


Figure 5.3 Water flow velocity profile in m/s and average turbulence intensity in parallel (plot a) and perpendicular (plot b) reactors at water flow rate of 1000 g/s

5.4. Reactor performance

With the simulation methodology described in Chapter 3, the reactor performance can be compared based on the same UV dosage consumed.

5.4.1. Type A and B parallel reactors

Figure 5.4a shows the comparison of log reductions of the 4-PAR-A, 4-PAR-B and single-lamp reactors when the UV dosage is 15 J/kg under different water flow rates. It can be observed that log reduction of the 4-PAR-A reactor decreases with increasing water flow rate while the 4-PAR-B reactor always performed inferior to the single-lamp reactor.

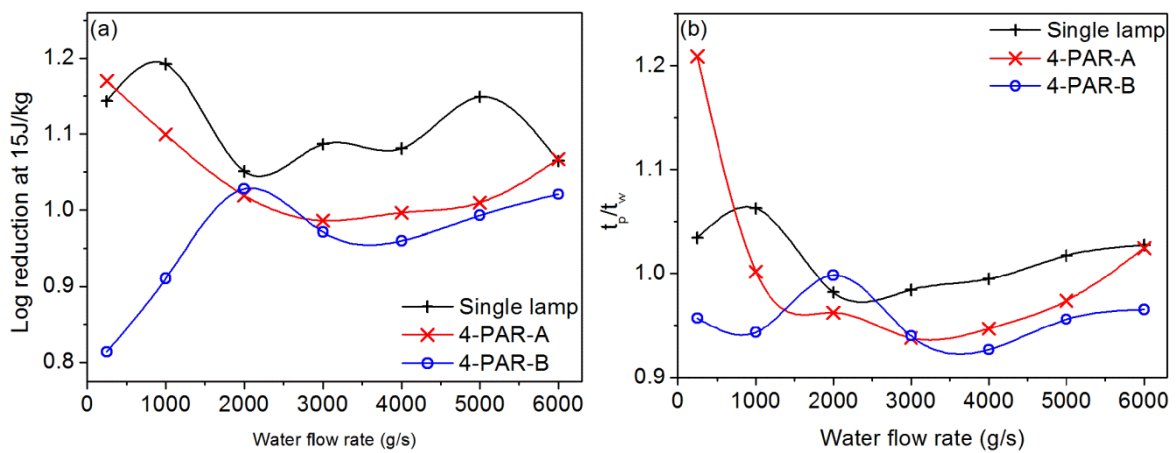


Figure 5.4 Comparison of log reduction (plot a) and average particle residence time over water residence time (plot b) of 4-lamp and single-lamp reactors

These differences observed in Figure 5.4a are probably due to their different average particle residence time. Figure 5.4b shows the ratio of average particle residence time of respective reactors over average water residence time ($\overline{t_p}/\overline{t_w}$). A corresponding pattern in log reduction and $\overline{t_p}/\overline{t_w}$ can be observed. One reason could be that in both 4-PAR-A and single-lamp reactors, there is a lamp located directly below the water outlet, acting as a barrier for particle exiting the reactor. Thus, $\overline{t_p}$ is enhanced by this effect, increasing both UV fluence received by the microorganism particles and reactor performance. Such effect is absent in the 4-PAR-B reactor, resulting its overall lowest log reduction. When the water flow rate increases, the barrier effect of the lamp is offset by the increase in hydraulic pressure and hence water velocity, diminishing the differences in both $\overline{t_p}/\overline{t_w}$ and the reactor

performance. Since the lamp is closer to the water outlet in the 4-PAR-A reactor, its barrier effect is the most prominent. Therefore, the trend of decreasing log reduction with increasing water flow rate is most observable for the 4-par-A reactor. Hence, type A parallel reactors are more favorable when designing photo-disinfection reactors.

Simulation of parallel Type A and Type B reactors demonstrates one of the advantages of TURF method. Since the UV fluence rate distribution inside these parallel reactors is the same, calculation results of UV fluence rate distribution for Type A can be directly used for simulation of Type B, saving much time for UV fluence rate calculations.

5.4.2. Parallel reactors

Figure 5.5 compares the performance of the parallel reactors. It can be observed that the disinfection performances of Type A parallel reactors are similar when the water flow rate was increased (the 6-PAR reactor is also of Type A). They all decreased with increasing water flow rate first, and then bounced back to oscillate around certain values. The decrease in log reduction with water flow rate at lower range is mainly due to changes in the particle residence time inside the reactors as mentioned in Section 5.4.1. At lower water flow rate, there are lamps located directly below the water outlet in Type A parallel reactors, acting as a barrier for particles to the exit, increasing the average particle residence time. As water flow rate increases, such effect is diminished by increase in hydraulic pressure, thus decreasing log reduction in these reactors while keeping UV dosage constant. This is also the reason why the difference in log reductions of all parallel reactors decreases with increasing water flow rate. Such barrier effect is absent in the 4-PAR-B reactor. Therefore, its log reduction changes differently with water flow rate when compared with other parallel reactors. Another trend is that, for Type A parallel reactors, log reduction increases with increasing number of lamps. Since the \bar{P}_R of all parallel reactors are close to each other, the increase in disinfection performance of parallel reactors with more number of lamps is possibly due to lower S_{PR} (Figure 5.2) and more homogeneous water flow/velocity distribution (Figure 5.3). Section 5.5 provides more detailed discussion.

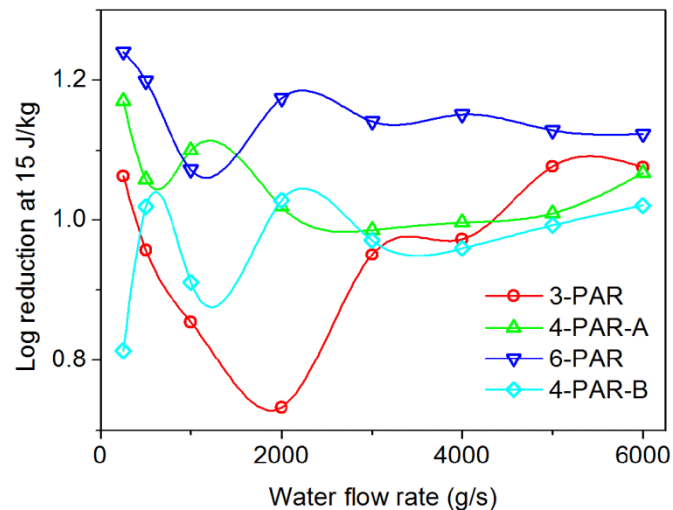


Figure 5.5 Disinfection performance comparison of parallel reactors

5.4.3. Perpendicular reactors

Figure 5.6 shows the log reduction of the perpendicular reactors over different water flow rate when UV dosage is 15 J/kg. The general trend is that log reduction of all perpendicular reactors decreases with increasing water flow rate. The barrier effect mentioned above can still be applied here. In perpendicular reactors, all the lamps are perpendicular to the general water flow direction, acting as barriers. At low water flow rate, due to initial direction at the water inlet, water as well as particles would flow around these lamps, increasing average residence time of particles. As water flow rate increases, water flow tends to by-pass these lamps to avoid additional resistance, making these barriers less effective. Generally, Type A parallel reactors perform better than their respective Type B counter parts over most water flow rates, despite slightly higher \bar{P}_R in Type B perpendicular reactors, mainly due to the location of lamps directly below water inlet and outlet and hence better barrier effect in Type A reactors.

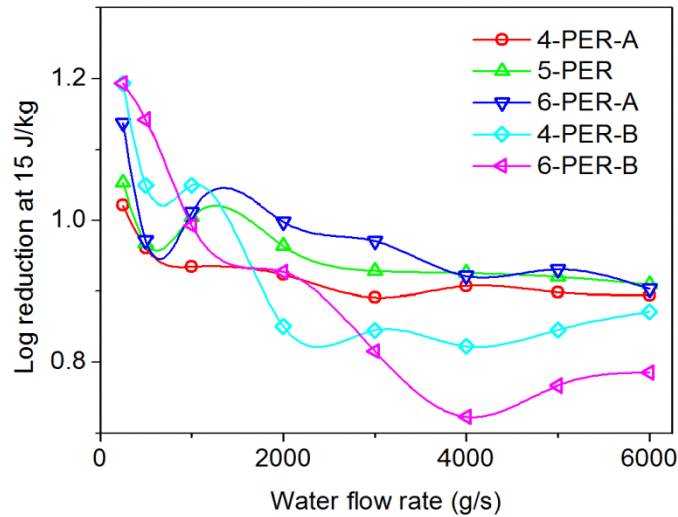


Figure 5.6 Disinfection performance comparison of perpendicular reactors

Figure 5.7 shows the water flow vector profile at the central plane of 6-PER-B reactor at selected water flow rates. The scales for each graph is adjusted according to the water flow rate, i.e. the water velocity represented by the warmest color in the 6000 g/s graph is 24 times of that in the 250 g/s graph. It can be observed that as the water flow rate increases, water flow velocity normal to the central plane in the regions between the lamps becomes lower relative to the average values, indicated by smaller vector magnitude and darker color in Figure 5.7. These regions have the highest UV fluence rate inside the reactors. Lower water velocity normal to the central plane in these regions means part of particles would be trapped for longer time in these regions while other particles will not enter these regions but by-pass through regions near the reactor wall and exit the reactor directly. This widens the distribution of UV fluence received by the particles and increases the normalized standard deviation of UV fluence received by particles (S_U), as shown by the numbers in Figure 5.7. In conjunction with the decrease in the particle residence time relative to average water residence time and thus lower \bar{U}_p , the log reduction decreases as water flow rate increases. The relationship between number of lamps and reactor performance is more complicated in perpendicular reactors than parallel ones. Among the reactors studied, 6-PER-A reactor has the highest overall log reduction when water flow rate exceeds 1000 g/s.

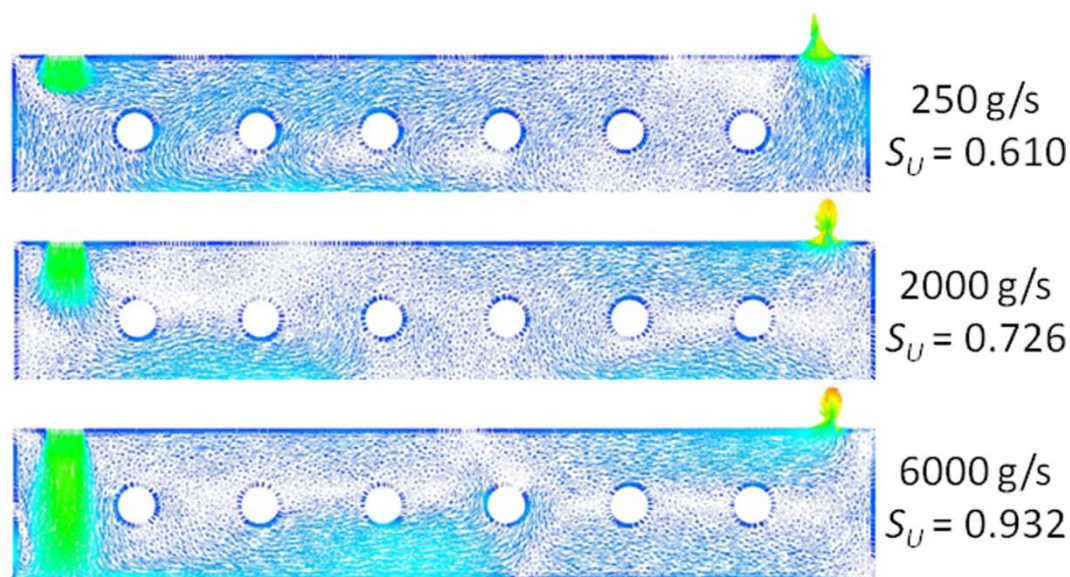


Figure 5.7 Water flow vector profile at different water flow rates in the 6-PER-B reactor

5.4.4. Comparison among all reactors

Figure 5.8 compares log reductions of 6-PER-A, 6-PAR and the reference single-lamp reactors under different water flow rates. The first two reactors are chosen for their highest overall log reduction among perpendicular and parallel reactors respectively. 6-PER-A reactor has the lowest log reduction at all water flow rates among the three in Figure 5.8. 6-PAR and single-lamp reactors have comparable performance. It should also be noted that single-lamp reactor performs better than all parallel reactors other than 6-PAR. This is mainly attributed to the higher \bar{P}_R in the single-lamp reactor. Therefore, for better performance, it is not attractive to increase number of lamps in UV water disinfection reactors. In addition, increasing number of lamps in reactors require more spare lamps for industrial operation, hence increasing the operation cost. However, reactors with multiple lamps can still be favorable. In industrial reactors, high power UV lamps are usually used for high water flow rate. Increasing number of lamps in each reactor reduces power of each lamp. Thus, the ventilation duty to remove the excess heat inside the quartz jacket can be reduced in reactors with multiple lamps.

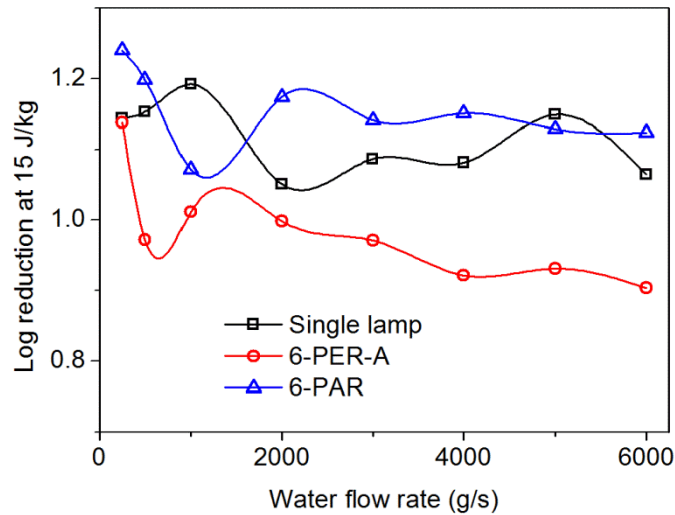


Figure 5.8 Disinfection performance comparison of best parallel and perpendicular reactors with single-lamp reactor

Simulation of these lab-scale reactors shows that multi-lamp reactors do not perform significantly better than single-lamp reactors for the same UV power in total, despite its more evenly distributed UV fluence rate. Only reactors with a lamp located directly below the outlet offer more disinfection under low water flow rate. However, multi-lamp reactors have been popular for industrial water disinfection. This is probably due to the much larger cross-sectional area of industrial reactors and high water flow rate.

5.5. Normalized standard deviations

Since S_U , the normalized standard deviation of UV fluence received by microorganism particles, is a good indicator for better reactor performance when \bar{U}_p is close to each other, it is important to study its origin for better reactor design and operation. In theory, S_U is dependent on both S_{PR} and normalized standard deviation of particle residence time (S_t). The normalized standard deviation is chosen due to large difference in standard deviation of particle residence time under different water flow rates. Figure 5.2 shows that perpendicular reactors have higher S_{PR} than parallel reactors. However, the difference in S_U of the two types of reactors is not so significant when S_t is about the same, as shown in Figure 5.9. S_{PR} thus has little impact on S_U . The impact of \bar{U}_p on reactor performance is more significant. Therefore, it is reasonable to conclude that when designing UV disinfection reactors, especially the arrangement of UV lamps, the major aim is to increase \bar{U}_p . The

water flow rate should be chosen such that S_t is at the minimum. In addition, the parallel reactors have smaller S_U than perpendicular reactors at the same S_t , which is consistent with the above observation that parallel reactors perform superior to perpendicular reactors.

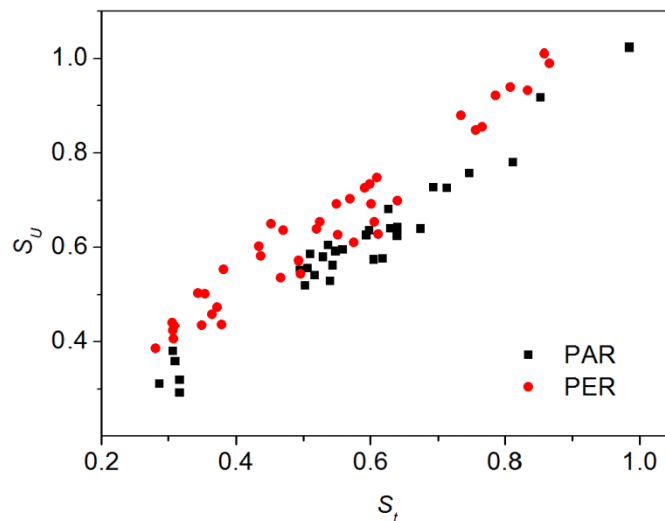


Figure 5.9 Relationship between normalized standard deviation of UV fluence (S_U) and that of residence time (S_t)

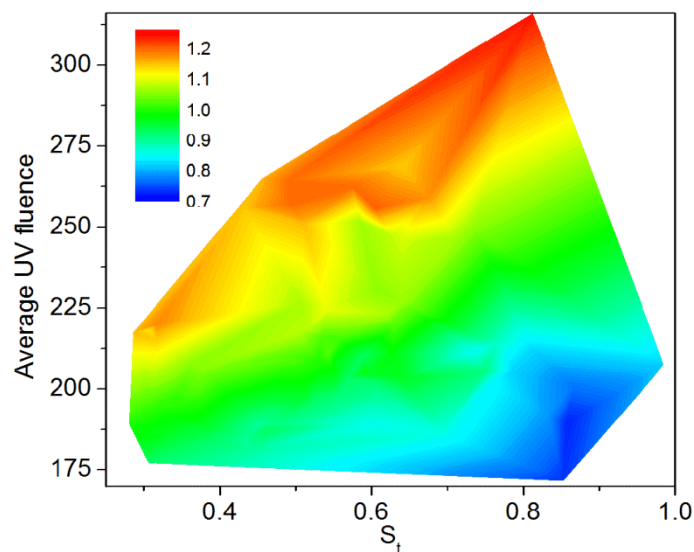


Figure 5.10 Contour plot of log reduction versus average UV fluence (\bar{U}_p) and S_t

The reactor performance is dependent on UV fluence and water flow profile. \bar{U}_p was found to be a more significant variable than S_{PR} . On the other hand, S_t influences S_U and is solely dependent on water flow profile. Figure 5.10 shows the relationship between reactor performance, \bar{U}_p and S_t for all reactors analyzed in this work, with a total of 80 data points.

It can be observed that higher \overline{U}_p and lower S_t favor better reactor performance, which is consistent with the theory. Figure 5.10 shows smooth transition from high to low disinfection performance over the whole range, indicating that the relationship between these three variables would be similar in difference reactor types.

5.6. Conclusions

The effects of various lamp arrangements on the performance of different UV water disinfection reactors were analyzed. Direction, orientation and number of lamps were varied. The overall effect on reactor performance was found to be complex. Parallel reactors are more efficient than perpendicular reactors. Type A reactors with lamps directly below water inlet and outlet enhances reactor performance due to the barrier effect of the lamps to the exiting particles. Higher water flow rate diminishes this “barrier” effect in reactors with multiple lamps, lowering log reduction under constant UV dosage. Reactors and operating conditions that provide higher average UV fluence rate and lower normalized standard deviation of particle residence time favor the reactor performance. This work provides new physical insights for understanding the effect of lamp arrangements on the performance of UV disinfection reactors.

Chapter 6

Modeling and Optimization of Photo-Disinfection Reactors

6.1 Introduction

Previous two chapters have shown that the relationship between photo-disinfection reactor performance and design and operating variables is complex. Simple algebraic equation is not capable of describing the reactor performance. Two data-driven modeling methods, Artificial Neural Network (ANN) and Genetic Programming (GP), were utilized for modeling and optimization of these reactors since they are able to mimic complex relationships. The developed ANN and GP models were used for subsequent optimization of UV water disinfection process for multiple objectives, and for further testing the generalization ability of these models using the new input variable sets given by optimization. Almost all earlier studies simply developed ANN and/or GP models, and did not use and test them for an application such as optimization. In the models, the input design variables were reactor length and radius, number and direction of lamps, and lamp jacket radius, and the input operating variables were water flow rate and UV dosage; thus, there were 7 input variables. The microorganism log reduction of the reactors was the only output variable.

ANN and GP Modeling, and subsequently optimization algorithms are described briefly in Section 6.2. Models constructed using ANN and GP are compared in Sections 6.3.1 and 6.3.2. Section 6.4 discusses the optimal design and operating conditions obtained using different models and multi-objective optimization (MOO). Selected Pareto-optimal solutions were simulated in CFD software FLUENT to compare the generalization ability of ANN and GP models (i.e. predicting output for new input values not used in the modeling step); these are presented and discussed in Sections 6.4.1 and 6.4.2. Optimal values of design and operating variables of the UV water disinfection process are analyzed in Section 6.4.3. Findings are summarized in the Conclusions section.

6.2. ANN and GP modeling

The seven input variables and their ranges used for obtaining the data for modeling are shown in Table 6.1. The lamp direction means the direction of the lamp relative to the

reactor axis (refer to Section 3.2.2). Plots in the first row of Figure 6.1 show three parallel type reactors while the second row shows three perpendicular type reactors. The grey circles are water inlets and outlets. In the single-lamp reactors, lamps were placed along the U-shaped reactor axis. All the reactors considered for data-driven modeling are Type A reactors due to their better performance over Type B counter parts (refer Section 3.2, Figures 3.1 and 3.2, Section 5.4.1). Total number of data sets for model development was 2,068.

Table 6.1 Input variables and their ranges used for obtaining the data for modeling

Lamp direction	Perpendicular (1) or parallel (0)
Number of lamps	4, 5, 6 for perpendicular, and 1, 3, 4, 5, 6 for parallel
Lamp jacket radius	9 to 15 mm
Reactor length	0.5 to 1.2 m
Reactor radius	35 to 50 mm
Water flow rate	0.25 to 7.5 kg/s
Dosage	5 to 155 J/kg

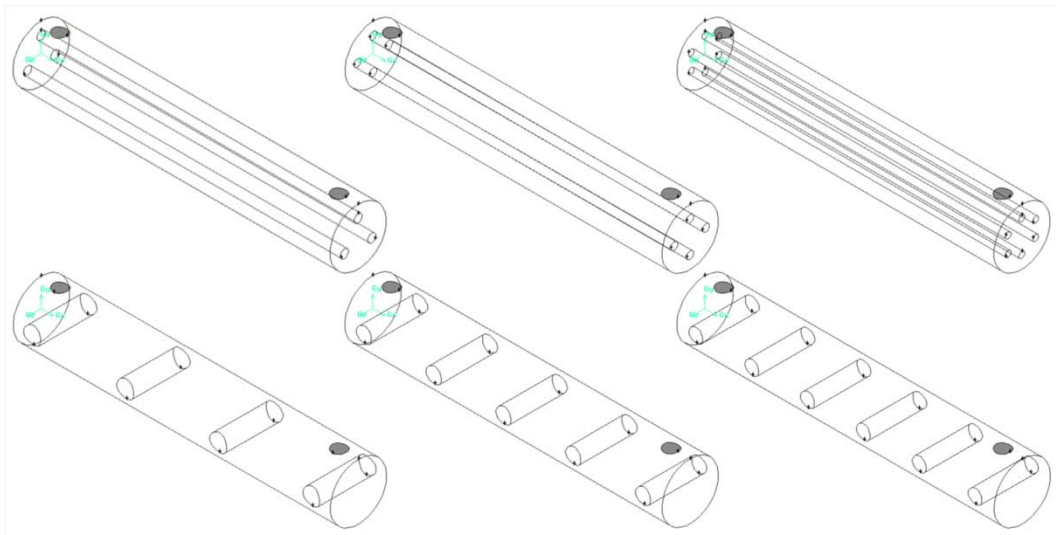


Figure 6.1 Reactor layouts: parallel type in the top row and perpendicular type in the bottom row, grey circles are water inlets and outlets

6.2.1. ANN modeling

Inspired by biological neural networks, ANN consists of a few layers of interconnected artificial neurons which can transmit information to their connected neighbours through various kinds of transfer functions and weights. Although the computation methods connecting neurons are simple, ANN has been shown to be able to recognize complex patterns between inputs and outputs. Application of ANN in modeling fluid phase phenomena is quite new. With simulation results from CFD software as the training data sets, ANN was able to model complex relationships between selected input and output variables in fluid and multi-phase reactors [10, 44]. In the present study, ANN module in Matlab was used to construct models for UV water disinfection process, for the first time. Feed-forward with back-propagation for training was selected as the network type. Modeling parameters such as structure (number of hidden layers and neurons) and transfer functions were tuned to obtain a model with minimum mean square error and lowest complexity.

6.2.2. GP modeling

GP models were constructed using the BioGP described by Giri et al. [46]. These models have tree structures with different mathematical operators linking the nodes. One limitation of ANN is that the network designer has fewer choices for type of mathematical operations connecting the neurons. All neurons in the same layer are subject to the same type of transfer function, and input value of each neuron is the summation of outputs of all neurons in the upstream layer according to their respective weights and biases. On the other hand, GP offers greater flexibility in mathematical operations linking nodes in the tree structure. Besides normal double arity functions such as plus, subtraction, multiplication and division, single arity functions such as square, log and square roots were also used in these tree structures in this work. The tuning parameters for BioGP model construction were maximum number of nodes linking to each node and maximum depth of the trees. High numbers mean more complex and usually more accurate model.

6.2.3. Multi-objective optimization

One direct application of models constructed using previous methods is for optimization. UV disinfection is a capital-intensive process, and majority of the operating cost comes from electric power consumption of UV lamps. Since UV dosage received by unit

mass of water (with units of J/kg) is directly proportional to the UV lamp power consumption, an efficient UV disinfection reactor should be able to kill more microorganisms with less UV dosage. Therefore, minimization of UV dosage and maximization of log reduction of microorganisms in the reactors were chosen as the two objectives for MOO. A Matlab-based Non-dominated Sorting Genetic Algorithm II (NSGA-II) program, NGPM (version 1.4), developed by Lin [153], was used in this work as the MOO tool. The Pareto-optimal solutions obtained using both ANN and GP models were analyzed and compared. Relationship between optimal design and operating variables was studied to discover general trend in efficient reactor designs. The accuracy of the ANN and GP models was verified again via TURF simulation of selected Pareto-optimal solutions.

6.3. Accuracy of ANN and BioGP models

6.3.1. ANN model

To avoid over-fitting of training data, the number of hidden layers in the ANN model was limited to just one. Number of neurons in this hidden layer was varied from 7 to 30. During the initial optimization attempts, it was observed that the ANN model was not able to capture the relationship between UV dosage and log reduction, i.e. the log reduction did not increase with UV dosage when the input set was new to the model (i.e., not in the training set). Under extreme conditions, the log reduction calculated by the ANN model changed only by a few percent when UV dosage increased from 5 to 155 J/kg. Possible reason for this is that, although UV dosage is the dominant factor for log reduction, it is only one of the seven inputs in the ANN model. After transmission through hidden layer, the output, i.e. the log reduction was not able to respond to the change in UV dosage up to the expectation. In order to overcome this problem, training data sets were pre-processed. One particular reactor under certain operating conditions was chosen as the reference. Its log reduction with respect to different UV dosages was modeled as a 3rd order polynomial, which was chosen because the UV response curve of the target microorganism used in this work was an order-3 polynomial. It is also accurate enough to describe the reference reactor performance variation with the UV dosage. All the log reductions in the training data sets were normalized by the log reduction of this reference reactor at their respective UV dosage. The output of the normalized training data sets varied from 0.48 to 1.4 instead of 0.3 to 7.2 in the un-processed data. As shown in plot (a) of Figure 6.2, 20 hidden neurons were enough to give good agreement between

model results and the training data sets. Average relative absolute error of 2.3% over the entire data set indicates that the ANN model was able to simulate the training data with satisfactory accuracy.

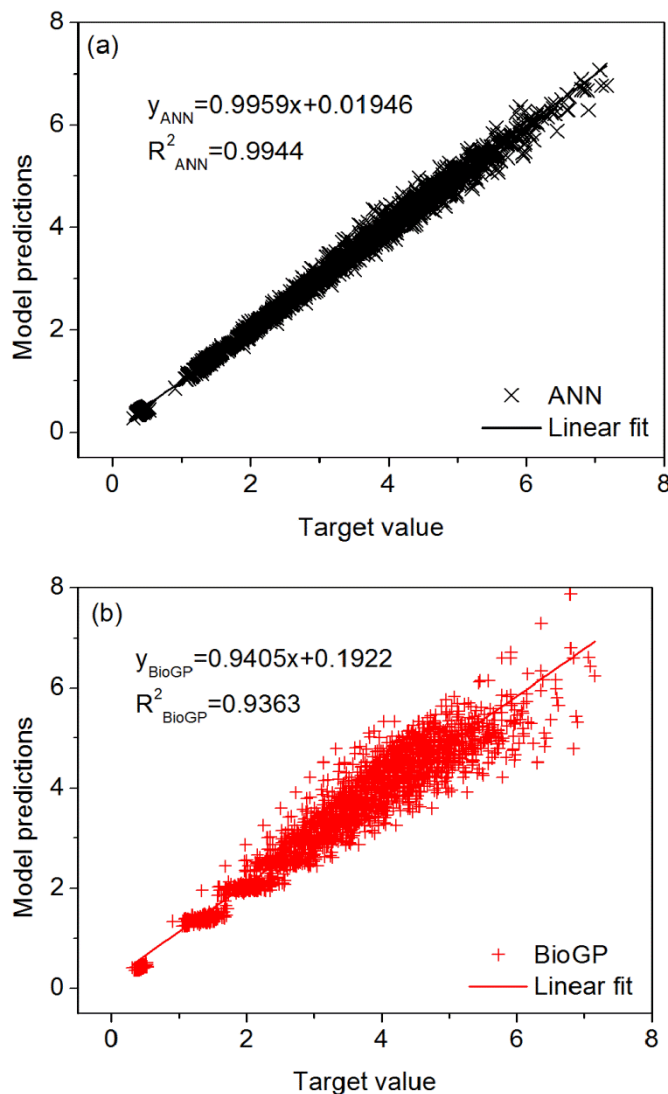


Figure 6.2 Parity plots of output predictions by ANN model (plot a) and by BioGP model (plot b), versus actual output (target) values

All the models with different number of hidden neurons were able to model the UV disinfection with satisfactory accuracy, with maximum relative absolute error at just over 5% over the entire training data set (for the model with 7 hidden neurons). As expected, increasing number of hidden neurons from 7 to 20 decreased modeling error from 5% to 3%. Further increasing number of hidden neurons to over 20 did not improve the model accuracy much. Note that 20 hidden neurons required 181 parameters (weights and biases) in the ANN

model, which is one order lower than the number of training data sets (> 2000). Therefore, scope for over-fitting is minimal. All the transfer functions were *tansig* (tangent sigmoid). The *purelin* (linear) and *logsig* (log-sigmoid) transfer functions were found to be less accurate in modeling the UV disinfection process.

6.3.2. BioGP model

Both the maximum number of nodes connected to each node and maximum depth of the tree structure in the BioGP models were varied from 3 to 5. The models were also constructed with and without single arity functions. Training results revealed that the model accuracy did not improve much with increasing model complexity. There is even an increase in relative absolute error from 8.4% to 10% when both maximum nodes connected to each node and depth of tree increased from 3 to 5. Hence, the simplest model (where maximum number of nodes connected to each node and maximum depth of tree are both 3) was chosen for analysis and MOO discussed later. Increasing the model complexity would bring the risk of over-fitting. Plot b of Figure 6.2 compares the predictions by the BioGP model having at most 3 nodes connected to each node and depth of the tree was 3, with actual values.

As can be observed from Figure 6.2, the BioGP model is less accurate than the ANN model, with a significantly larger average relative absolute error of 8.4%. The former model predictions are more scattered from the diagonal line than the ANN results, primarily due to lower number of parameters in the former than in the latter model. The type of mathematical operations linking the nodes was also limited. Inclusion of new mathematical operation(s) should be beneficial to model accuracy as inclusion of single arity functions during BioGP model training improved accuracy. However, larger error may not always mean a worse model. The ability of the model to generalize, i.e. to give an accurate prediction with new input data that were not included in the training data sets, is more important. For example, the ANN model constructed using the un-processed training data performs poorly in this aspect although it was able to give a much smaller error than the BioGP model. On the other hand, the BioGP model was able to predict log reduction with different UV dosage and new input sets well, without the need to pre-process the training data. This is further discussed in the later section.

6.4. Multi-objective optimization

After developing the ANN and BioGP models, a Matlab-based Non-dominated Sorting Genetic Algorithm II (NSGA-II) program (NGPM) was used to find the optimal design and operating variables of the UV disinfection process. Note that this optimization employs either the ANN or BioGP model developed earlier, and is different from the optimization involved in developing the ANN and BioGP models. The two objectives for finding the optimal design and operating variables of the UV disinfection process were minimization of UV dosage and maximization of log reduction. Since NGPM deals with minimization of two objectives, the UV dosage and the negative of log reduction were minimized during MOO. Default parameters in NGPM were used. After 100 generations, the Pareto-optimal solutions reached a plateau and no further improvement was observed for more generations using both models. MOO using the BioGP model already developed took significantly longer time (around 10 hours) than that using the ANN model developed earlier (around 2 hours) for the same number of generations (100) on the same computer. Possible reason may be that the ANN model is constructed using the built-in functions of Matlab, while the BioGP model is developed by other researchers. The calculation speed optimization of ANN may be better.

6.4.1. Process optimization using the ANN model

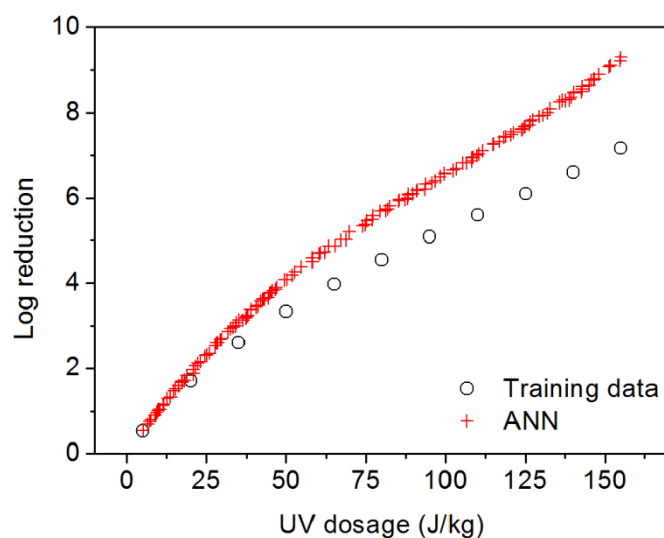


Figure 6.3 Pareto-optimal solutions based on the ANN model; highest log reduction at some UV dosages in the training data are also shown for comparison

Figure 6.3 shows the Pareto-optimal solutions obtained using the ANN (with 20 hidden neurons) model developed earlier for the UV disinfection process. For comparison, the best possible log reduction at respective UV dosage in the training data is also shown in this figure. Pareto-optimal solutions found using the ANN model mostly give higher log reduction compared to the training data over the entire UV dosage range. MOO was repeated using ANN models developed with 10 to 25 hidden neurons, which led to Pareto-optimal solutions with similar log reduction as in Figure 6.4. However, input variables of these similar Pareto-optimal solutions are quite different from one another. This is possible since different values of decision variables could generate similar output in this complex system.

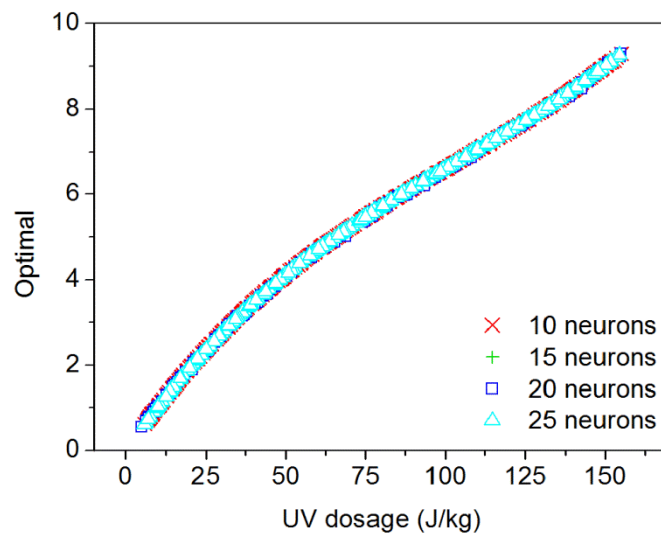


Figure 6.4 Pareto-optimal solutions found using ANN models with different number of hidden neurons

To verify the optimized solutions, two Pareto-optimal solutions at the two ends of the curve in Figure 6.3 were chosen and simulated using the method described in Chapter 3 via CFD; optimal values of decision variables corresponding to these solutions (labelled as POS1-ANN and POS2-ANN) are given in Table 6.2. Note that this simulation using CFD software is equivalent to performing an experiment using the optimal values of design and operating variables, and will be referred to as CFD test hereafter. The input variables and output results of CFD test and the log reduction predicted by both the ANN and the BioGP models are listed in Table 6.2. These results show that both models are not able to predict correctly the log reduction given by CFD test for POS1-ANN solution, and that the BioGP model predicts better than the ANN model for POS2-ANN solution.

Table 6.2 Selected Pareto-optimal solutions and their CFD test results

Optimal solution	POS1-ANN	POS2-ANN	POS3-BioGP	POS4-BioGP
Lamp direction	parallel	parallel	parallel	parallel
Number of lamps	4	4	3	4
Water flow rate (kg/s)	1.900	0.254	0.250	0.250
Reactor length (m)	1.092	0.561	1.200	1.200
Lamp radius (cm)	0.910	0.969	0.913	0.900
Reactor radius (cm)	4.26	4.10	5.00	4.89
UV Dosage (J/kg)	154.99	5.00	145.00	6.38
Log reduction from the CFD test	7.410	0.392	8.169	0.616
Log reduction predicted by the ANN model	9.298	0.528	8.700	0.666
Log reduction predicted by the BioGP model	5.216	0.404	7.688	1.043

Since it is hard to determine which of the two models is better in predicting log reduction for new input variables based on POS1-ANN and POS2-ANN, the UV dosage of each of the two Pareto-optimal solutions was varied in the CFD test while keeping all other input variables unchanged. The results are shown in Figure 6.5. All the points in Figure 6.5a have the same input variables such as lamp direction (parallel), number of lamps (4), water flow rate (1.900 kg/s), reactor length (1.092 m), lamp jacket radius (0.910 cm), and reactor radius (4.259 cm) as POS1-ANN in Table 2. Their UV dosage was varied from 5 to 155 J/kg. Similarly, all the points in Figure 6.5b have the same input variables as POS2-ANN (parallel

lamps, 4 lamps, water flow rate: 0.254 kg/s, reactor length: 0.561 m, lamp jacket radius: 0.969 cm, reactor radius: 4.10 cm), except the UV dosage.

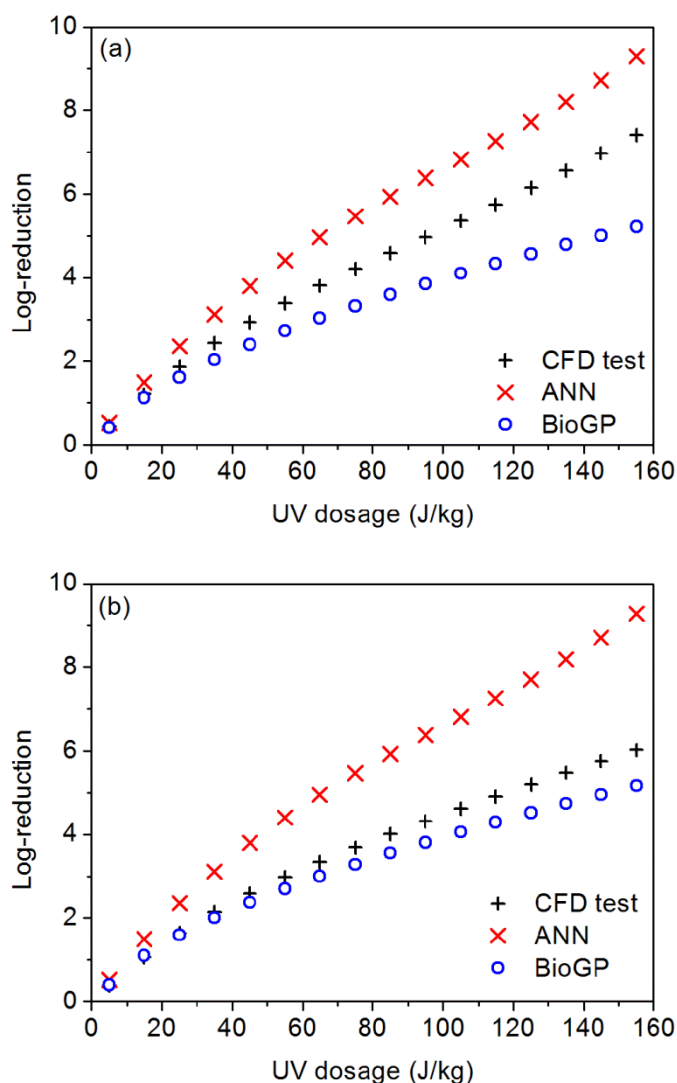


Figure 6.5 Comparison of model predictions with CFD test for input variables of POS1-ANN (plot a) and POS2-ANN (plot b), with varying UV dosage

It is observed from Figure 6.5 that the ANN model tends to over-estimate log reduction, especially at high UV dosage. This is possibly due to over-fitting of the training data as a result of large neural network structure, which lowers the generalization ability of the ANN model. For input variable set of POS1-ANN, both models perform poorly, and the errors of both models are comparable, as shown in Figure 6.5a. The BioGP model performed better for input variable set of POS2-ANN, as indicated by the smaller gap between BioGP curve and CFD test curve in Figure 6.5b.

6.4.2. Process optimization using BioGP model

Similar optimization procedure and subsequent CFD test were also conducted for the BioGP model. Results in Figure 6.6 show that optimization using the BioGP model was able to generate Pareto-optimal solutions slightly better than the best possible training data over the entire range of UV dosage; however, these solutions are inferior to those found using the ANN model shown in Figure 6.3.

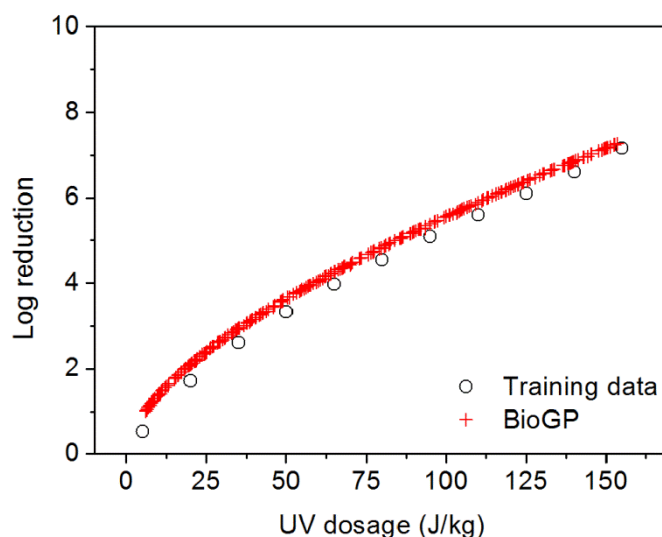


Figure 6.6 Pareto-optimal solutions based on the BioGP model; highest log reduction at some UV dosages in the training data are also shown for comparison

Two Pareto-optimal solutions at the two ends of the curve in Figure 6.6 are chosen for CFD testing; values of their input (design and operating) variables are given in Table 6.2 (labelled as POS3-BioGP1 and POS4-BioGP2). Comparison of log reduction predicted by the ANN and the BioGP models with CFD test results (Table 6.2) show that both models are not able to predict correctly the log reduction given by CFD test for POS3-BioGP solution, and that the ANN model predicts better than Bio-GP model for POS4-BioGP solution.

Again, the UV dosages of two Pareto-optimal solutions obtained using the BioGP model, were varied for conducting the CFD test. Figure 6.7a and 6.7b show the results for input variable sets of POS3-BioGP and POS4-BioGP respectively, with UV dosages varying in the same way as those in Figure 6.5. Both models perform better for these two input variable sets than those in Figure 6.5 in terms of the difference in log reduction between CFD simulation and model calculation. The BioGP model has smaller error at lower and middle UV dosages, while the ANN model performs better at the high UV dosage end. From the

results in Figure 6.5 and 6.7, it can be concluded that the BioGP model is relatively more accurate for predicting log reduction for new input variable sets. This is probably because the complexity of the BioGP tree structure in this work is limited, enabling the BioGP model to generalize over new input variable sets. Over-fitting of the noisy data is avoided.

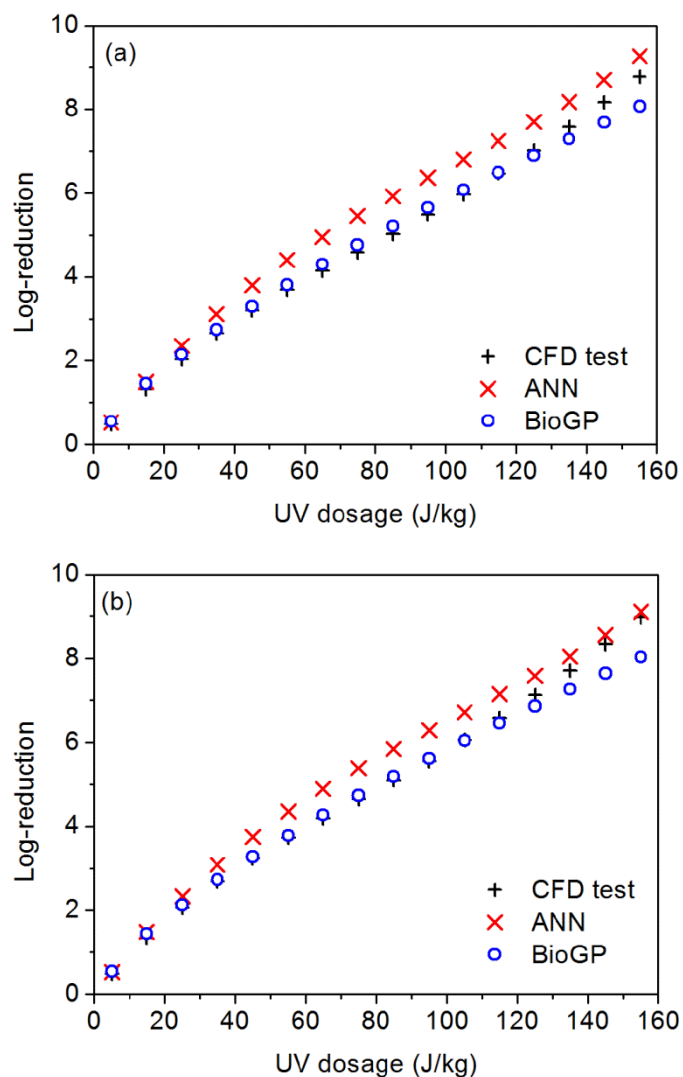


Figure 6.7 Comparison of model predictions with CFD test for input variables of POS3-BioGP (plot a) and POS4-BioGP (plot b), with varying UV dosage

It can be concluded that the ANN model developed for UV disinfection reactor is not suitable for optimization. Figure 6.5 shows that the CFD test results are lower than those predicted by the ANN model. This overestimation of the ANN model may lead to incorrect optimal solutions thus making it unable to find the “real” optimal solutions. For instance, Table 6.2 shows that the CFD test result of POS3-BioGP solution is higher than that of

POS1-ANN solution, even though the UV dosage of the former is lower. The CFD test result (7.410) of POS1-ANN solution is only slightly better than the best training data (7.159) when UV dosage is 155 J/kg. On the other hand, Figure 6.7 shows that the CFD test result for the input variable sets of both POS3-BioGP and POS4-BioGP solutions can reach above 8.5 when UV dosage is 155 J/kg. Therefore, although the ANN model is able to provide smaller modeling error as discussed above (Figure 6.2), the BioGP model is better suited for optimization of the UV disinfection reactor since it is able find Pareto-optimal solutions that have higher log reduction in CFD test.

6.4.3. Optimal values of design and operating variables

Since the BioGP model seems to better for optimizing the design variables of UV disinfection reactor, only the Pareto-optimal solutions obtained using the BioGP model were analyzed for the relationship between reactor performance and optimal values of design variables. Figure 6.8 shows some of the design and operating variables of the Pareto-optimal solutions. Firstly, all the Pareto-optimal solutions obtained using the BioGP model have water flow rate near the lower boundary, i.e. 0.25 kg/s. Previous studies have revealed that, at low water flow rate, microorganism particles would stay longer in the reactors relative to water (Section 5.4.1). This barrier effect helps to increase the UV fluence received by the particles, enhancing the reactor performance. This means a batch of UV disinfection reactors connected in parallel with lower water flow rate in each reactor is more favourable than the same number of identical reactors connected in series when the total water flow rate is constant. Secondly, reactor lengths in these Pareto-optimal solutions are close to the upper bound (1.2 m). Theoretically, longer reactors offer longer particle and water residence time. This provides more mixing in radial direction, which was found to correlate positively with better reactor performance (Section 4.8).

The cross-sectional area of the Pareto-optimal reactors is near the high end, i.e. the quartz jacket radius is close to the minimum value of 9 mm and the reactor radius is near the upper limit of 50 mm (Figure 6.8b). The reason for this is similar to that for the optimal reactor length. Larger reactors offer longer residence time and better radial mixing, and hence better reactor performance. In addition, smaller quartz jacket radius offers more regions of higher UV fluence rate, which increases the UV fluence received by microorganism particles

and finally enhances reactor performance. Therefore, the quartz jacket radius should be as small as possible for optimal reactor design. However, UV lamps in industrial reactors are usually of very high power, and air circulation for their cooling is necessary inside the quartz jacket. Small quartz jacket radius may result in poor cooling and lowers lamp life, increasing operating cost. On the other hand, larger reactor radius increases residence time and decreases average UV fluence rate inside the reactor by increasing regions of lower UV fluence rate at the same time. Thus, although larger reactor radius enhances reactor performance in this work, it may not be the case if the reactor radius further increases. In short, an optimal UV disinfection reactor should have a large volume.

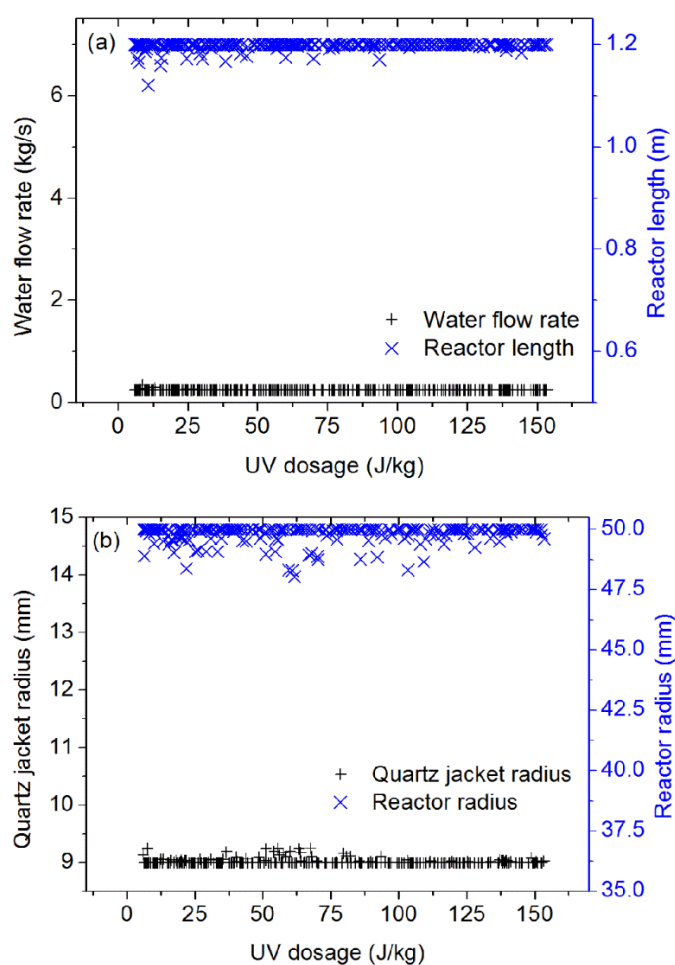


Figure 6.8 Selected design and operating variables of the Pareto-optimal solutions obtained using the developed BioGP model

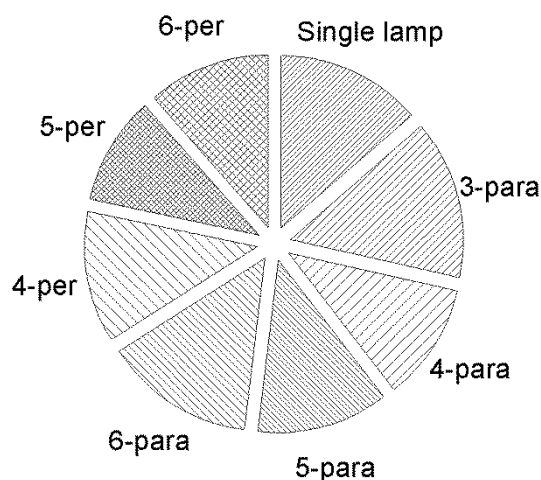


Figure 6.9 Distribution of lamp arrangements in the Pareto-optimal solutions

No clear trend was observed in optimal lamp direction and number of lamps. As shown in Figure 6.9, number of Pareto-optimal solutions of each lamp arrangement is comparable to one another. There is also no clear relationship between optimal UV dosage and optimal type of reactor (parallel/perpendicular and number of lamps). The parallel type reactors including the ones with single lamp are generally more favourable as they outnumber perpendicular type in the Pareto-optimal solutions (66% for parallel and 34% for perpendicular reactors). In summary, optimal values of continuous design/operating variables are at the lower/upper limit (Figure 6.8), and the variation in the optimal value of log reduction in the Pareto-optimal front (Figure 6.6) is mainly due to UV dosage.

6.5. Conclusions

This work utilized ANN and GP tools to model UV water disinfection reactors. Both the tools were able to generate models with satisfactory accuracy, and the ANN model performed better in terms of smaller training error. MOO was performed using the developed ANN and GP models, to find the optimal design and operating conditions of UV water disinfection reactors. Selected Pareto-optimal solutions were simulated using CFD software to analyze their validity. The BioGP model performed better in this, and the optimal solutions found using the ANN model are relatively less accurate when compared CFD test results. The Pareto-optimal solutions, obtained using the developed BioGP model, show that larger reactor is preferable for the range of input variables used in this work. Overall, this work demonstrates the application of ANN and GP for modeling UV water disinfection reactors as

well as the use of the developed models for MOO of these reactors. They are useful tools in modeling and optimization of these reactors, and are promising for related processes such as photocatalytic and advanced oxidation reactors. There is a need to employ the developed ANN and GP models for optimization and test the optimal results, as investigated in this study, in order to establish their utility and validity.

Chapter 7

Photocatalytic Degradation: Experiments and Modeling

7.1. Introduction

Photocatalytic degradation of methylene blue (MB) by P25 TiO₂ was performed. The experimental details are provided in Section 7.2. The adsorption-desorption phenomenon of MB on TiO₂ during photocatalytic degradation is discussed in Section 7.3. The effects of choice of light source are presented in Section 7.4. Impacts of TiO₂ concentration on photocatalytic reaction are discussed in Section 7.5. This is followed by analysis of relationship between initial MB concentration and the reaction in Section 7.6. A model was constructed for degradation and desorption in Section 7.7. Findings of this work are summarized in the Conclusions section.

7.2. Experimental methods

Photocatalytic degradation was conducted with different lamps, initial MB and TiO₂ concentrations.

7.2.1. Reagents

Degussa P25 TiO₂ was used as the catalyst. It is polycrystalline and consists of wt. 80% anatase and wt. 20% rutile. Its average particle size is 25 nm and specific surface area is about 50 m²/g. Methylene blue (Aldrich, used as purchased) was used as the target pollutant. It was dissolved in deionised water first to reach concentration of 500 ppm for later use. The water used in this work was deionised by an Elga Micromeg water deioniser.

7.2.2. Experimental procedure

1. MB was added to deionised water to reach concentration of 500 ppm.
2. A given amount of P25 TiO₂ was dissolved in deionised water in a 100 ml beaker. The mixture was ultrasonicated for 15 minutes under room temperature to disperse the solid catalyst particles.
3. Add appropriate amount of 500 ppm MB solution to the TiO₂ suspension to reach the target concentration.

- The mixture was then stirred in darkness in a SGY-II B-Type Multifunctional Photochemistry Reactor (Stonetech Electric Equipment, Nanjing, China, schematic shown in Figure 7.1) for 30 minutes to achieve adsorption-desorption equilibrium before its exposure to the light radiation. The lamp inside the photo-reactor was also turned on for stabilization. Its radiation was shielded from the beaker initially.

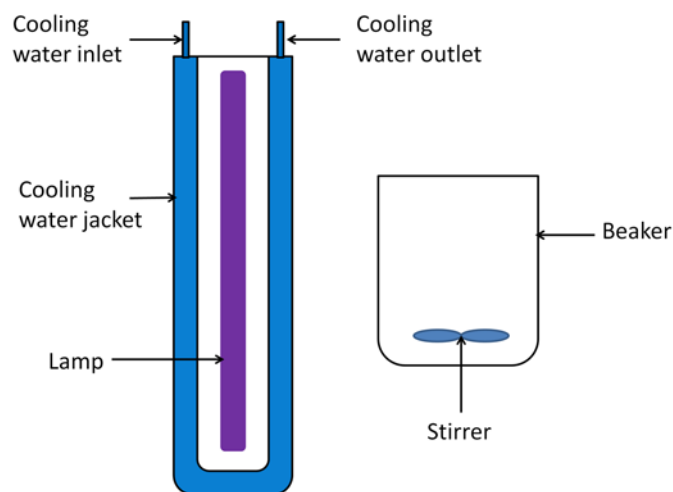


Figure 7.1 Schematic of the photo-reactor

- Remove the light shield and start timing. Samples were taken at fixed time intervals and their light absorbance was measured immediately in a Shimadzu UV1601PC UV-visible spectrophotometer. The difference between the light absorbance at 600 nm of the drawn sample and the slurry at respective TiO_2 concentration was recorded. This wavelength was chosen because the change in light absorbance of the reaction mixture with respect to MB concentration is the most significant at 600 nm while holding the TiO_2 concentration constant.
- The experiment run was stopped when the change in light absorbance of the reaction mixture was minimal. Each experiment run was repeated three times and the average values in light absorbance difference were recorded. The variation in light absorbance difference in the three runs at the same time under the same experimental conditions was within 5%, as shown by the small error bars in Figure 7.2.

Three types of lamps were used: 350 W xenon lamp (labelled as Xe350), 300 W and 500 W mercury lamps (labelled as Hg300 and Hg500 respectively). Different runs of photocatalytic degradation experiment were labelled by TiO_2 concentration – initial MB

concentration. For example, in the 0.2g/L–20ppm run, the TiO_2 concentration is 0.2 g/L while the initial MB concentration is 20 ppm. For this run, 0.01 g of TiO_2 was added into 48 ml of deionised water before addition of 2 ml of 500 ppm MB. Four TiO_2 concentrations were chosen: 0.2 g/L, 0.3 g/L, 0.4 g/L and 0.5 g/L. The initial MB concentrations were 20 ppm, 25 ppm, 30 ppm and 35 ppm.

7.3. Adsorption-desorption equilibrium

Figure 7.2 shows the change in the light absorbance over time of the reaction mixture from the addition of MB (time = -30 min) to start of light radiation (time = 0 min) and end of photocatalytic degradation. When the dye solution is added into the mixture, the dye molecules started to adsorb on the surface of the solid catalyst particles. Little degradation occurred when there was no light radiation. The dye molecules absorb more light when they are free in the solution. Therefore, the adsorption process decreases the light absorbance of the mixture (Region I in Figure 7.2). When the light is turned on, the light absorbance of the mixture at 600 nm increases with time first (Region II) before decreasing to the value around the same as that of the TiO_2 -water slurry at the concentration of 0.2 g/L (Region III). To further study this unusual observation, the sampling time interval for several runs was reduced and the radiation was shielded for several times. Since the lamp requires several minutes to stabilize after turning on, the lamp was shielded to prevent light radiation reaching the slurry, instead of turning it off.

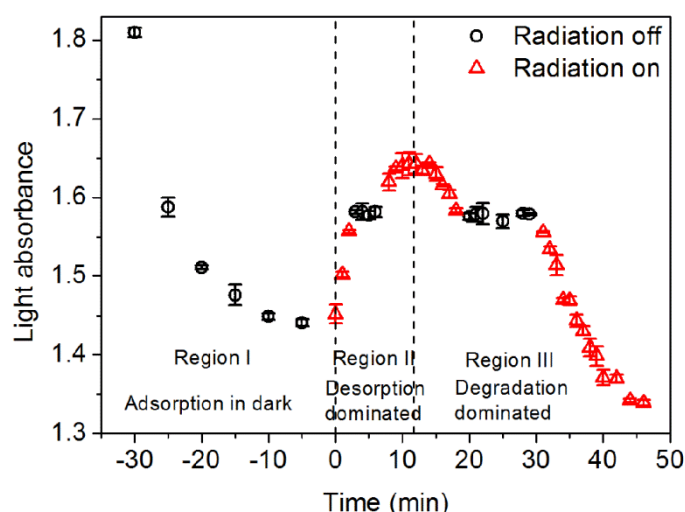


Figure 7.2 Change in light absorbance over time when the radiation was shielded or not for the 0.2g/L–20ppm run; error bars are also shown

It can be observed in Figure 7.2 that, during both increasing and decreasing process of light absorbance, shielding the reaction mixture from light radiation kept the light absorbance of the mixture at almost a constant level. This indicates that both increasing and decreasing of light absorbance is a result of light radiation. Decreasing light absorbance in the later part of the experiment is obviously due to degradation of MB (Region III in Figure 7.2). Since TiO_2 is not able to degrade MB without UV light radiation, shielding off the light stopped the light absorbance from decreasing. Increase in light absorbance at start of light radiation is primarily due to desorption of MB molecules from the surface of the solid catalyst particles. This desorption is probably due to the pH change in the slurry brought by degradation products. Electric charges on both functional groups of MB and surface of TiO_2 were altered, affecting the affinity between MB molecules and the catalyst, shifting the adsorption equilibrium. The concentration of dissolved MB molecules in the solution (i.e. not adsorbed on the surface of the catalyst particles) thus increases, increasing the light absorbance of the mixture. Therefore, when the radiation is shielded off, the light absorbance of the mixture did not fall back to the minimal value at adsorption equilibrium. At the same time, some MB molecules are being degraded by the photocatalytic reaction when the radiation is on, decreasing the light absorbance. The overall light absorbance change is thus a competition between desorption (increase) and degradation (decrease). As the reaction goes on, MB is consumed and the number of MB molecules released from the catalyst surface decreases as less MB molecules are now available for desorption. The light absorbance of the mixture thus starts to decrease after reaching a local maximum until all MB molecules are degraded.

7.4. Effects of different lamps

Three different lamps were used as the light source in this work. Figure 7.3 shows the degradation performance of these lamps with respect to energy consumption. The energy consumption is calculated as the electric energy consumed by the lamps, i.e. product of power of the lamps and irradiation time. The TiO_2 concentration is 0.5 g/L and initial MB concentration is 20 ppm.

It can be observed that degradation using the xenon lamp is the least energy efficient among the three lamps tested (Figure 7.3). This is mainly due to the lower proportion of UV radiation in the xenon lamp emission spectrum than mercury lamps. Therefore, larger amount

of electric energy is “wasted” as light radiation of longer wavelength which is not able to overcome the band gap energy of TiO_2 . When comparing the Hg300 and Hg500 data, it can be observed that the 300 W mercury lamp is able to degrade more MB with the same amount of energy consumed. This is because too many electron-hole pairs are generated when Hg500 lamp is used. Larger fraction of them re-combines and release heat instead of forming hydroxyl radicals when compared to Hg300 lamp, reducing overall efficiency. It can then be deduced that for well-mixed batch reactors, larger number of smaller reactors with lamps of lower power is preferred to smaller number of larger reactors with lamps of higher power, if all other operating conditions are kept constant. For continuous reactors, lower water flow rate and lower UV lamp power are more favourable while keeping UV dosage constant (amount of UV radiation received per unit volume of water). Our previous work has also revealed that lower water flow rate is more favourable for photo water-disinfection reactors in terms of higher UV dosage received for the suspended particles in water [152]. Hence, low water flow rate is preferred in degradation performance. However, lower water flow rate means higher residence time, and hence higher number of reactors required and larger plant size for a certain daily treatment capacity, increasing the capital investment. Therefore, there is a trade-off between capital and operating costs for optimal design.

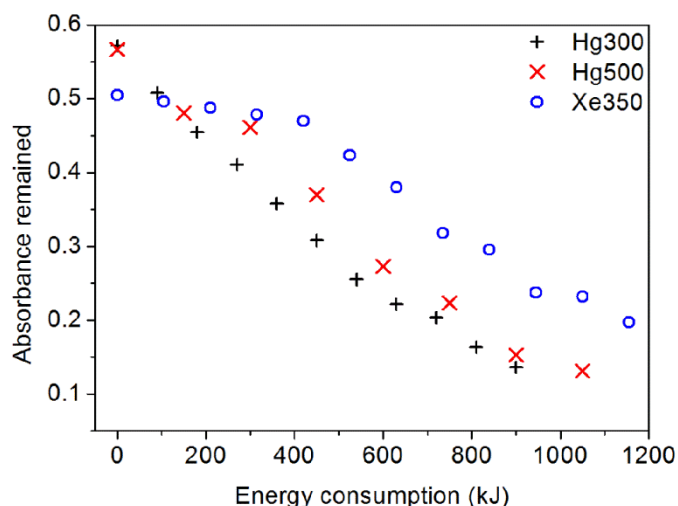


Figure 7.3 Degradation of MB with different lamps: TiO_2 concentration = 0.5 g/L, and initial MB concentration = 20 ppm

7.5. TiO₂ concentration

Photocatalytic degradation of MB was carried out with different TiO₂ and initial MB concentrations. Figure 7.4 shows the degradation performance under a 500 W mercury lamp of different TiO₂ concentrations when the initial MB concentration was varied in the range from 20 to 35 ppm. At the initial MB concentration of 20 ppm, the degradation speed is in this order of TiO₂ concentration: 0.3 g/L > 0.4 g/L > 0.2 g/L > 0.5 g/L (Figure 7.4a). For other initial MB concentrations, this trend is a bit different. For initial MB concentration of 25 ppm and 30 ppm, TiO₂ concentration of 0.3 g/L degrades the dye at the highest speed, followed by 0.4 g/L and 0.5 g/L, and 0.2 g/L is the slowest (Figures 7.4b and 7.4c). When initial MB concentration is 35 ppm, the degradation speed is in this order of TiO₂ concentration: 0.4 g/L > 0.3 g/L > 0.5 g/L > 0.2 g/L (Figure 7.4d). These observations are because, on one hand, higher TiO₂ concentration offers more reaction sites for oxidation of water molecules and production of hydroxyl radicals, thus increases reaction rate. On the other hand, TiO₂ also increases the light absorbance of the mixture, lowering the average light radiation and total amount of photons received by the photocatalyst. The production rate of electron-hole pairs per unit catalyst surface area is lowered and thus hydroxyl radicals produced is less, decreasing the reaction rate. At lower TiO₂ concentration, the increasing effect dominates while at higher TiO₂ concentration, the latter decreasing effect plays a more important role. Therefore, the degradation speed would first increase and then decrease with increasing TiO₂ concentration. The optimal TiO₂ concentration is also different with different initial MB concentration. At lower initial MB concentration, the optimal TiO₂ concentration is lower. 0.3 g/L offers the fastest degradation for initial MB concentration of 20 to 30 ppm. While for 40 ppm, 0.4 g/L is the fastest. This is because at lower MB concentration, the contribution of light absorbance by TiO₂ is relatively higher, i.e. the light absorbance is more sensitive to increase in TiO₂ concentration. Therefore, the decreasing effect of TiO₂ concentration is more predominant.

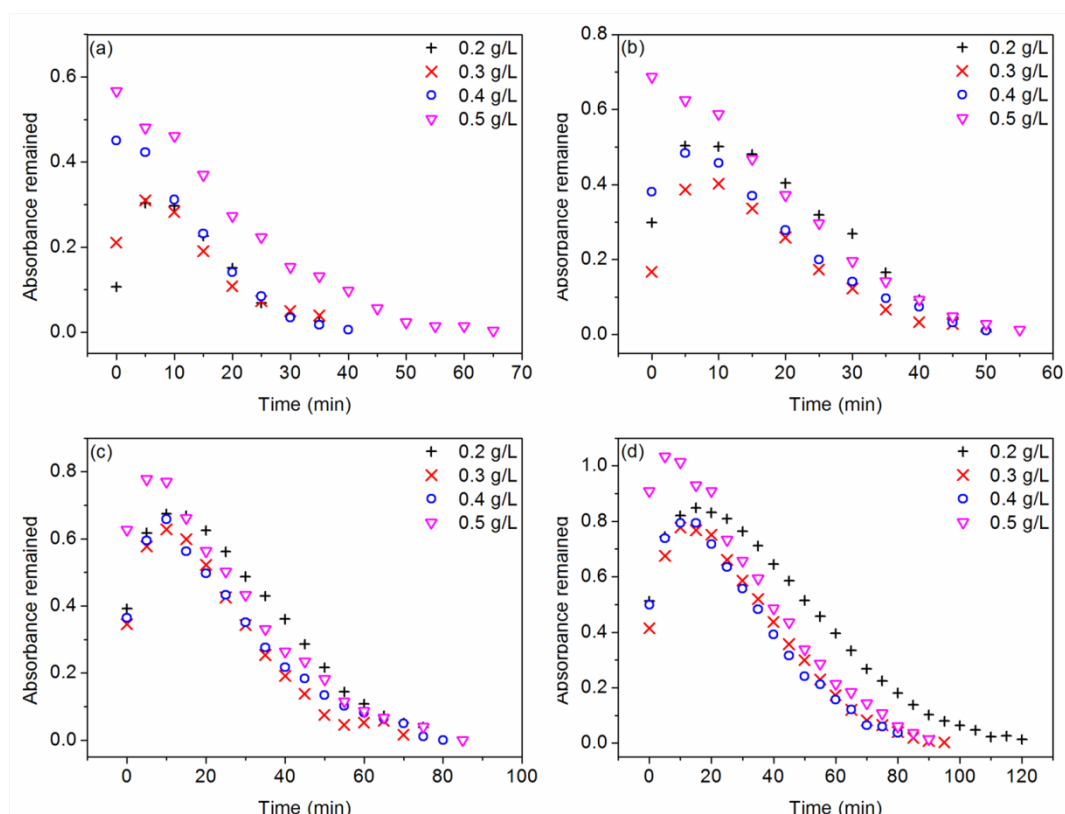


Figure 7.4 Degradation of MB with different TiO_2 concentration, a 500 W mercury lamp, and initial MB concentration of (a) 20 ppm, (b) 25 ppm, (c) 30 ppm, and (d) 35 ppm

It should also be noted that for each initial MB concentration, the increase in the light absorbance during the first few minutes of light radiation becomes smaller and even is not observed with increasing TiO_2 concentration. For example, in Figure 7.4a, the light absorbance keeps decreasing with time for the 0.4g/L–20ppm and 0.5g/L–20ppm runs. The difference between initial light absorbance and highest light absorbance is about 0.2 for the 0.2g/L–20ppm run and about 0.1 for the 0.3g/L–20ppm run. As previously discussed in Section 7.3, the increase in light absorbance during the first few minutes is due to desorption of MB molecules from the surface of the solid catalyst particles. This effect is more predominant for lower TiO_2 concentration as higher TiO_2 concentration offers more sites for adsorption. Hence, the change in adsorption-desorption equilibrium due to light radiation does not effectively increase the number of dissolved MB molecules in the solution when TiO_2 concentration is high enough. On the other hand, the MB molecules in the solution were being degraded all the time, lowering the light absorbance. Therefore, this desorption effect is not observable in terms of increase in light absorbance at higher TiO_2 concentration, such as

the 0.4g/L–20ppm and 0.5g/L–20ppm runs. As initial MB concentration increases, more adsorption sites on the solid catalyst particles are occupied by the MB molecules. When light radiation is on, the amount of desorbed MB molecules is thus higher. Hence, the TiO_2 concentration for which such desorption effect becomes observable increases with increasing initial MB concentration. When the initial MB concentration is 20 ppm (Figure 7.4a), this effect becomes observable when the TiO_2 concentration is 0.3 g/L or lower. In Figure 7.4b (25 ppm), such desorption effect is observed when TiO_2 concentration is 0.4 g/L or lower. When the initial MB concentration is 30 ppm or higher, this desorption effect is observed for all TiO_2 concentrations (Figures 7.4c and 7.4d).

7.6. Initial MB concentration

Figure 7.5 shows the photocatalytic degradation of different initial MB concentration with different TiO_2 concentrations. The time difference decreases with increasing TiO_2 concentration to completely degrade different initial amount of MB. It is more than one hour for TiO_2 concentration of 0.2 g/L (Figure 7.5a) and around 40 minutes for TiO_2 concentration of 0.5 g/L (Figure 7.5d). This is because at higher TiO_2 concentration, more surface adsorption sites are available. The reaction rate is thus less sensitive to the increase in light absorbance brought by increase in initial MB concentration. As the initial MB concentration increases, slope of the degradation curves becomes less steep when approaching the end of the reaction, i.e. it took longer for reaction runs with higher initial MB concentration to degrade for the same amount of light absorbance. This is because the intermediate products of degradation of MB, which have lower light absorbance, would compete with MB for reaction with hydroxyl radicals. At higher initial MB concentration, the intermediates' concentrations are also higher. This lowers the decreasing rate of the mixture's light absorbance.

Another notable observation from Figure 7.5 is that, as initial MB concentration increases, the increase in light absorbance during the first few minutes is different. This is especially obvious for the 0.5 g/L runs. Figure 7.5d shows that no such increase is observed in the 0.5g/L–20ppm and 0.5g/L–25ppm runs, while the increase is quite obvious in the 0.5g/L–30ppm and 0.5g/L–35ppm runs.

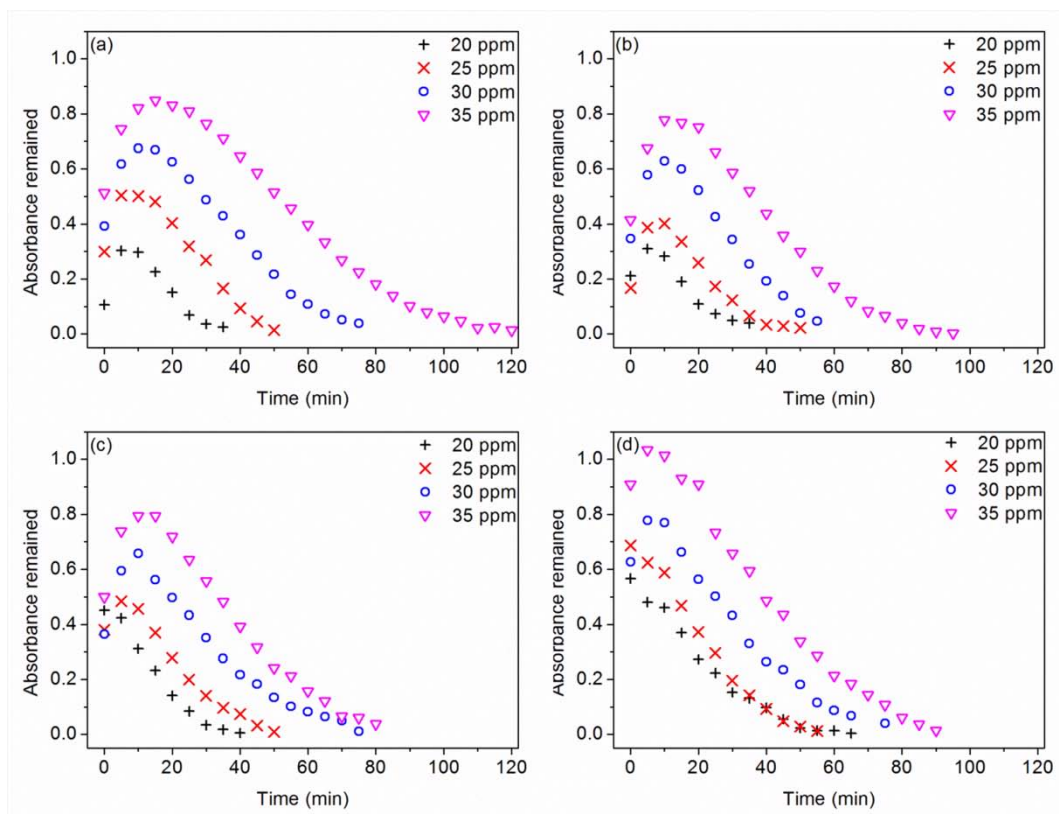


Figure 7.5 Degradation of MB with different initial MB concentration, 500 W mercury lamp and TiO₂ concentration of: (a) 0.2 g/L, (b) 0.3 g/L, (c) 0.4 g/L, and (d) 0.5 g/L

As previously discussed in Section 7.3, the increase in light absorbance is primarily due to desorption of MB from the surface of the solid catalyst particles. Section 7.5 has also discussed about this phenomenon at higher TiO₂ concentration and lower MB concentration. When the initial MB concentration increases, the change in adsorption-desorption equilibrium would increase concentration of dissolved MB in the solution. Hence, the light absorbance increases. On the other hand, increase in initial MB concentration also makes decrease in light absorbance faster as degradation reaction rate increases with increasing MB concentration. Therefore, this partially offsets the desorption effect when compared to the increase in light absorbance during the first few minutes of 0.5g/L–30ppm and 0.5g/L–35ppm runs. The magnitude of this increase in light absorbance is larger in the 0.5g/L–30ppm run (about 0.15) than in the 0.5g/L–35ppm run (about 0.11). As the TiO₂ concentration decreases, number of vacant adsorption sites decreases. Hence, when there is a shift of equilibrium to the desorption side, the desorption effect is more observable at lower TiO₂ concentration. The initial MB concentration for which such effect becomes observable thus decreases with

decreasing TiO₂ concentration. When the TiO₂ concentration is 0.4 g/L, this desorption effect is observed when the initial MB concentration is 25 ppm or higher (Figure 7.5c). When the TiO₂ concentration drops to 0.3 g/L and 0.2 g/L, this desorption effect is observed for all initial MB concentrations (Figures 7.5a and 7.5b).

7.7. Modelling of degradation

As discussed in the above sections, the change in light absorbance of the mixture can be attributed to two processes: desorption increases light absorbance while degradation decreases it. Therefore, to model the change in light absorbance, both processes have to be considered.

The degradation reaction can usually be fitted into Equation 2-8. As the MB concentration is low in this work (35 ppm maximum), it can further be simplified since $KC \ll 1$.

$$-r = \frac{dC}{dt} = \frac{kKC}{1+KC} \approx kKC \quad \text{Equation 7-1}$$

The L-H model is based on the assumption that the adsorption equilibrium is established much faster than reaction. From the experimental observation, it was found that the adsorption equilibrium is continuously shifting towards the desorption side when light radiation is on, i.e. the proportion of adsorbed MB is always decreasing (Section 7.3). Therefore, the L-H model is no longer applicable here. Hence, for simplicity, it is assumed that the net desorption rate is first order with respect to concentration of MB adsorbed on the surface of the catalyst, thus

$$\frac{dC_a}{dt} = -k_2 C_a \quad \text{Equation 7-2}$$

where C_a is the concentration of MB adsorbed on the surface of the catalyst (in mass per unit mass of catalyst), and k_2 is the desorption rate constant (in hour⁻¹). Therefore, the concentration of MB adsorbed on the catalyst surface is

$$C_a = C_{a0} \exp(-k_2 t) \quad \text{Equation 7-3}$$

where C_{a0} is the concentration of adsorbed MB at the start of light radiation.

The change in the concentration of dissolved MB in the solution because of both degradation and desorption processes is

$$\frac{dC_f}{dt} = -r - \frac{dC_a}{dt} = \frac{1}{V}[-k_1 C_f V + k_2 C_a C_s V] \quad \text{Equation 7-4}$$

Here, r is the degradation reaction rate, C_f is the concentration of dissolved MB in the solution (in g/L), k_1 is the degradation reaction rate constant (in hour^{-1}), V is the total solution volume (in L) and C_s is the catalyst concentration (in g/L). Solving Equation 7-4:

$$C_f = \frac{k_2}{k_1 - k_2} C_s C_{a0} \exp(-k_2 t) + (C_{f0} - \frac{k_2 C_s C_{a0}}{k_1 - k_2}) \exp(-k_1 t) \quad \text{Equation 7-5}$$

where C_{f0} is the concentration of dissolved MB in the solution at the start of light radiation. It should be noted that both k_1 and k_2 are dependent on light radiation received by the catalyst. Both TiO_2 and MB affect light radiation received by the catalyst, and so k_1 and k_2 are dependent on their concentrations.

Assume that the light absorbance (X) is linear with respect to both C_a and C_f :

$$\begin{aligned} X &= \alpha C_f + \beta C_a C_s = \left(\frac{\alpha k_2}{k_1 - k_2} C_s + \beta C_s \right) C_{a0} \exp(-k_2 t) + \alpha \left(C_{f0} - \frac{k_2 C_s C_{a0}}{k_1 - k_2} \right) \exp(-k_1 t) \\ &= m \exp(-k_1 t) + n \exp(-k_2 t) \end{aligned}$$

Equation 7-6

where

$$m = \alpha \left(C_{f0} - \frac{k_2 C_s C_{a0}}{k_1 - k_2} \right) \quad n = \left(\frac{\alpha k_2}{k_1 - k_2} + \beta \right) C_{a0} C_s$$

This assumption about light absorbance and MB concentration can be partially validated as the light absorbance changes nearly linearly with respect to total methylene concentration, as shown in Figure 7.6.

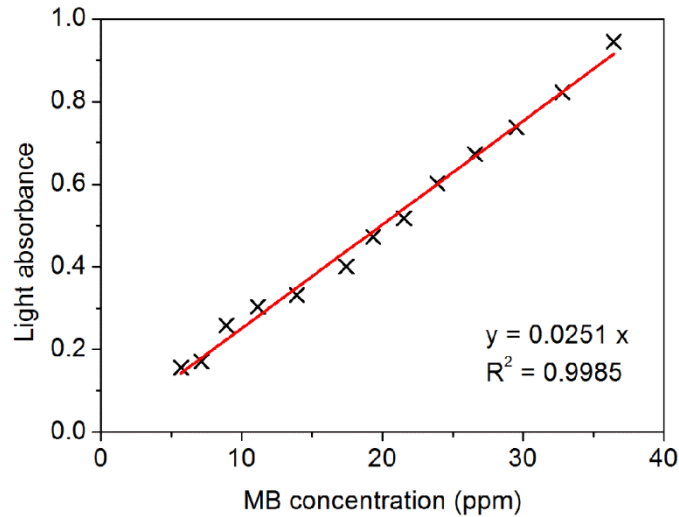


Figure 7.6 Variation of light absorbance of 0.5 g/L TiO₂ with MB concentration

The light absorbance curves in Figure 7.4 indicate that the free MB concentration first increases and then decreases over time for most of the runs; hence, the desorption rate is higher than degradation rate under most conditions at the beginning of light radiation. Therefore, $k_2 > k_1$, and m is positive. For the same reason, n has to be negative in order to fit the shape of the light absorbance curve with respect to time.

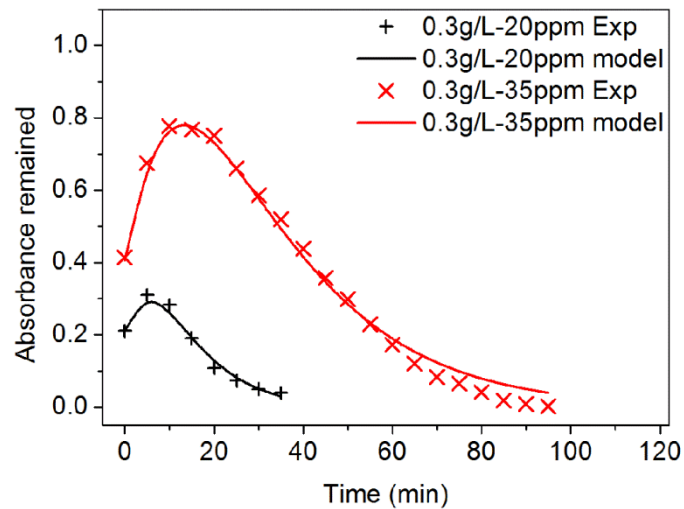


Figure 7.7 Light absorbance for selected runs and the model predictions

Measured light absorbance data from each run of all the 16 photocatalytic degradation runs using the 500 W mercury lamp were fitted into Equation 7-6. The estimates of m , n , k_1 and k_2 from this modelling for all runs are summarized in Table 7.1. Slope and R^2 in this table

refer to the gradients and the coefficients of determination for the regression line passing through the origin of the plots of fitted data versus actual light absorbance (i.e., parity plots) for each run. All slopes and R^2 are close to unity, indicating a good fitting of the experimental data into Equation 7-6. Figure 7.7 shows the modeling results for selected runs, which were also close to the experimental results.

Table 7.1 Constants for photocatalytic degradation and desorption

Run No.	m	n	k_1 (hr ⁻¹)	k_2 (hr ⁻¹)	Slope	R^2	Number of data points
0.2g/L-20ppm	2.152	-2.046	6.905	10.036	1.0190	0.9844	8
0.2g/L-25ppm	3.202	-2.903	4.489	6.499	0.9969	0.9697	11
0.2g/L-30ppm	2.743	-2.351	2.826	4.997	0.9992	0.9854	17
0.2g/L-35ppm	4.546	-4.033	2.189	3.343	1.0021	0.9894	25
0.3g/L-20ppm	2.201	-1.990	6.925	9.211	0.9929	0.9900	8
0.3g/L-25ppm	2.959	-2.792	5.619	7.800	0.9976	0.9949	11
0.3g/L-30ppm	2.917	-2.571	3.782	6.252	1.0048	0.9906	12
0.3g/L-35ppm	4.866	-4.460	2.965	4.267	0.9939	0.9908	20
0.4g/L-20ppm	2.347	-1.896	6.941	9.033	0.9979	0.9956	9
0.4g/L-25ppm	2.986	-2.606	5.306	7.265	1.0068	0.9976	11
0.4g/L-30ppm	2.552	-2.188	3.429	6.018	1.0074	0.9960	16
0.4g/L-35ppm	4.926	-4.427	3.168	4.491	0.9963	0.9965	17
0.5g/L-20ppm	1.701	-1.134	4.407	6.970	1.0222	0.9903	14
0.5g/L-25ppm	2.910	-2.223	4.654	6.455	1.0097	0.9923	12
0.5g/L-30ppm	4.793	-4.166	3.664	4.927	1.0085	0.9946	15
0.5g/L-35ppm	5.085	-4.176	2.818	3.957	0.9979	0.9946	19

Figures 7.8 and 7.9 are, respectively, the plots of k_1 and k_2 at different TiO_2 and initial MB concentrations. It can be observed from Figures 7.8a and 7.9a that both degradation rate (k_1) and desorption rate (k_2) constants decrease with increasing initial MB concentration. This is because higher MB concentration absorbs more UV radiation, thus lowering the overall UV radiation received by the solid catalyst particles, effectively slowing the production rate of hydroxyl radicals and the degradation reaction. This observation is consistent with the research work of Li et al. [18]. Since desorption is also related to the UV radiation, blocking of UV radiation by higher MB concentration decreases desorption rate constant. Figure 7.8b shows that the degradation rate constant first increases and then decreases with catalyst concentration, at higher initial MB concentrations (25 ppm and above). On the other hand, when the initial MB concentration is 20 ppm, the degradation rate constant is almost constant when the TiO_2 concentration is below 0.4 g/L and then decreases at higher TiO_2 concentration. This is because higher TiO_2 concentration provides more sites for adsorption of water molecules and hence more hydroxyl radicals are produced, increasing the degradation rate. On the other hand, higher TiO_2 concentration also absorbs more UV radiation, decreasing the overall photon efficiency and hence decreasing the degradation rate. As discussed in Section 7.5, the increasing effect is more dominant at lower TiO_2 concentration while the decreasing effect is more dominant at higher TiO_2 concentration.

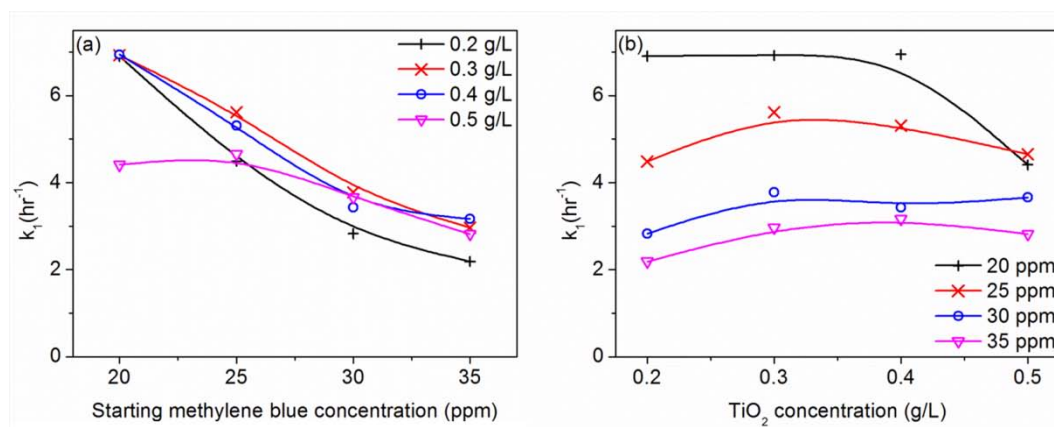


Figure 7.8 Degradation rate constants at different TiO_2 and initial MB concentrations

The desorption rate constant also decreases with increasing initial MB concentration (Figure 7.9a). The rate of change of solid catalyst surface property increases with increasing TiO_2 concentration. On the other hand, higher TiO_2 concentration provides more sites for adsorption, shifting the equilibrium to the adsorption side, effectively lowering the desorption

rate. This decreasing effect is most observable when initial MB concentration is 20 ppm, due to the fact that majority of the MB molecules are adsorbed on the surface of the catalyst at this low MB concentration. More UV radiation absorbed by higher TiO_2 concentration also contributes to lower the desorption rate constant.

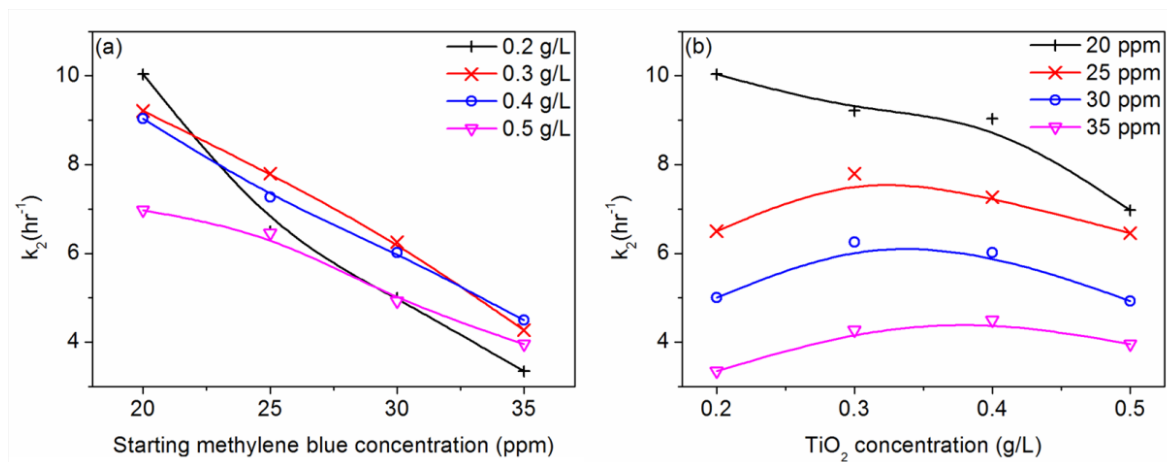


Figure 7.9 Desorption rate constants at different TiO_2 and initial MB concentrations

It can be concluded from experimental data and modelling that both degradation and desorption of MB by TiO_2 fit into a pseudo-first-order model well. High MB concentration suppresses both desorption and degradation, and the effect of TiO_2 concentration is more complicated. Increasing TiO_2 concentration enhances both desorption and degradation at lower values. Further increasing it reduces reaction rate constants for both processes. Both these are mainly due to the change in light radiation received by the catalyst under different experimental conditions.

7.8. Conclusions

Photocatalytic degradation of MB by TiO_2 was studied under different conditions. Desorption of MB molecules from catalyst surface at the start of UV radiation was observed; it is probably due to change in the surface property of the solid catalyst. Lamp with lower power was found to be more energy efficient. Experimental data show that concentration of TiO_2 and initial MB concentration have complex impact on the reaction rate. Experimental data on both net desorption and degradation of MB are fitted well by a pseudo-first-order reaction model. MB has negative impact on both degradation and desorption. Increasing TiO_2 concentration first enhances both processes and then suppresses them.

The design and operational principles from photo-reactors can be applied to photocatalytic reactors since most of the photocatalytic degradation occurs near the surface of the catalyst particles. The UV fluence received by the photocatalyst is also an important indicator for good reactor design, similar to the UV fluence received by the microorganism particles in the photo-reactors. The parameters in Table 7.1 can be integrated into the UV fluence response equations if TURF is applied to model photocatalytic reactors.

Chapter 8

Conclusions and Recommendations

8.1. Conclusions

Photo and photocatalytic water treatment technologies are promising substitutes for conventional methods such as chlorination. The broad objective of this doctoral research is to establish models relating design and operating variables to performance of photo and photocatalytic reactors, by both computer simulation and experimental work. For this, a new simulation methodology was developed for simulating photo water-disinfection reactors via CFD software. It was applied to simulate several photo water-disinfection reactors with different dimensions, water flow rate, lamp arrangement and lamp power. The simulation data was then used to train ANN and GP models to describe the complex relationship between reactor performance and design and operating variables. The obtained models and MOO tool were used for two-objective optimization, and several Pareto-optimal solutions obtained were simulated in the CFD software to test the generalization ability of ANN and GP models over new input sets. Photocatalytic degradation of methylene blue by TiO_2 was performed under different experimental conditions. Reaction model was constructed, and the relationship between reaction conditions and reaction rate constants was investigated.

The conclusions drawn from this thesis work are summarized below.

- Photo-disinfection reactors can be simulated using the TURF methodology in three consecutive steps: establishment of UV fluence rate distribution, construction of water flow profile and calculation of microorganism log reduction passing through the reactors. The TURF methodology offers simulation results close to both experimental data and predictions by SURF methodology used in earlier studies; furthermore, it significantly reduces calculation time for simulations.
- The size and shape of microorganism particles did not have an observable impact on the UV fluence received by microorganisms in photo water-disinfection reactors. Water flow rate, reactor size and shape have complex effect on reactor performance. Low water flow rate and large reactor volume generally favor better reactor performance due to higher particle residence time. It was found that reactor

performance was correlated to the particle movement in radial direction inside the single-lamp photo water-disinfection reactors.

- For photo water-disinfection reactors with multiple lamps, parallel reactors are more efficient than perpendicular reactors. Reactors with lamps directly below water inlet and outlet enhance reactor performance by retaining the particles inside the reactors for a longer time. Higher water flow rate diminishes this “barrier” effect, lowering log reduction for the same UV dosage. Reactors and operating conditions that provide higher average UV fluence rate and lower normalized standard deviation of particle residence time, result in better reactor performance in terms of higher log reduction under constant UV dosage.
- Both ANN and GP models trained by the simulation data of photo water-disinfection reactors were able to describe the complex relationship between reactor performance and design and operating variables. The ANN model performed better in terms of smaller modeling error. MOO was performed using the developed ANN and GP models, to find the optimal design and operating conditions of photo water-disinfection reactors. Selected Pareto-optimal solutions were simulated using CFD software to analyze the validity of ANN and GP models and also optimal results obtained using them. The BioGP model performed better in this aspect, and the optimal solutions found using the ANN model are relatively less accurate when compared with CFD test results. The Pareto-optimal solutions, obtained using the developed BioGP model, show that larger reactor and lower water flow rate are preferable for the range of input variables used in this work, which is consistent with the findings above.
- In photocatalytic degradation of methylene blue by TiO_2 , mercury lamp with lower power was found to be more energy efficient. The overall light absorbance of the reaction slurry increased at starting phase of light radiation, due to desorption of methylene blue molecules from the catalyst surface, probably a result of change in the surface property of the solid catalyst by light radiation. Analysis of results showed that both net desorption and degradation of methylene blue data can be modelled by a pseudo first-order reaction model. The reaction rate constants for both desorption and degradation decreased with increasing initial methylene blue concentration due to

higher light absorbance by the slurry and lower average light radiation received by the catalyst. The increasing TiO_2 concentration first enhanced desorption and degradation, and then suppressed both processes.

8.2. Recommendations for future work

This thesis has demonstrated the accuracy of the TURF simulation methodology for photo water-disinfection reactors. The complex relationship between reactor performance and design and operating parameters can be described by ANN and GP models. Desorption and degradation of methylene blue in TiO_2 slurry were analyzed. A number of recommendations for follow-up work are outlined below.

- Currently, all the reactors simulated in this thesis are lab-scale in size. In principle, TURF methodology developed in this work can be applied to simulate industrial-scale reactors because the characterizing parameters such as Reynolds number for industrial reactors are similar to those for the lab-scale reactors. However, validation of this is desirable and yet to be done; this requires design and operating data of such reactors as well measurements on their performance. An attempt was made in this direction as part of the present research but it was not successful. The operating conditions and log reduction of microorganisms were available, but complete design details of the reactors were lacking. In addition, the industrial data were concentrated around a particular water flow rate.
- The relationship between reactor performance and design and operating variables has been analyzed in Chapters 4 and 5. However, a single quantity, which combines the effects of all these variables, is still not found yet, and this requires further research. Such a quantity for photocatalytic reactors has been explored. Akyol and Bayramoglu proposed that the catalyst surface area per unit reactor volume could be a good indicator for photocatalytic reactor performance [68].
- All the photo water-disinfection reactors with multiple-lamps simulated in Chapter 5 are of the same size. This thesis has shown that the relationship between reactor performance and design and operating variables is highly non-linear. The reactor size may affect optimal lamp arrangement under different operating conditions, and needs to be investigated.

- In Chapter 6, it is shown that ANN performs better in modeling photo water-disinfection reactors in terms of smaller modeling error while GP performs better in generalization ability. Therefore, modification in modeling algorithm to combine the merits of both modeling tools is a promising research area. It seems that researchers have been focused in comparing modeling accuracy of different modeling tools instead of combining their merits [46, 51-54].
- In Chapter 7, desorption and degradation of methylene blue by TiO_2 in a batch reactor was analyzed. One possible follow-up work is the experimental and modeling study of this photocatalytic process in continuous reactors. The light absorbance of the reaction mixture increases at start of light radiation, as discussed in Section 7.3. Therefore, continuous reactors should be designed to allow sufficient residence time for the reaction mixture to reach degradation dominated region (refer to Figure 7.2).

References

1. Wolfe, R.L., Ultraviolet disinfection of potable water: Current technology and research needs. *Environmental Science and Technology*, 1990. **24**(6): p. 768-773.
2. Malato, S., et al., Photocatalytic decontamination and disinfection of water with solar collectors. *Catalysis Today*, 2007. **122**(1-2): p. 137-149.
3. Ma, J., et al., Enhanced inactivation of bacteria with silver-modified mesoporous TiO₂ under weak ultraviolet irradiation. *Microporous and Mesoporous Materials*, 2011. **144**(1-3): p. 97-104.
4. Ducoste, J.J., D. Liu, and K. Linden, Alternative approaches to modeling fluence distribution and microbial inactivation in ultraviolet reactors: Lagrangian versus Eulerian. *Journal of Environmental Engineering*, 2005. **131**(10): p. 1393-1403.
5. Blatchley-III, E.R., Numerical modelling of UV intensity: Application to collimated-beam reactors and continuous-flow systems. *Water Research*, 1997. **31**(9): p. 2205-2218.
6. Suidan, M.T. and B.F. Severin, Light intensity models for annular UV disinfection reactors. *AIChE Journal*, 1986. **32**(11): p. 1902-1909.
7. Naunovic, Z., K.G. Pennell, and E.R. Blatchley-III, Development and performance of a fluence rate distribution model for a cylindrical excimer lamp. *Environmental Science and Technology*, 2008. **42**(5): p. 1605-1614.
8. Shih, T.-H., et al., A new k- ϵ Eddy viscosity model for high Reynolds number turbulent flows. *Computers & Fluids*, 1995. **24**(3): p. 227-238.
9. Elyasi, S. and F. Taghipour, Simulation of UV photoreactor for water disinfection in Eulerian framework. *Chemical Engineering Science*, 2006. **61**(14): p. 4741-4749.
10. Safikhani, H., et al., Modeling and multi-objective optimization of square cyclones using CFD and neural networks. *Chemical Engineering Research and Design*, 2011. **89**: p. 301-309.

-
11. WHO and UNICEF, Progress in Drinking-water and Sanitation: special focus on sanitation. 2008, New York; Geneva: World Health Organization and United Nations Children's Fund Joint Monitoring Programme for Water Supply and Sanitation.
 12. Watkins, K., Human Development Report 2006. 2006, New York: The United Nations Development Programme, Palgrave Macmillan.
 13. Macedonio, F., et al., Efficient technologies for worldwide clean water supply. *Chemical Engineering and Processing*, 2012. **51**: p. 2-17.
 14. Rideal, S., Disinfection and Disinfectants: together with an account of the chemical substances used as antiseptics and preservatives. 1895, the University of California: C. Griffin.
 15. Hijnen, W.A.M., E.F. Beerendonk, and G.J. Medema, Inactivation credit of UV radiation for viruses, bacteria and protozoan (oo)cysts in water: A review. *Water Research*, 2006. **40**(1): p. 3-22.
 16. Malato, S., et al., Decontamination and disinfection of water by solar photocatalysis: Recent overview and trends. *Catalysis Today*, 2009. **147**(1): p. 1-59.
 17. Pan, J.H., et al., Porous photocatalysts for advanced water purifications. *Journal of Materials Chemistry*, 2010. **20**(22): p. 4512-4528.
 18. Li, Y., et al., Kinetic Study and Model of the Photocatalytic Degradation of Rhodamine B (RhB) by a TiO₂-Coated Activated Carbon Catalyst: Effects of Initial RhB Content, Light Intensity and TiO₂ Content in the Catalyst. *Chemical Engineering Journal*, 2008. **142**(2): p. 147-155.
 19. Li Puma, G., Dimensionless Analysis of Photocatalytic Reactors Using Suspended Solid Photocatalysts. *Chemical Engineering Research and Design*, 2005. **83**(7): p. 820-826.
 20. Sozzi, D.A. and F. Taghipour, Computational and experimental study of annular photo-reactor hydrodynamics. *International Journal of Heat and Fluid Flow*, 2006. **27**(6): p. 1043-1053.

21. Sozzi, D.A. and F. Taghipour, UV reactor performance modeling by Eulerian and Lagrangian methods. *Environmental Science and Technology*, 2006. **40**(5): p. 1609-1615.
22. Lyn, D.A., K. Chiu, and E.R. Blatchley-III, Numerical modeling of flow and disinfection in UV disinfection channels. *Journal of Environmental Engineering*, 1999. **125**(1): p. 17-26.
23. Li Puma, G., J.N. Khor, and A. Brucato, Modelling of an Annular Photocatalytic Reactor for Water Purification: Oxidation of Pesticides. *Environmental Science and Technology*, 2004. **38**(13): p. 3737-3745.
24. Blatchley-III, E.R., W.L. Wood, and P. Schuerch, UV pilot testing, intensity distribution and hydrodynamics. *Journal of Environmental Engineering*, 1995. **121**(3): p. 258-262.
25. Bolton, J.R., Calculation of Ultraviolet fluence rate distributions in an annular reactor: Significance of refraction and reflection. *Water Research*, 2000. **34**(13): p. 3315-3324.
26. Duran, J.E., F. Taghipour, and M. Mohseni, Irradiance modeling in annular photoreactors using the finite-volume method. *Journal of Photochemistry and Photobiology A: Chemistry*, 2010. **215**(1): p. 81-89.
27. Batchelor, G.K., *An Introduction to Fluid Dynamics*. 1967, Cambridge: Cambridge University Press.
28. Elyasi, S. and F. Taghipour, General method of simulating radiation fields using measured boundary values. *Chemical Engineering Science*, 2010. **65**(20): p. 5573-5581.
29. Chen, J., B. Deng, and C.N. Kim, Computational fluid dynamics (CFD) modeling of UV disinfection in a closed-conduit reactor. *Chemical Engineering Science*, 2011. **66**(21): p. 4983-4990.
30. Cabrera, M.I., O.M. Alfano, and A.E. Cassano, Absorption and Scattering Coefficients of Titanium Dioxide Particulate Suspensions in Water. *Journal of Physical Chemistry B*, 1996. **100**(51): p. 20043-20050.

-
31. Boyjoo, Y., M. Ang, and V. Pareek, Light intensity distribution in multi-lamp photocatalytic reactors. *Chemical Engineering Science*, 2013. **93**: p. 11-21.
 32. Ballari, M.d.I.M., O.M. Alfano, and A.E. Cassano, Mass transfer limitations in slurry photocatalytic reactors: Experimental validation. *Chemical Engineering Science*, 2010. **65**(17): p. 4931-4942.
 33. Alpert, S.M., D.R.U. Knappe, and J.J. Ducoste, Modeling the UV/hydrogen peroxide advanced oxidation process using computational fluid dynamics. *Water Research*, 2010. **44**(6): p. 1797-1808.
 34. Chen, J.-q., et al., Photocatalytic mineralization of dimethoate in aqueous solutions using TiO₂: Parameters and by-products analysis. *Desalination*, 2010. **258**(1): p. 28-33.
 35. Chiu, K., et al., Integrated UV disinfection model based on particle tracking. *Journal of Environmental Engineering*, 1999. **125**(1): p. 459-469.
 36. Liu, D., et al., Numerical simulation of UV disinfection reactors: Evaluation of alternative turbulence models. *Applied Mathematical Modelling*, 2007. **31**: p. 1753-1769.
 37. ANSYS, ANSYS 13.0 Help. 2010.
 38. Fenner, R.A. and K. Komvuschara, A new kinetic model for ultraviolet disinfection of greywater. *Journal of Environmental Engineering*, 2004. **131**(6): p. 850-864.
 39. Hofman-Caris, R.C.H.M., et al., Prediction of advanced oxidation performance in various pilot UV/H₂O₂ reactor systems with MP- and LP- and DBD-UV lamps. *Chemical Engineering Journal*, 2012. **210**: p. 520-528.
 40. Launder, B.E. and D.B. Spalding, *Lectures in Mathematical Models of Turbulence*. 1972, London, New York: Academic Press.
 41. Cartwright, H. and S. Curteanu, *Neural Networks Applied in Chemistry. II. Neuro-Evolutionary Techniques in Process Modeling and Optimization*. *Industrial and Engineering Chemistry Research*, 2013. **52**(36): p. 12673-12688.

42. Pettersson, F., N. Chakraborti, and H. Saxén, A genetic algorithms based multi-objective neural net applied to noisy blast furnace data. *Applied Soft Computing*, 2007. **7**(1): p. 387-397.
43. Nath, K. and D. Das, Modeling and optimization of fermentative hydrogen production. *Bioresource Technology*, 2011. **102**(18): p. 8569-8581.
44. Safikhani, H., A. Hajiloo, and M.A. Ranjbar, Modeling and multi-objective optimization of cyclone separators using CFD and genetic algorithms. *Computers and Chemical Engineering*, 2011. **35**: p. 1064-1071.
45. Elsayed, K. and C. Lacor, CFD modeling and multi-objective optimization of cyclone geometry using desirability function, artificial neural networks and genetic algorithms. *Applied Mathematical Modelling*, 2013. **37**(8): p. 5680-5704.
46. Giri, B.K., et al., Genetic programming through bi-objective genetic algorithms with a study of a simulated moving bed process involving multiple objectives. *Applied Soft Computing*, 2012. **13**(5): p. 2613-2623.
47. Di Pasquale, N., et al., Identification of nucleation rate parameters with MD and validation of the CFD model for polymer particle precipitation *Chemical Engineering Research and Design*, 2013: p. Accepted Manuscript.
48. Soleimani, R., et al., Experimental investigation, modeling and optimization of membrane separation using artificial neural network and multi-objective optimization using genetic algorithm. *Chemical Engineering Research and Design*, 2013. **91**(5): p. 883-903.
49. Moral, H., A. Aksoy, and C.F. Gokcay, Modeling of the activated sludge process by using artificial neural networks with automated architecture screening. *Computers and Chemical Engineering*, 2008. **32**(10): p. 2471-2478.
50. Ghavipour, M., et al., Experimental study of natural gas hydrates and a novel use of neural network to predict hydrate formation conditions. *Chemical Engineering Research and Design*, 2013. **91**(2): p. 264-273.

-
51. Shiri, J., et al., Predicting groundwater level fluctuations with meteorological effect implications—A comparative study among soft computing techniques *Computers & Geosciences*, 2013. **56**: p. 32-44.
 52. Kisi, O., J. Shiri, and M. Tombul, Modeling rainfall-runoff process using soft computing techniques. *Computers & Geosciences*, 2013. **51**: p. 108-117.
 53. Çelekli, A., H. Bozkurt, and F. Geyik, Use of artificial neural networks and genetic algorithms for prediction of sorption of an azo-metal complex dye onto lentil straw. *Bioresource Technology*, 2013. **129**: p. 396-401.
 54. Güres, S., et al., Application of artificial neural networks (ANNs) and genetic programming (GP) for prediction of drug release from solid lipid matrices. *International Journal of Pharmaceutics*, 2012. **436**(1-2): p. 877-879.
 55. Caliman, F.A., et al., Neural Networks and Genetic Algorithms Optimization of the Photocatalytic Degradation of Alcian Blue 8GX. *Journal of Advanced Oxidation Technologies*, 2008. **11**(2): p. 1-11.
 56. Dutta, S., et al., Development of an artificial neural network model for adsorption and photocatalysis of reactive dye on TiO₂ surface. *Expert Systems with Applications*, 2010. **37**(12): p. 8634-8638.
 57. Fahmi, I. and S. Cremaschi, Process synthesis of biodiesel production plant using artificial neural networks as the surrogate models. *Computers and Chemical Engineering*, 2012. **46**: p. 105-123.
 58. Song, Z., B.T. Murray, and B. Sammakia, Airflow and temperature distribution optimization in data centers using artificial neural networks. *International Journal of Heat and Mass Transfer*, 2013. **64**: p. 80-90.
 59. Xiong, Z., et al., Synthesis of mesoporous anatase TiO₂ with a combined template method and photocatalysis. *Crystal Engineering Communications*, 2010. **12**: p. 3455-3457.

60. Friedler, E. and Y. Gilboa, Performance of UV disinfection and the microbial quality of greywater effluent along a reuse system for toilet flushing. *Science of the Total Environment*, 2010. **208**(9): p. 2109-2117.
61. Sattler, C., et al., Solar Photocatalytic Water Detoxification of Paper Mill Effluents. *Energy*, 2004. **29**(5-6): p. 835-843.
62. Fox, M.A. and M.T. Dulay, Heterogeneous photocatalysis. *Chemical Reviews*, 1993. **93**(1): p. 341-357.
63. Hoffmann, M.R., et al., Environmental applications of semiconductor photocatalysis. *Chemical Reviews*, 1995. **95**(1): p. 69-96.
64. Li, Q., et al., Antimicrobial nanomaterials for water disinfection and microbial control: Potential applications and implications. *Water Research*, 2008. **42**(18): p. 4591-4602.
65. Fujishima, A., X. Zhang, and D.A. Tryk, TiO₂ photocatalysis and related surface phenomena. *Surface Science Reports*, 2008. **63**(12): p. 515-582.
66. Chuang, H.-Y. and D.-H. Chen, Fabrication and photocatalytic activities in visible and UV light regions of Ag@TiO₂ and NiAg@TiO₂ nanoparticles. *Nanotechnology*, 2009. **20**(10): p. 105704-105713.
67. Hofstadler, K., et al., New Reactor Design for Photocatalytic Wastewater Treatment with TiO₂ Immobilized on Fused-Silica Fibers, Photomineralization of 4-Chlorophenol. *Environmental Science and Technology*, 1994. **28**(4): p. 670-674.
68. Akyol, A. and M. Bayramoglu, Photocatalytic performance of ZnO coated tubular reactor. *Journal of Hazardous Materials*, 2010. **180**(1-3): p. 466-473.
69. Dijkstra, M.F.J., et al., Experimental Comparison of Three Reactor Designs for Photocatalytic Water Purification. *Chemical Engineering Science*, 2001. **56**(2): p. 547-555.
70. Ohno, T., et al., Morphology of a TiO₂ Photocatalyst (Degussa, P-25) Consisting of Anatase and Rutile Crystalline Phases. *Journal of Catalysis*, 2001. **203**(1): p. 82-86.

-
71. Chauhan, R., A. Kumar, and R.P. Chaudhary, Photocatalytic degradation of methylene blue with Cu doped ZnS nanoparticles. *Journal of Luminescence*, 2014. **145**: p. 6-12.
72. Kang, Q., et al., A ternary hybrid CdS/Pt-TiO₂ nanotube structure for photoelectrocatalytic bactericidal effects on Escherichia Coli. *Biomaterials*, 2010. **31**(12): p. 3317-3326.
73. Lv, H., et al., Synthesis of graphene oxide-BiPO₄ composites with enhanced photocatalytic properties. *Applied Surface Science*, 2013. **284**: p. 308-314.
74. Ahmad, M., et al., Graphene-Ag/ZnO nanocomposites as high performance photocatalysts under visible light irradiation. *Journal of Alloys and Compounds*, 2013. **577**: p. 717-727.
75. Akhavan, O. and E. Ghaderi, Self-accumulated Ag nanoparticles on mesoporous TiO₂ thin film with high bactericidal activities. *Surface and Coatings Technology*, 2010. **204**(21-22): p. 3676-3683.
76. Akly, C., P.A. Chadik, and D.W. Mazyck, Photocatalysis of gas-phase toluene using silica-titania composites: Performance of a novel catalyst immobilization technique suitable for large-scale applications. *Applied Catalysis B: Environmental*, 2010. **99**(1-2): p. 329-335.
77. Pawar, R.C. and C.S. Lee, Single-step sensitization of reduced graphene oxide sheets and CdS nanoparticles on ZnO nanorods as visible-light photocatalysts. *Applied Catalysis B: Environmental*, 2014. **144**: p. 57-65.
78. Chong, M.N., et al., Recent developments in photocatalytic water treatment technology: A review. *Water Research*, 2010. **44**: p. 2997-3027.
79. Jin, Z., et al., Porous TiO₂ nanowires derived from nanotubes: Synthesis, characterization and their enhanced photocatalytic properties. *Microporous and Mesoporous Materials*, 2013. **181**: p. 146-153.
80. Xie, H., et al., Synthesis of TiO₂ nanoparticles by propane/air turbulent flame CVD process. *Particuology*, 2009. **7**(3): p. 204-210.

81. He, J., et al., A General, Efficient Method of Incorporation of Metal Ions into Ultrathin TiO₂ Films. *Chemistry of Materials*, 2002. **14**(8): p. 3493-3500.
82. Alexiadis, A. and I. Mazzarino, Design guidelines for fixed-bed photocatalytic reactors. *Chemical Engineering and Processing*, 2005. **44**(4): p. 453-459.
83. Boiarkina, I., S. Norris, and D.A. Patterson, The Case for the Photocatalytic Spinning Disc Reactor as a Process Intensification Technology: Comparison to an annular Reactor for the Degradation of Methylene Blue. *Chemical Engineering Journal*, 2013: p. Accepted Manuscript.
84. Nikazar, M., K. Gholivand, and K. Mahanpoor, Photocatalytic Degradation of Azo Dye Acid Red 114 in Water with TiO₂ Supported on Clinoptilolite as a Catalyst. *Desalination*, 2008. **219**(1-3): p. 293-300.
85. Dunnill, C.W., et al., White light induced photocatalytic activity of sulfur-doped TiO₂ thin films and their potential for antibacterial application. *Journal of Materials Chemistry*, 2009. **19**(46): p. 8747-8754.
86. Sa, J., et al., Photocatalytic Nitrate Reduction over Metal Modified TiO₂. *Applied Catalysis B*, 2009. **85**(3-4): p. 192-200.
87. Nezamzadeh-Ejhieh, A. and S. Hushmandrad, Solar photodecolorization of methylene blue by CuO/X zeolite as a heterogeneous catalyst. *Applied Catalysis A*, 2010. **388**(1-2): p. 149-159.
88. An, H., et al., Iron-coated TiO₂ nanotubes and their photocatalytic performance. *Journal of Materials Chemistry*, 2010. **20**(3): p. 603-610.
89. Quiñones, C., J. Ayala, and W. Vallejo, Methylene blue photoelectrodegradation under UV irradiation on Au/Pd-modified TiO₂ films. *Applied Surface Science*, 2010. **257**(2): p. 367-371.
90. Wang, C., et al., Preparation, characterization and photocatalytic activity of the neodymium-doped TiO₂ hollow spheres. *Applied Surface Science*, 2010. **257**(1): p. 227-231.

-
91. Chen, F., et al., Enhanced adsorption and photocatalytic degradation of high-concentration methylene blue on Ag₂O-modified TiO₂-based nanosheet. *Chemical Engineering Journal*, 2013. **221**: p. 283-291.
 92. Herrmann, J.-M., et al., TiO₂-Based Solar Photocatalytic Detoxification of Water Containing Organic Pollutants. Case Study of 2,4-Dichlorophenoxyacetic acid (2,4-D) and of Benzofuran. *Applied Catalysis B: Environmental*, 1998. **17**: p. 15-23.
 93. Sattler, C., et al., Solar Photocatalytic Water Detoxification of Paper Mill Effluents. *Energy*, 2004. **29**: p. 835-843.
 94. Blanco, J., et al., Review of feasible solar energy applications to water processes. *Renewable and Sustainable Energy Reviews*, 2009. **13**(6-7): p. 1437-1445.
 95. Cassano, A.E. and O.M. Alfano, Reaction engineering of suspended solid heterogeneous photocatalytic reactors. *Catalysis Today*, 2000. **58**(2-3): p. 167-197.
 96. Legrini, O., E. Oliveros, and A.M. Braun, Photochemical processes for water treatment. *Chemical Reviews*, 1993. **93**(2): p. 671-698.
 97. Ray, A.K., Design, Modelling and Experimentation of a New Large-Scale Photocatalytic Reactor for Water Treatment. *Chemical Engineering Science*, 1999. **54**(15-16): p. 3113-3125.
 98. Ray, A.K. and A.A.C.M. Beenackers, Development of a New Photocatalytic Reactor for Water Purification. *Catalysis Today*, 1998. **40**(1): p. 73-83.
 99. US-EPA, Wastewater Technology Fact Sheet Ultraviolet Disinfection. 1999.
 100. Taghipour, F., ed. Development of a CFD-Based Model for Photo-Reactor Simulation. *Parallel Computational Fluid Dynamics 2003: Advanced Numerical Methods, Software and Applications*, ed. A. Ecer, et al. 2004, Elsevier Science. 243-250.
 101. Han, Z., et al., A microfluidic device with integrated ZnO nanowires for photodegradation studies of methylene blue under different conditions. *Microelectronic Engineering*, 2013. **111**: p. 199-203.

102. Oelgemoller, M., Highlights of Photochemical Reactions in Microflow Reactors. *Chemical Engineering and Technology*, 2012. **35**(7): p. 1144-1152.
103. Mozia, S., Photocatalytic membrane reactors (PMRs) in water and wastewater treatment. A review. *Separation and Purification Methods*, 2010. **73**(2): p. 71-91.
104. Camera-Roda, G. and F. Santarelli, Design of a Pervaporation Photocatalytic Reactor for Process Intensification. *Chemical Engineering and Technology*, 2012. **35**(7): p. 1221-1228.
105. Lianos, P., Production of electricity and hydrogen by photocatalytic degradation of organic wastes in a photoelectrochemical cell The concept of the Photofuelcell: A review of a re-emerging research field. *Journal of Hazardous materials*, 2011. **185**(2-3): p. 575-590.
106. Kashyout, A.B., M. Soliman, and M. Fathy, Effect of preparation parameters on the properties of TiO₂ nanoparticles for dye sensitized solar cells. *Renewable Energy*, 2010. **35**(12): p. 2914-2920.
107. Vivar, M., et al., A concept for a hybrid solar water purification and photovoltaic system. *Solar Energy Materials and Solar Cells*, 2010. **94**(10): p. 1772-1782.
108. Sa, J., et al., Photocatalytic Nitrate Reduction over Metal Modified TiO₂. *Applied Catalysis B: Environmental*, 2009. **85**: p. 192-200.
109. Sun, D.D., H.T. Joo, and M.T. Koh, Photocatalytic Degradation of E.Coli form in Water. *Water Research*, 2003. **37**: p. 3452-3462.
110. Topalov, A., D. Molnar-Gabor, and J. Csanadi, Photocatalytic Oxidation of the Fungicide Metalaxyl Dissolved in Water over TiO₂. *Water Research*, 1999. **33**(6): p. 1371-1376.
111. Alexiadis, A. and I. Mazzarino, Design Guidelines for Fixed-Bed Photocatalytic Reactors. *Chemical Engineering and Processing*, 2005. **44**: p. 453-459.
112. Saien, J., et al., Photocatalytic Degradation of Direct Red 16 and Kinetic Analysis in a Conic Body Packed Bed Reactor with Nanostructure Titania Coated Raschig Rings. *Chemical Engineering Journal*, 2009. **151**: p. 295-301.

-
113. Nikazar, M., K. Gholivand, and K. Mahanpoor, Photocatalytic Degradation of Azo Dye Acid Red 114 in Water with TiO₂ Supported on Clinoptilolite as a Catalyst. *Desalination*, 2008. **219**: p. 293-300.
114. Ray, A.K., Design, Modelling and Experimentation of a New Large-Scale Photocatalytic Reactor for Water Treatment. *Chemical Engineering Science*, 1999. **54**: p. 3113-3125.
115. Peill, N.J. and M.R. Hoffmann, Development and Optimization of a TiO₂-Coated Fiber-Optic Cable Reactor: Photocatalytic Degradation of 4-Chlorophenol. *Environmental Science & Technology*, 1995. **29**: p. 2974-2981.
116. Ray, A.K. and A.A.C.M. Beenackers, Development of a New Photocatalytic Reactor for Water Purification. *Catalysis Today*, 1998. **40**: p. 73-83.
117. Ray, A.K. and A.A.C.M. Beenackers, Novel Photocatalytic Reactor for Water Purification. *AIChE Journal*, 1998. **44**(2): p. 477-483.
118. Ahmed, S., et al., Heterogeneous photocatalytic degradation of phenols in wastewater: A review on current status and developments. *Desalination*, 2010. **261**(1-2): p. 3-18.
119. Grabowska, E., J. Reszczyńska, and A. Zaleska, Mechanism of phenol photodegradation in the presence of pure and modified-TiO₂: A review. *Water Research*, 2012. **46**(17): p. 5453-5471.
120. Chakraborty, A.K., et al., Formation of highly crystallized TiO₂(B) and its photocatalytic behavior. *Applied catalysis B*, 2010. **93**(3-4): p. 368-375.
121. Saien, J., et al., Photocatalytic Degradation of Direct Red 16 and Kinetic Analysis in a Conic Body Packed Bed Reactor with Nanostructure Titania Coated Raschig Rings. *Chemical Engineering Journal*, 2009. **151**(1-3): p. 295-301.
122. Wang, J., et al., Investigation on photocatalytic degradation of ethyl violet dyestuff using visible light in the presence of ordinary rutile TiO₂ catalyst doped with upconversion luminescence agent. *Water Research*, 2006. **40**(11): p. 2143-2150.

123. Liu, Y., L. Hua, and S. Li, Photocatalytic degradation of Reactive Brilliant Blue KN-R by TiO₂/UV process. *Desalination*, 2010. **258**(1-3): p. 48-53.
124. Mathews, N.R., et al., TiO₂ thin films - influence of annealing temperature on structural, optical and photocatalytic properties. *Solar Energy*, 2009. **83**(9): p. 1499-1508.
125. Zhao, G., et al., Fabrication of electrospun Bi₂WO₆ microbelts with enhanced visible photocatalytic degradation activity. *Journal of Alloys and Compounds*, 2013. **578**: p. 12-16.
126. Zhao, W., et al., Photocatalytic degradation efficacy of Bi₄Ti₃O₁₂ micro-scale platelets over methylene blue under visible light. *Journal of Physics and Chemistry of Solids*, 2013. **74**(11): p. 1604-1607.
127. Le, H.A., et al., Photocatalytic degradation of methylene blue by a combination of TiO₂-anatase and coconut shell activated carbon. *Powder Technology*, 2012. **225**: p. 167-175.
128. Akpan, U.G. and B.H. Hameed, Parameters affecting the photocatalytic degradation of dyes using TiO₂-based photocatalysts: A review. *Journal of Hazardous Materials*, 2009. **170**(2-3): p. 520-529.
129. Khataee, A.R. and M.B. Kasiri, Photocatalytic degradation of organic dyes in the presence of nanostructured titanium dioxide: Influence of the chemical structure of dyes. *Journal of Molecular Catalysis A: Chemical*, 2010. **328**(1): p. 8-26.
130. Assadi, A.A., et al., Modeling of a continuous photocatalytic reactor for isovaleraldehyde oxidation: Effect of different operating parameters and chemical degradation pathway. *Chemical Engineering Research and Design*, 2013. **91**(7): p. 1307-1316.
131. Baranda, A.B., A. Barranco, and I.M.d. Maranon, Fast atrazine photodegradation in water by pulsed light technology. *Water Research*, 2012. **46**(3): p. 669-678.
132. Wols, B.A. and C.H.M. Hofman-Caris, Modelling micropollutant degradation in UV/H₂O₂ systems: Lagrangian versus Eulerian method. *Chemical Engineering Journal*, 2012. **210**: p. 289-297.
133. Calza, P., et al., Efficiency of TiO₂ photocatalytic degradation of HHCB (1,3,4,6,7,8-hexahydro-4,6,6,7,8,8-hexamethylcyclopenta[γ]-2-benzopyran) in natural aqueous solutions

by nested experimental design and mechanism of degradation. *Applied Catalysis B: Environmental*, 2010. **99**(1-2): p. 314-320.

134. Herrmann, J.-M., et al., TiO₂-based solar photocatalytic detoxification of water containing organic pollutants. Case studies of 2,4-dichlorophenoxyacetic acid (2,4-D) and of benzofuran. *Applied Catalysis B*, 1998. **17**(1): p. 15-23.

135. Lagunas-Allué, L., et al., Photocatalytic degradation of boscalid in aqueous titanium dioxide suspension: Identification of intermediates and degradation pathways. *Applied Catalysis B*, 2010. **98**(3-4): p. 122-131.

136. Khan, A., et al., Heterogeneous photocatalysed degradation of an insecticide derivative acetamiprid in aqueous suspensions of semiconductor. *Desalination*, 2010. **261**(1-2): p. 169-174.

137. Saien, J., H. Delavari, and A.R. Solymani, Sono-assisted photocatalytic degradation of styrene-acrylic acid copolymer in aqueous media with nano titania particles and kinetic studies. *Journal of Hazardous Materials*, 2010. **177**(1-3): p. 1031-1038.

138. McMurray, T.A., et al., Intrinsic Kinetics of Photocatalytic Oxidation of Formic and Oxalic Acid on Immobilized TiO₂ Films. *Applied Catalysis A*, 2004. **262**(1): p. 105-110.

139. Fernandez, C., M.S. Larrechi, and M.P. Callao, Modelling of the simultaneous photodegradation of Acid Red 97, Acid Orange 61 and Acid Brown 425 using factor screening and response surface strategies. *Journal of Hazardous Materials*, 2010. **180**(1-3): p. 474-480.

140. Juang, R.-S., S.-H. Lin, and P.-Y. Hsueh, Removal of binary azo dyes from water by UV-irradiated degradation in TiO₂ suspensions. *Journal of Hazardous Materials*, 2010. **182**(1-3): p. 820-826.

141. Khataee, A.R., et al., Optimization of photocatalytic treatment of dye solution on supported TiO₂ nanoparticles by central composite design: Intermediates identification. *Journal of Hazardous Materials*, 2010. **181**(1-3): p. 886-897.

142. Sakkas, V.A., et al., Photocatalytic degradation using design of experiments: A review and example of the Congo red degradation. *Journal of Hazardous Materials*, 2010. **175**(1-3): p. 33-44.
143. Vargas, R. and O. Nunez, Photocatalytic degradation of oil industry hydrocarbons models at laboratory and at pilot-plant scale. *Solar Energy*, 2010. **84**(2): p. 345-351.
144. Zhong, L., et al., Modeling and physical interpretation of photocatalytic oxidation efficiency in indoor air applications. *Building and Environment*, 2010. **45**(12): p. 2689-2697.
145. Zhong, L. and F. Haghghat, Modeling and validation of a photocatalytic oxidation reactor for indoor environment applications. *Chemical Engineering Science*, 2011. **66**(23): p. 5945-5954.
146. Zekri, M.e.M. and C. Colbeau-Justin, A mathematical model to describe the photocatalytic reality: what is the probability that a photon does its job? *Chemical Engineering Journal*, 2013: p. Accepted manuscript.
147. Queffeuou, A., L. Geron, and E. Schaer, Prediction of photocatalytic air purifier apparatus performances with a CFD approach using experimentally determined kinetic parameters. *Desalination*, 2010. **259**(1-3): p. 147-155.
148. Qi, N., et al., CFD modelling of hydrodynamics and degradation kinetics in an annular slurry photocatalytic reactor for wastewater treatment. *Chemical Engineering Journal*, 2011. **172**: p. 84-95.
149. Motegh, M., et al., Photocatalytic-reactor efficiencies and simplified expressions to assess their relevance in kinetic experiments. *Chemical Engineering Journal*, 2012. **207-208**(22nd International Symposium on Chemical Reaction Engineering): p. 607-615.
150. Misstear, D.B. and L.W. Gill, The inactivation of phages MS2, Φ X174 and PR772 using UV and solar photocatalysis. *Journal of photochemistry and Photobiology B: Biology*, 2012. **107**: p. 1-8.
151. Lee, J.E. and G. Ko, Norovirus and MS2 inactivation kinetics of UV-A and UV-B with and without TiO₂. *Water Research*, 2013. **47**: p. 5607-5613.

-
152. Xu, C., X.S. Zhao, and G.P. Rangaiah, Performance analysis of ultraviolet water disinfection reactors using computational fluid dynamics simulation. *Chemical Engineering Journal*, 2013. **221**: p. 398-406.
153. Lin, S. NGPM -- A NSGA-II Program in Matlab v1.4. <http://www.mathworks.com/matlabcentral/fileexchange/31166> 2011 [cited 2013 April]; Available from: <http://www.mathworks.com/matlabcentral/fileexchange/31166>.

List of Publications

Chen Xu, G.P. Rangaiah and X.S. Zhao, *A Computational Study of the Effect of Lamp Arrangements on the Performance of Ultraviolet Water Disinfection Reactors*, Revised manuscript submitted to Chemical Engineering Science, 2014

Chen Xu, G.P. Rangaiah and X.S. Zhao, *Application of Artificial Neural Network and Genetic Programming in Modeling and Optimization of Ultra-Violet Water Disinfection Reactors*, Chemical Engineering Communications, Accepted, 2014

Chen Xu, G.P. Rangaiah and X.S. Zhao, *Photocatalytic Degradation of Methylene Blue by Titanium Dioxide: Experimental and Modeling Study*, Industrial & Engineering Chemistry Research, Accepted, 2014

Chen Xu, X.S. Zhao, G.P. Rangaiah (2013), *Performance analysis of ultraviolet water disinfection reactors using computational fluid dynamics simulation*, Chemical Engineering Journal **221**: p. 398 – 406

Jia Hong Pan, Haiqing Dou, Zhigang Xiong, **Chen Xu**, Jizhen Ma and X. S. Zhao (2010), *Porous photocatalysts for advanced water purifications*, Journal of Materials Chemistry **20**: p. 4512 – 4528

Zhigang Xiong, Haiqing Dou, Jiahong Pan, Jizhen Ma, **Chen Xu** and X. S. Zhao (2010), *Synthesis of mesoporous anatase TiO₂ with a combined template method and photocatalysis*, Crystal Engineering Communications **12**: p. 3455 – 3457

Conference Presentation

Chen Xu, G.P. Rangaiah and X.S. Zhao (2013), *Application of Artificial Neural Network in Modelling Ultraviolet Water Disinfection Reactor*, Presentation at 2nd International Conference on Water Research, January 2013, Singapore